FEDERAL UNIVERSITY OF SÃO CARLOS
CENTER OF EXACT SCIENCES AND TECHNOLOGY
DEPARTMENT OF CHEMISTRY
POSTGRADUATE PROGRAM IN CHEMISTRY

DEVELOPMENT AND CHARACTERIZATION OF KEFIRAN/CARBOXYMETHYL CELLULOSE/ZNO NPS NANOCOMPOSITES FOR FOOD PACKAGING APPLICATIONS

Gleison Neres Marques*

Thesis presented as part of the requirements for obtaining the title of DOCTOR OF SCIENCE, concentration area: PHYSICAL-CHEMISTRY

Advisor: Dr. Lucia H. Mascaro

***São Paulo Research Foundation (FAPESP): grants Nº 2021/06128-5 and 2023/04376-7 (BEPE)**

Programa Estratégico Emergencial de Prevenção e Combate a Surtos, Endemias, Epidemias e Pandemias (CAPES No. 9/2020)

São Carlos – SP

2025

UNIVERSIDADE FEDERAL DE SÃO CARLOS

Centro de Ciências Exatas e de Tecnologia
Programa de Pós-Graduação em Química

Folha de Aprovação

Defesa de Tese de Doutorado do candidato Gleison Neres Marques, realizada em 04/07/2025.

Comissão Julgadora:

Profa. Dra. Lucia Helena Mascaro Sales (UFSCar)

Profa. Dra. Farayde Matta Fakhouri (UFGD)

Profa. Dra. Isabela Rosier Olimpio Pereira (Mackenzie)

Profa. Dra. Sandra Andrea Cruz (UFSCar)

Profa. Dra. Maria Inês Basso Bernardi (USP)

O Relatório de Defesa assinado pelos membros da Comissão Julgadora encontra-se arquivado junto ao Programa de Pós-Graduação em Química.

ACKNOWLEDGEMENT

This doctoral Thesis was carried out at the Chemistry Department of the Federal University of São Carlos between September 2020 and September 2024. Some stages of the study were conducted in the laboratories of the Institute of Physics at the University of São Paulo (USP - IFSC) and the Materials Engineering Laboratory of the Universitat Politècnica de Catalunya (UPC Barcelona Tech). This study is part of the *Programa Estratégico Emergencial de Prevenção e Combate a Surtos, Endemias, Epidemias e Pandemias – Edital CAPES n° 9/2020*. I want to thank the following individuals for their assistance, support, and guidance throughout this study.

To Jehovah God, who has always given me the strength to carry on and do my best.

My parents, Claudio Roberto Lopes Marques and Antônia Neres Marques have always encouraged and supported me. I also want to thank my siblings, Jéssica Neres and Jefferson Neres, for their constant encouragement.

I would like to extend a huge thank you to Sergio Montilla, my partner in battles in Spain and Paris, and life.

I want to thank Prof. Dr. Lucia H. Mascaro for the opportunity she provided when I joined her research group, for her teachings, guidance, discussions, and the freedom to grow as a professional by exploring various topics.

Prof. Maria Inês Basso Bernardi has helped me with my studies since I earned my master's degree. I thank her immensely for always showing great concern, even when I was away. I would also like to thank all the technicians and friends of the Nanomaterials and Advanced Ceramics Group (NaCA) at IFSC USP campus 2.

To Prof. Dr. Jose Ignacio Velasco, thank you for accepting me at the Polytechnic University of Catalonia—UPC and for giving me all the support I

needed. I also thank Prof. Dr. Farayde Matta Fakhouri for helping me get into the UPC and for assisting with my studies.

Thank you to Regiane Cristina de Oliveira for always supporting me. I also thank her for teaching me a great deal about studying.

To Roberta Yonara, who was a partner in study and courses and was a shoulder to lean on so many times during these four years. I also thank Davi Souza and Fernando Vasconcelos for their friendship and help with their study.

I would also like to thank Dr. Ailton Moreira for the rich discussions on science and the opportunity to collaborate in an area that fascinates me: photodegradation.

To Professor Isabella Rosier Pereira, thank you for helping me understand the process of extracting and purifying kefiran.

To all my friends from São Luís and even Piauí who shared the apartment in Alameda das Azaleias, our eternal BBB. To Fiama Martins and Moisés Rocha for helping me from the moment I arrived in São Carlos.

To the CDMF and my LIEC's friends who always supported me and were partners. To the technicians Rorivaldo Camargo, Ricardo Tranquilin, Anna Esther Carrillo, Priscila Cervini, and Manoel Ricardo Roncon for the electron microscopy images.

To FAPESP for the PhD scholarship (2021/06128-5) and the internship abroad (2023/04376-7). To CAPES for the scholarship (001).

To Luciana, a technician at the "Sérgio Mascarenhas" Biophysics and Structural Biology Group (BBE), for providing the equipment needed to synthesize the polymer

Andei.
Por caminhos difíceis, eu sei.
Mas olhando o chão sob meus pés,
vejo a vida correr.
E, assim, cada passo que der,
tentarei fazer o melhor que puder.
Aprendi.
Não tanto quanto quis, mas vi que, conhecendo
O universo ao meu redor, aprendo a me conhecer melhor,
E assim escutarei o tempo, que ensinará
A tomar a decisão certa em cada momento.
E partirei, em busca de muitos ideais.
Mas sei que hoje
Se encontram meu passado, futuro e presente.
Hoje sinto em mim a emoção da despedida.
Hoje é um ponto de chegada e, ao mesmo tempo, ponto de partida.
Se em horas de encontros pode haver tantos desencontros, que a hora da separação seja, tão-somente, a hora de um verdadeiro, profundo e coletivo encontro.
De tudo ficarão três coisas:
a certeza de estar sempre começando,
a certeza de que é preciso continuar
e a certeza de ser interrompido antes de terminar.
Fazer da queda um passo de dança,
do medo uma escada, do sonho uma ponte,
da procura um encontro."

Fernando Sabino

Encontro Marcado

Nada a temer senão o correr da luta
Nada a fazer senão esquecer o medo
Abrir o peito a força, numa procura
Fugir às armadilhas da mata escura

Milton Nascimento

Caçador De Mim

LIST OF ABBREVIATIONS

ANOVA, Analysis Of Variance

ATCC, American Type Culture Collection

ATR-FTIR, Attenuated Total Reflectance Fourier-Transform Infrared

BC, Bacterial Cellulose

BHI, Brain Heart Infusion Agar

COVID-19, Coronavirus Disease

SARS-Cov-2, Severe Acute Respiratory Syndrome Coronavirus 2

EPS, Exopolysaccharide

CFU, Colony Forming Unit

CMC, Carboxymethyl Cellulose

CMS, Carboxymethyl Starch Sodium

DRS, Diffuse Reflectance Spectroscopy

DS, Degree Swelling

EB, Elongation at Break

EC, Edible Coating

EM, Elastic Modulus

EPS, Exopolysaccharides

ESKAPE (*Enterococcus faecium, Staphylococcus aureus, Klebsiella pneumoniae, Acinetobacter baumannii, Pseudomonas aeruginosa*, and *Enterobacter* spp.)

FAAS, Flame Atomic Absorption Spectroscopy

FDA, Food And Drug Administration

FTIR, Fourier Transform Infrared Spectroscopy

Ham, Microwave-Assisted Hydrothermal Method

HPMC, Hydroxypropyl Methylcellulose

ICSD, Inorganic Crystal Structure Database

MC, Moisture Content

MEP, Molecular Electrostatic Potential

MHCA, Mueller Hinton Cation Adjusted Broth

MIC, Minimum Inhibitory Concentration

NMR, Nuclear Magnetic Resonance

Nps, Nanoparticles

PBS, Phosphate-Buffered Saline

PCA, Principal Component Analysis

PDA, Potato Dextrose Agar

Ph, Potential Of Hydrogen

ROS, Reactive Oxygen Species

SEM, Scanning Electron Microscopy

SS, Soluble Solids

TA, Titratable Acidity

TS, Tensile Strength

TSS, Total Soluble Solids

WCA, Water Contact Angle

WPU, Water-Based Polyurethane

WVP, Water Vapour Permeability

XPS, X-Ray Photoelectron Spectroscopy

XRD, X-Ray Diffraction

LIST OF TABLES

LIST OF FIGURES

ABSTRACT

DEVELOPMENT AND CHARACTERIZATION OF KEFIRAN, CARBOXYMETHYL CELLULOSE, ZNO NPS NANOCOMPOSITES FOR FOOD PACKING APPLICATIONS. Polysaccharides are polymers derived from natural and renewable sources, which can be utilized in various applications, including the packaging industry. Kefiran is one of these polymers that has gained prominence recently due to its antimicrobial properties. Several studies have sought to combine the intrinsic properties of kefiran with other biopolymers and oxide nanoparticles as an effective alternative for producing active food packaging. In this context, the present study investigates, in detail, the development of films and edible coatings based on kefiran, carboxymethyl cellulose (CMC), and zinc oxide nanoparticles (ZnO NPs) for food packaging applications. Kefiran was extracted and purified from kefir grains, and its purity and structural features were confirmed by proton and carbon nuclear magnetic resonance (^{1}H and ^{13}C NMR), Fourier-transform infrared spectroscopy (FT-IR), and gel permeation chromatography (GPC). For the first time, kefiran exhibited significant antibiofilm activity against *Staphylococcus epidermidis* ATCC 35984, achieving eradication at 512 mg/L ($p < 0.001$). At the same time, ZnO NPs were synthesized via a microwave-assisted hydrothermal method and showed high crystallinity and distinct morphologies. These nanoparticles exhibited selective bactericidal activity against Gram-positive multidrug-resistant bacteria, primarily due to the generation of reactive oxygen species (ROS), especially hydroxyl radicals. Statistical analyses demonstrated that minimum inhibitory concentrations (MICs) of 256 and 512 mg/mL were effective in bacterial inhibition, highlighting the potential of ZnO NPs for functionalization in bio-based packaging systems. Subsequently, nanocomposite films were prepared by incorporating ZnO NPs into the kefiran/CMC matrix at different concentrations (5, 10, and 25% w/w), and their physicochemical, mechanical, structural, and

functional properties were thoroughly evaluated. Characterization techniques, including Scanning Electron Microscopy (SEM), Atomic Force Microscopy (AFM), X-ray Diffraction (XRD), X-ray Photoelectron Spectroscopy (XPS), Raman spectroscopy, Fourier-Transform Infrared Spectroscopy (FT-IR), and Ultraviolet–Visible (UV-Vis) spectroscopy, revealed significant morphological, structural, and optical changes resulting from the incorporation of ZnO NPs. The nanocomposites exhibited improved mechanical strength, UV-blocking capacity, and water vapor barrier properties. Additionally, the films demonstrated enhanced antimicrobial activity, particularly against *Staphylococcus aureus*, indicating their suitability for active food packaging applications.
Keywords: Kefiran, active films, antimicrobial, antibiofilm, food packaging

RESUMO

DESENVOLVIMENTO E CARACTERIZAÇÃO DE NANOCOMPÓSITOS À BASE DE KEFIRAN, CARBOXIMETILCELULOSE E ZNO NPS PARA APLICAÇÕES EM EMBALAGENS DE ALIMENTOS. Os polissacarídeos são polímeros derivados de fontes naturais e renováveis, que podem ser utilizados em várias aplicações, inclusive no setor de embalagens. O kefiran é um desses polímeros que ganhou destaque recentemente devido às suas propriedades antimicrobianas. Vários estudos buscaram combinar as propriedades intrínsecas do kefiran com outros biopolímeros e nanopartículas de óxido como uma alternativa eficaz para a produção de embalagens ativas para alimentos. Nesse contexto, o presente estudo investiga, em detalhes, o desenvolvimento de filmes e revestimentos comestíveis à base de kefiran, carboximetilcelulose (CMC) e nanopartículas de óxido de zinco (NPs de ZnO) para aplicações em embalagens de alimentos. O kefiran foi extraído e purificado dos grãos de kefir, e sua pureza e características estruturais foram confirmadas por ressonância magnética nuclear de prótons e carbono (^{1}H e ^{13}C NMR), espectroscopia de infravermelho com transformada de Fourier (FT-IR) e cromatografia de permeação em gel (GPC). Pela primeira vez, o kefiran apresentou atividade antibiofilme significativa contra *Staphylococcus epidermidis* ATCC 35984, alcançando erradicação a 512 mg/L ($p < 0,001$). Ao mesmo tempo, as NPs de ZnO foram sintetizadas por meio de um método hidrotérmico assistido por micro-ondas e apresentaram alta cristalinidade e morfologias distintas. Essas NPs apresentaram atividade bactericida seletiva contra bactérias Gram-positivas resistentes a múltiplos medicamentos, principalmente devido à geração de espécies reativas de oxigênio (ROS), especialmente radicais hidroxila. As análises estatísticas demonstraram que as concentrações inibitórias mínimas (MICs) de 256 e 512 mg/mL foram eficazes na inibição bacteriana, destacando o potencial das NPs de ZnO para a

funcionalização em sistemas de embalagem. Em seguida, os filmes nanocompósitos foram preparados com a incorporação de NPs de ZnO na matriz de kefiran/CMC em diferentes concentrações (5, 10 e 25% m/m), e suas propriedades físico-químicas, mecânicas, estruturais e funcionais foram avaliadas. As técnicas de caracterização, incluindo microscopia eletrônica de varredura (SEM), microscopia de força atômica (AFM), difração de raios X (XRD), espectroscopia de fotoelétrons de raios X (XPS), espectroscopia Raman, espectroscopia de infravermelho com transformada de Fourier (FT-IR) e espectroscopia ultravioleta-visível (UV-Vis), revelaram mudanças morfológicas, estruturais e ópticas significativas resultantes da incorporação de NPs de ZnO. Os nanocompósitos apresentaram maior resistência mecânica, capacidade de bloqueio de UV e propriedades de barreira ao vapor de água. Além disso, os filmes demonstraram uma atividade antimicrobiana aprimorada, especialmente contra *Staphylococcus aureus*, indicando sua adequação para aplicações em embalagens ativas de alimentos.

Palavras-chave: Kefiran, filmes ativos, antimicrobiano, antibiofilme, embalagens de alimentos

TABLE OF CONTENTS

PREFACE

Among the alternatives that address these environmental concerns, bio-based plastic derived from renewable sources has emerged as an effective strategy to mitigate sustainability issues and pollution problems. In this context, the development of active packaging, capable of controlling or preventing the growth of bacteria, fungi, and viruses, has gained attention as a practical approach for enhancing food safety and, in some cases, extending shelf life. One such biopolymer is kefiran, a high-molar-mass, branched glucogalactan that has garnered significant interest due to its antibacterial, antitumor, and immunomodulatory properties, making it a promising candidate for various applications. However, certain limitations, such as the insufficient mechanical strength and barrier properties of kefiran-based films, must be addressed to make them viable alternatives to conventional polymers in terms of performance and cost-effectiveness. Therefore, the central motivation of this study is to develop kefiran-based nanocomposite films incorporating carboxymethyl cellulose (CMC) and zinc oxide nanoparticles (ZnO NPs) to enhance their barrier, mechanical, and antimicrobial properties, thus enabling their potential application in food packaging systems.

To provide a clear understanding of this thesis, the work has been organized into six chapters. Chapter 1 presents the state of the art, covering the central topics addressed in this research, including the use of polysaccharides in film production and the development of active packaging systems incorporating antimicrobial agents. Chapter 2 outlines the general and specific objectives that guide the research scope, as well as the underlying motivation for addressing the identified problem. Chapter 3 describes the experimental procedures, beginning with the extraction and characterization of kefiran, followed by the synthesis of ZnO NPs. The optimization of CMC- and kefiran-based films is then detailed,

along with the methods employed for the preparation and characterization of nanocomposite films containing different concentrations of ZnO NPs. Chapter 4 presents the results obtained throughout the research, along with a detailed discussion of their significance and implications. Chapter 5 presents the final remarks and general conclusions drawn from the study, followed by a comprehensive list of references that support the development of this thesis, Chapter six.

The appendix provides additional material that complements the main text, including supporting data and scientific articles that have been submitted or accepted for publication as a result of this research.

Chapter 1 GENERAL INTRODUCTION

1.1 Potential use of biodegradable polymeric materials based on polysaccharides in the food packaging industry

In recent years, environmental pollution caused by the accumulation of non-biodegradable plastics has increased significantly, becoming a global concern [1–3]. The slow degradation of these materials, combined with the release of chemical additives used in their manufacture, contributes to their persistent accumulation across diverse environments and ecosystems. This accumulation can lead to irreversible imbalances, affecting various species, including plants, aquatic organisms, and even humans [4–6]. Given the growing environmental impacts related to greenhouse gas emissions and marine contamination, various strategies have been discussed to mitigate the issues associated with conventional plastics. Among these, recycling, energy recovery, and the development of alternative materials, such as biodegradable biopolymers, stand out. In addition to environmental concerns, there is also increasing pressure from policies and regulations aimed at promoting a circular economy for plastics, which emphasizes the importance of integrated and sustainable solutions [4,5].

In this context, several biopolymers have attracted attention not only for their renewable origin but also for their potential in applications such as controlled drug release and the development of antimicrobial food packaging. This is mainly due to their favorable properties, including excellent biocompatibility and water solubility [3,7–10]. In particular, growing concern over the environmental impact of petroleum-based, non-biodegradable plastics, along with issues related to micro- and nanoplastic contamination and the increasing demand for renewable alternatives, has intensified research into polysaccharide (PS)-based materials [11,12]. PSs are complex carbohydrates made of monosaccharides linked by glycosidic bonds, regardless of their origin [12]. These

units range from D-glucose and D-fructose to D-galactose and D-galactosamine[13]. Naturally abundant and nontoxic, PSs are attractive for biomedical applications, such as drug delivery and wound healing, as well as food packaging[13] (Figure 1.1).

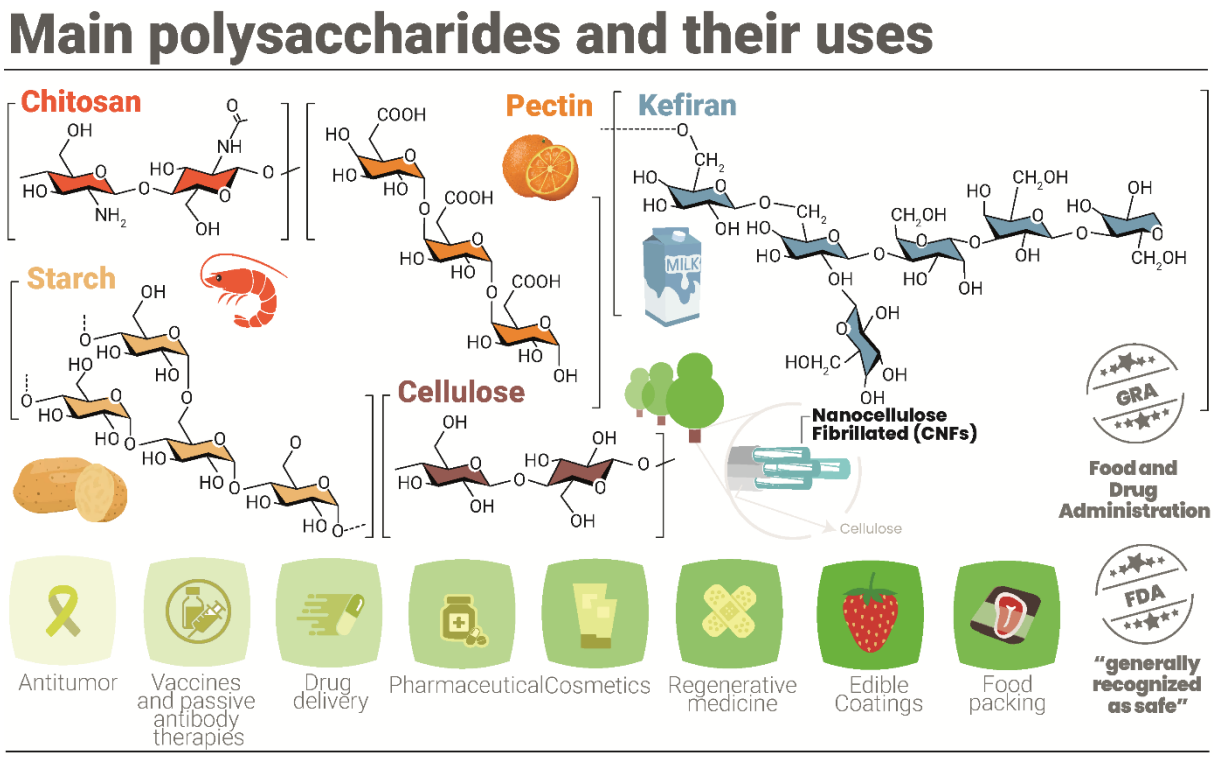

FIGURE 1.1- Chemical structures of the main polysaccharides used to produce biodegradable packaging.

PS-based materials offer desirable properties, including gas barrier capacity, low water vapor permeability, good tensile strength, and the potential to extend shelf life due to the antioxidant properties of specific matrices[10]. Their versatility stems mainly from their recognized safety, endorsed by regulatory agencies such as the U.S. Food and Drug Administration (FDA). Chitosan, for instance, is a non-toxic, biocompatible, and biodegradable biopolymer widely commercialized due to the abundance of its precursor, chitin [10,14] (Figure 1.1). This linear polysaccharide stands out for its antimicrobial activity against fungi and bacteria, offering an advantage over other biopolymers and enabling its use

in drug delivery, tissue engineering, and other biomedical applications [14]. Several studies report the antimicrobial efficacy of this polymer in biodegradable plastics, attributing it to electrostatic interactions between the polymer and microorganisms [14–16].

Subramani et al. (2024) [15] developed a chitosan film incorporating bio-vanillin and kaolin clay, exhibiting antimicrobial, antioxidant, and antifungal properties. Additionally, weight loss and color change tests revealed its high preservation capacity for freshly cut apples. Hu et al. (2018)[17] developed multilayer films combining acrylamide-modified chitosan and alginate for strawberry packaging. The synergy between the polysaccharides endowed the films with self-healing properties, restoring surface integrity after minor cuts, and anti-fogging capacity. A key drawback of chitosan is its insolubility in water without acidification (pH < 6.3) [14]. In contrast, starch, another widely used, non-toxic polysaccharide, readily dissolves in water and is commonly applied as a fruit coating to extend shelf life [8,18].

Similarly, cellulose is a renewable and abundant biopolymer naturally produced by plants and microorganisms, further expanding the range of viable PSs for sustainable material development [11,19,20]. It consists of linear chains of repeating D-glucose units ($C_6H_{10}O_5$) linked by β-1,4-glycosidic bonds (Figure 1.1), which confer structural strength and stability. These characteristics make cellulose a promising material for sustainable applications. Due to extensive hydrogen bonding and high crystallinity, cellulose is insoluble in water and most common organic solvents [20,21]. However, this limitation can be overcome by using cellulose derivatives, such as methylcellulose, hydroxypropyl methylcellulose (HPMC), and carboxymethyl cellulose (CMC), which have modified chemical groups that enhance their solubility and expand their usability in various industries [10]. Furthermore, processing cellulose's structure can yield nanometer-scale

particles, such as cellulose nanofibrils (CNF) and cellulose nanocrystals (CNC), which exhibit enhanced properties ideal for food packaging applications [22].

Additionally, cellulose can be produced by microorganisms like *Gluconacetobacter*, forming a nanofiber network with a three-dimensional structure[23]. Microbially derived polysaccharides, such as kefiran, an important exopolysaccharide (EPS) produced by bacterial biofilms in milk, have gained increasing prominence due to their unique properties [24].

1.2. Kefiran – An important exopolysaccharide

These microbial polysaccharides not only expand the range of natural biopolymers available but also offer distinct functional properties that are increasingly explored for applications in food preservation, biomedicine, and packaging. Among them, kefiran, a high-molar-mass branched glucogalactan, has attracted significant interest due to its antibacterial, antitumor, and immunomodulatory effects [25–27]. The antitumor activity of kefiran was demonstrated in vivo through oral administration in mice with Ehrlich carcinoma and sarcoma 180 tumors [28]. Its ability to enhance antibody production and activate macrophages led to significant reductions in tumor size and weight. Structurally, kefiran consists of nearly equal amounts of D-glucose and D-galactose arranged in chains [24,27].

The promising bioactive properties of kefiran have stimulated extensive research into its production and application; however, its potential as an edible coating for fruits remains an unexplored area [29,30]. Despite its promising functionality, the large-scale application of kefiran films faces challenges primarily related to production scalability. Factors such as the choice of carbon source and the time required for biofilm development significantly influence yield [31]. The microbial community responsible for kefiran synthesis varies depending on the culture [25,32,33]; however, it typically includes bacteria such as *Lactobacillus*

kefiranofaciens, *Lactococcus*, *Streptococcus*, and yeasts from the *Saccharomycetaceae* family [24,27,34,35]. Research on kefiran extends beyond biofilm composition to optimizing fermentation parameters, including pH, temperature, and culture medium composition, to enhance EPS production and maximize kefiran yield [33,36,37]. Such optimization is crucial for improving scalability and consistency in kefiran-based applications [38,39]. However, depending on the microbial strains used during grain cultivation, variations in growth kinetics and EPS properties may occur[31].

Moreover, scaling up production while maintaining consistency is essential to meet industrial demands and ensure product efficacy. In this context, the extraction and purification processes are equally important. Typically, kefiran is extracted by dissolving the grains in distilled water at 100 °C, followed by centrifugation at 20 °C to remove residues. The supernatant is treated with 98% ethanol and refrigerated at –20 °C for 24 hours. This cycle is repeated three times before the polymer is lyophilized. Recent efforts to optimize these steps have explored variations in dissolution and precipitation temperatures to enhance yield and purity [40]. To address these limitations, studies have focused not only on optimizing fermentation conditions and incorporating industrial by-products as alternative carbon sources, but also on enhancing kefiran's functional performance through its combination with other polysaccharides [39]. This strategy is particularly relevant given the common drawbacks of some PS-based films, including high moisture sensitivity and poor mechanical strength [3].

Blending kefiran with other polysaccharides has emerged as a promising strategy to address its limitations, particularly its sensitivity to moisture and limited mechanical strength (Figure 1.2) [24,27,41]. For instance, Rad et al. (2017)[42] investigated the incorporation of water-based polyurethane (WPU) into kefiran films and evaluated its impact on film properties. Through morphological analysis, thermal behavior, and FTIR spectroscopy, the study demonstrated that

formulations containing up to 30% WPU by weight exhibited improved miscibility and compatibility. These interactions led to enhanced mechanical performance and optical clarity, indicating the potential of such blends for advanced packaging applications [42].

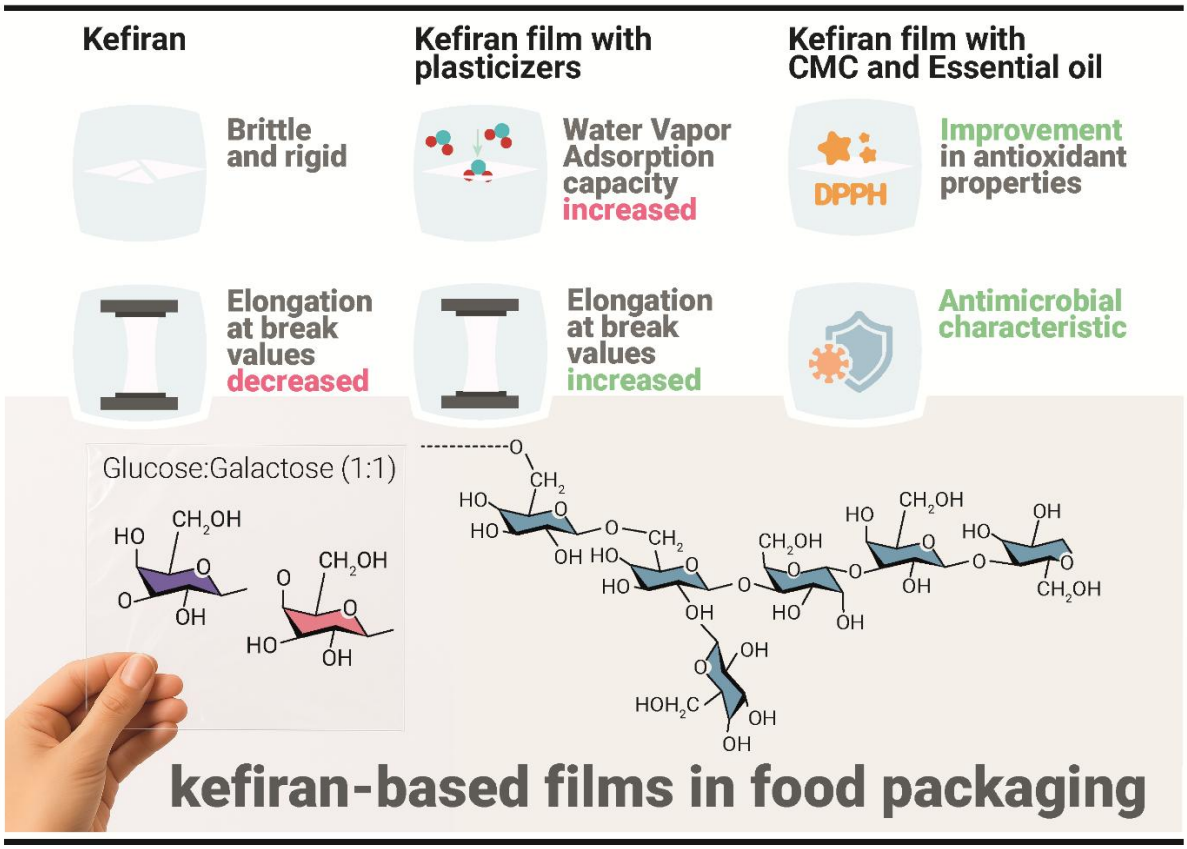

FIGURE 1.2- Main characteristics of films produced with pure Kefiran [43], with the addition of different plasticizers [44], and as a blend with Carboxymethyl cellulose (CMC) and *Satureja Khuzestanica* essential oil [45].

In another study, Motedayen et al. (2013)[46] reported that although kefiran and starch are compatible, increasing starch concentration negatively affected the films' mechanical properties and surface wettability, limiting their incorporation to a maximum of 50%. This finding highlights the importance of optimizing polymer ratios, as they directly influence film thickness and, consequently, key characteristics such as mechanical strength, transparency, and water vapor permeability (WVP) [47]. In some cases, physical crosslinking has been

employed to enhance the mechanical performance of carboxymethyl starch sodium (CMS) films [48], while other approaches have focused on incorporating plasticizers to improve the tensile strength of biopolymer-based films. In addition to structural modifications, several studies have explored the incorporation of additives, such as plasticizers, to enhance the tensile strength of biopolymer-based films [45]. The strategy of blending two or more biopolymers to improve film properties is well-established. However, selecting the ideal polysaccharide requires careful evaluation of multiple factors, including cost, availability, intrinsic properties, compatibility, and processability [49].

1.3 Carboxymethylcellulose to improve kefiran properties

Carboxymethylcellulose (CMC) is a cellulose derivative obtained through etherification, in which hydroxyl groups (–OH) are partially substituted by carboxymethyl groups (–CH_2COONa). This structural modification improves its solubility in water, enabling its application in various fields, including the development of biodegradable food packaging [50,51]. Among the methods reported for producing CMC-based plastic films are electrospinning, extrusion, and casting (Figure 1.3) [52,53]. The casting method is the most commonly used on a laboratory scale due to its low cost, the high solubility of CMC, and the simplicity of the technique. Additionally, CMC has a limited electrospinning capacity and cannot be extruded on its own [54]. In the casting method, CMC is first dissolved in water or another suitable solvent under constant stirring and controlled temperature (Figure 1.3). In some cases, particularly when temperatures exceed 50 °C, this process can lead to the formation of unwanted air bubbles in the solution [54]. The resulting solution is then poured onto plates to allow the solvent to evaporate, a process that can occur at room temperature or in an oven with air circulation. The resulting films are generally transparent, although the incorporation of additional materials may alter their optical properties (Figure 1.3). The incorporation of additional materials into the CMC matrix can significantly influence the

properties of the films, particularly water vapor permeability (WVP), surface wettability, and mechanical performance.

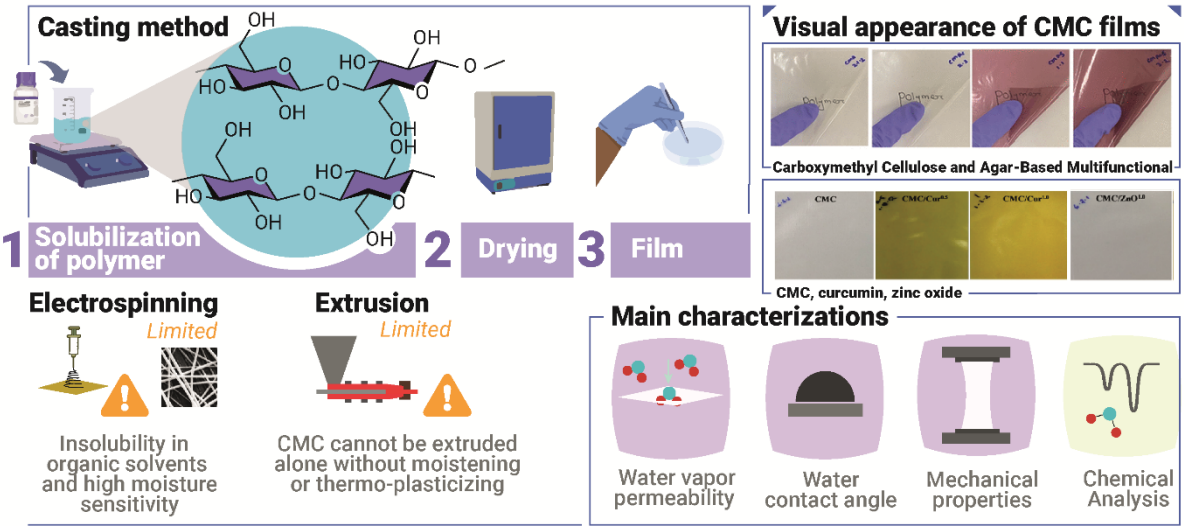

FIGURE 1.3– Main methods used to produce CMC-based films (casting, electrospinning[52], and extrusion). Visual appearance of CMC films produced by adding different materials (CMC and agar [55] and CMC-curcumin-zinc oxide [53]). Primary characterization methods used in the study of polysaccharide films.

All these processing parameters significantly influence the properties of the resulting films, especially since several studies have reported the use of CMC concentrations above 7% (w/v) in solution [56]. For example, increasing the film thickness improves its mechanical response but reduces its transparency [57]. Conversely, increasing thickness can decrease water vapor permeability while increasing its moisture content [58,59]. Increasing the concentration of the polymer matrix can even affect the surface's wettability, as in the case of starch films, for example. Optimizing processing parameters is a crucial step in film production, from selecting the appropriate blend to achieving optimal film performance [60,61]

However, despite its advantages, CMC presents certain limitations that must be addressed. Its hydrophilic nature leads to moisture absorption from the environment, compromising both mechanical strength and gas vapor barrier properties. Additionally, CMC lacks inherent antimicrobial activity, making it

necessary to functionalize the polymer with antimicrobial agents [62]. Valizadeh et al. (2019) [63], for instance, developed films based on CMC and chitosan, and found that the addition of glutaraldehyde as a cross-linking agent enhanced both mechanical properties and antioxidant capacity.

A review by Filho et al. (2025)[31], highlighted kefiran's strong antimicrobial activity against bacteria such as *Streptococcus pyogenes*, *Staphylococcus aureus*, *Streptococcus salivarius*, *Salmonella typhimurium*, *Listeria monocytogenes*, *Pseudomonas aeruginosa*, and *Escherichia coli*, as a key factor driving its use in bioplastic film development. The strong synergistic interaction between CMC and other biopolymers makes it a promising strategy for enhancing the functional properties of kefiran-based films. This approach has been further explored by Hasheminya et al. (2019)[45], who developed bionanocomposite films combining kefiran and CMC with *Satureja Khuzestanica* essential oil. The incorporation of the essential oil significantly improved the tensile strength (TS) of the films, while reducing their elongation at break (EB). Additionally, it notably modified the films' color parameters and transparency. Regarding antimicrobial activity, the resulting films exhibited inhibitory effects against both Gram-positive and Gram-negative bacteria. Motedayen et al. (2019)[64] developed kefiran-CMC biocomposite films with varying proportions of the biopolymers, utilizing glycerol as a plasticizer. The authors observed that increasing the CMC content up to 50% (v/v) improved the tensile strength and extensibility of the films, but higher concentrations reduced these properties. The WVP initially decreased and then increased with the addition of CMC. Morphological characterization revealed rougher surfaces with higher CMC content, and thermal analysis indicated good compatibility between the polymers.

Although kefiran exhibits inherent antimicrobial activity, the incorporation of nanoparticles has been investigated as a strategy to enhance this property further [45,65,66]. These agents, when combined with kefiran, can act

synergistically, enhancing the film's antimicrobial effectiveness against a broader spectrum of microorganisms and potentially improving other functional properties, such as barrier capacity and mechanical strength.

1.4 Metal oxide nanoparticles

The development of surface materials with antimicrobial properties has become increasingly important, particularly in light of the recent rise in serious contact-borne diseases, such as the SARS-CoV-2 pandemic in 2020 [67,68]. Cross-contamination due to contact with infected surfaces has significantly contributed to the spread of pathogens. At the same time, the growing emergence of multidrug-resistant bacteria and frequent cases of food contamination by pathogenic microorganisms have prompted researchers to develop materials that can function as antimicrobial agents [69].

The incorporation of metal oxide nanoparticles into biopolymer-based films has gained growing attention due to their multifunctional role in enhancing the performance of packaging materials [70–73]. When integrated into polysaccharide matrices such as carboxymethyl cellulose (CMC) and kefiran, nanoparticles like zinc oxide (ZnO), titanium dioxide (TiO_2), and copper oxide (CuO) can significantly improve mechanical strength, decrease water vapor permeability, enhance UV-blocking capacity, and introduce or reinforce antimicrobial properties[65,74,75] (Figure 1.4). Additionally, these nanoparticles are generally safe and non-toxic[74]. These nanocomposite structures benefit from the synergistic interaction between the biopolymer matrix and the dispersed nanoparticles, making them particularly attractive for active food packaging applications, as they can increase the shelf life of fruit and other foods [75].

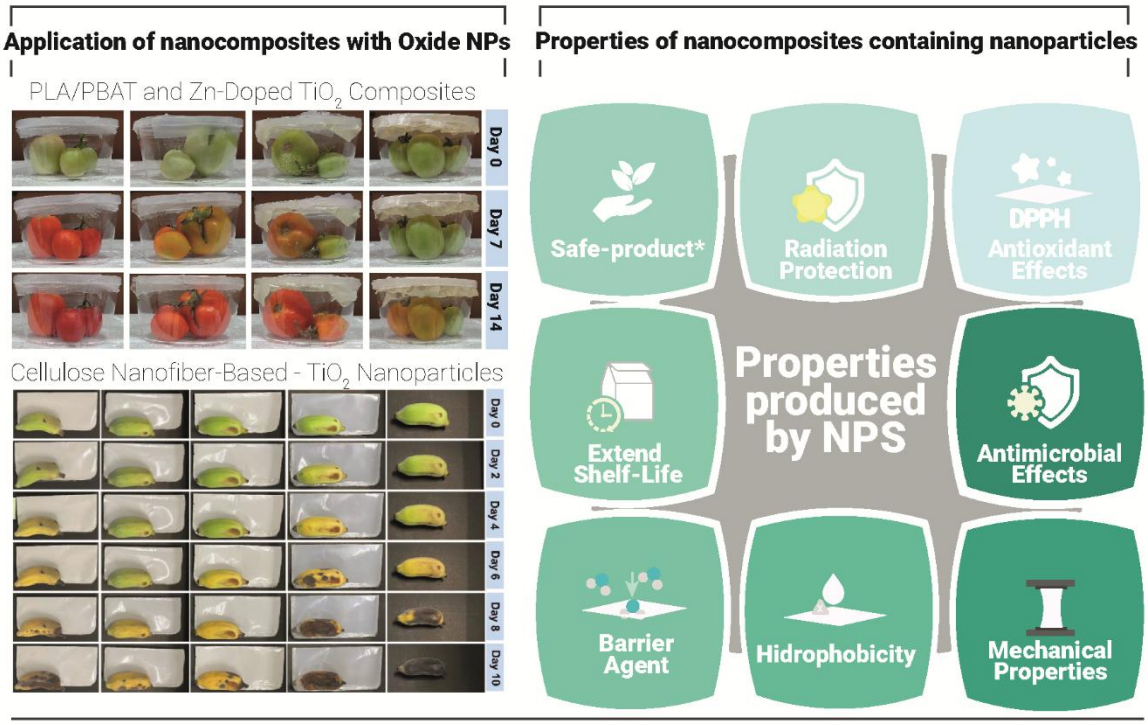

FIGURE 1.4 - Application of nanocomposite films containing TiO_2 NPs for the preservation of tomatoes and bananas [76,77]. Main properties required of nanocomposites containing oxide NPs, and Main parameters involved in the controlled synthesis of oxide nanoparticles.

In this context, various types of TiO_2 nanotubes have already been applied to cellulose nanofibril (CNF) films, protecting them from UV rays and enhancing their barrier to ethylene gas, a gas responsible for accelerating the deterioration of fruits such as tomatoes (Figure 1.4). Similarly, Hasheminya et al. (2018)[74] produced nanobiocomposite films of copper oxide–carboxymethyl cellulose–kefiran and observed that increasing the concentration of CuO NPs helped reduce water vapor permeability and enhance the tensile strength of the films. Furthermore, the uniform dispersion and optimal concentration of nanoparticles were shown to be critical factors influencing the final performance of these films. In a subsequent study, Hasheminya et al. (2019)[73] demonstrated that the addition of *Satureja Khuzestanica* essential oil to the CMC–kefiran–CuO NPs nanocomposite further improved the antimicrobial efficacy of the films, particularly against *Staphylococcus aureus* and *Escherichia coli*.

Despite the essential antimicrobial contribution of these NPs to the development of functionalized nanocomposite films, a significant gap remains between their conceptual design and application [78,79]. These NPs are typically synthesized through multistep processes, beginning with the precipitation of metal ions in aqueous media, followed by thermal treatment [80]. However, rapid precipitation kinetics often limit precise control over the size and morphology of the resulting hydroxide or hydroxycarbonate intermediates [81]. Furthermore, high-temperature calcination, commonly employed to convert these intermediates into crystalline oxides, can lead to undesirable particle agglomeration and dense aggregate formation, which may compromise the functional performance of the final nanomaterials [82].

In this context, selecting an appropriate synthesis route and fine-tuning processing parameters are crucial for obtaining ZnO NPs with optimal physicochemical characteristics. Factors such as particle size, distribution, surface charge, and compatibility with the polymer matrix must be carefully controlled to ensure consistent performance, safety, and scalability in real-world applications. Among the various candidates, ZnO NPs have gained prominence due to their ease of synthesis, low cost, and robust antimicrobial properties, making them ideal for incorporation into biodegradable film matrices aimed at food packaging and preservation [83–85].

1.5 Zinc Oxide Nanoparticles and their antimicrobial mechanisms of inactivation

Beyond their well-established role in enhancing the functional properties of biodegradable films, ZnO NPs also exhibit remarkable antimicrobial properties, including antibacterial, antifungal, and anti-inflammatory effects, combined with low cytotoxicity [86–90]. These characteristics make them highly attractive for applications in active packaging and biomedical fields. Their

effectiveness can be further optimized through precise control over key physicochemical parameters such as morphology, lattice defects, and surface chemistry [87]. Control over morphology, lattice parameters, and defect formation can be achieved not only by altering the metal precursors, but also by modifying the synthesis method, heat treatment duration and temperature, as well as the pH of the medium [91]. Silva et al. (2023)[79], for instance, demonstrated that it is possible to fine-tune the synthesis parameters for hierarchical 3D ZnO nanostructures using Central Composite Design (CCD) and Principal Component Analysis (PCA). Through careful adjustment of solvent proportions and physical conditions, the study successfully produced ZnO structures with high photocatalytic efficiency.

In a complementary approach, Sahu et al. (2021)[92] showed that altering the metal precursor allowed control over the morphology of ZnO nanoparticles, yielding nanogranules, hexagonal pillars, and nanorods. This work highlights the critical role of the counter-ion in determining nanoparticle shape and, consequently, functional behavior. The choice of precursor directly influences the arrangement of atoms within the crystal lattice, the exposure of polar or apolar surfaces, and the preferential orientation of ZnO nanoparticle planes [93]. In addition, using different Zn^{2+} salt precursors can guide preferential growth along axial or radial directions due to the various interactions between ZnO facets and the anions of the metal precursors [94]. These structural variations can significantly impact surface energy, reactivity, and interaction with biological or chemical species, making precursor selection a key factor in tailoring ZnO for specific applications, such as antimicrobial films and photocatalytic systems [80]. This tunability underscores zinc oxide's potential for diverse applications, particularly in reinforcing nanocomposite films.

On the other hand, the microwave-assisted hydrothermal (HaM) method is also widely known for being simple, environmentally safe, economical,

and easily adjustable to produce ZnO NPs with various morphologies [95]. Variables such as temperature, irradiation time, and pressure can be easily changed and investigated through experimental design approaches utilizing HaM [96]. Gusmão et al. (2021)[97] observed that the morphology of pure and Ag-doped ZnO using the HaM method depends on the alkaline medium in which the nucleation process occurs. When comparing the biocidal effect of ZnO obtained with NaOH and NH_4OH, pure samples exhibit more significant antimicrobial activity against *Saccharomyces cerevisiae*, as observed in the medium containing ammonium hydroxide at pH 12. González et al. (2021)[98] observed that changing the morphology of ZnO NPs (from spherical to hexagonal and rod shapes) significantly affected their antibacterial and anticancer activity. Mainly, NPs with spherical shapes showed more excellent biocide effects than hexagonal particles, increasing oxidative stress and apoptosis in cancer cells. This is because the shape of the NPs is fundamental to their antimicrobial efficacy, as one of the primary mechanisms involves direct contact through electrostatic interactions between the NP surface and the microbial envelope [80,99].

Although the mechanisms of antimicrobial action of oxide NPs have not yet been fully elucidated, the release of ions and the indirect mechanism of forming reactive oxygen species (ROS) are two frequently reported means of damaging microorganisms. ROS generation can oxidize microbial cell walls, causing irreversible damage to cellular components (Figure 1.5). This was demonstrated by Marques et al. (2023)[100] in a study involving silver nanoparticles (AgNPs) loaded onto silica (SiO_2) and immobilized on leather. The AgNPs exhibited antimicrobial activity by disrupting the protective envelope of bacteria and viruses, including SARS-CoV-2. To investigate the underlying mechanism, the authors employed specific scavengers such as ascorbic acid (AA), $AgNO_3$, p-benzoquinone (*p*-BQ), ammonium oxalate (AO), and tert-butyl alcohol (TBA) to inhibit •OOH, e^-, $•O_2^-$, h^+, and •OH species, respectively. A reduction in the photodegradation efficiency of the nanoparticles in the presence of any of these

scavengers indicated the involvement of the corresponding species in the material's antimicrobial activity[101]. Interestingly, ZnO NPs can generate ROS even in the absence of light [102]. However, ROS production is significantly enhanced under light exposure due to their photocatalytic properties [99,103]. The formation of ROS by ZnO NPs depends on several physicochemical parameters, including particle size, shape, and surface charge, as well as structural differences between the cell walls of Gram-positive and Gram-negative bacteria (Figure 1.5) [104,105].

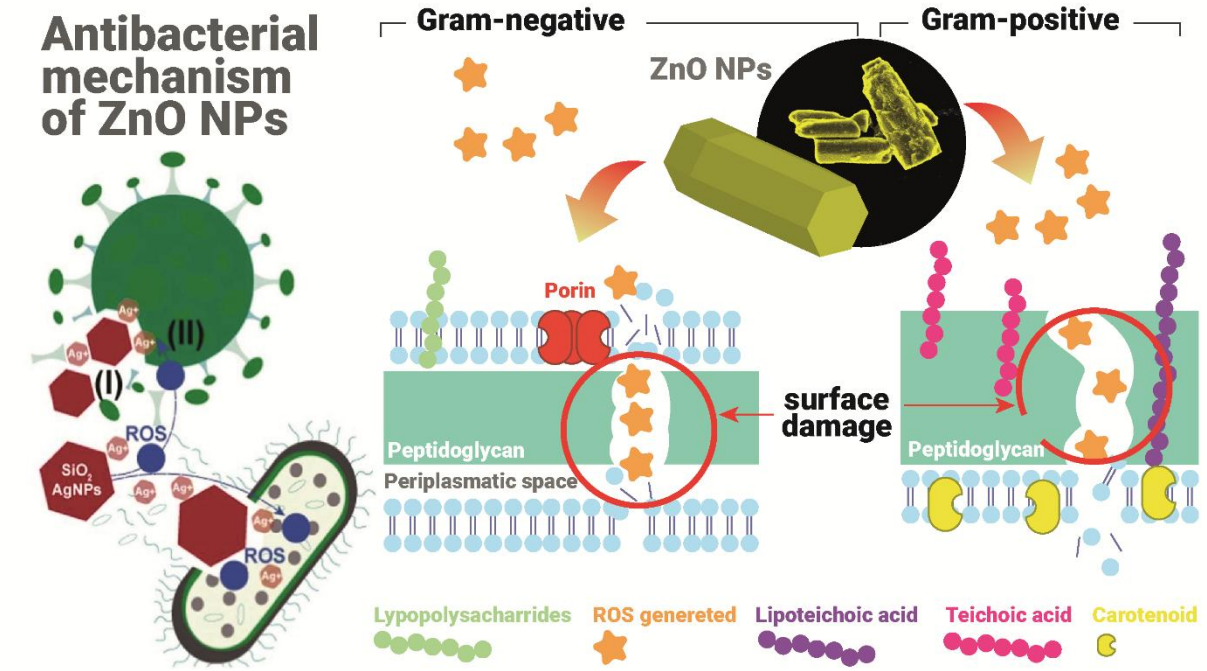

FIGURE 1.5 - Schematic illustration of the antibacterial mechanism of ZnO NPs on Gram-negative and Gram-positive cell structures through the action of ROS generation

All these mechanisms can compromise the integrity of the cell membrane, ultimately leading to bacterial inactivation[106,107]. Moreover, the release of ions and the production of nanoparticles with high surface exposure enhance their interaction with microorganisms, an effect that is strongly influenced by the synthesis method employed.

2. GOALS

This study aims to develop nanocomposite films based on kefiran, carboxymethyl cellulose, and ZnO nanoparticles, with enhanced functional properties for application in food packaging. To this end, a set of specific objectives was defined to enable a more in-depth investigation of key aspects of the study.

a. To extract, purify, and characterize kefiran obtained from kefir grains, and to evaluate its antimicrobial, antibiofilm, and antifungal activities, as well as its potential application as an edible coating for strawberry preservation under ambient and refrigerated conditions;

b. To optimize the synthesis of ZnO nanoparticles by systematically varying experimental parameters, such as the metal precursor type, alkaline medium (using different bases), and microwave irradiation time, and to evaluate the effect of these variables on the antimicrobial performance of the resulting nanoparticles;

c. To propose a mechanism of antimicrobial action for the synthesized ZnO nanoparticles, based on their physicochemical properties and interactions with microbial cells, including activity screening against clinically relevant ESKAPE pathogens;

d. To optimize CMC film production, the solvent casting method was studied, modifying CMC concentration.

e. To evaluate the effect of incorporating ZnO NPs at different concentrations into kefiran/CMC-based films on their mechanical, optical, and barrier properties (including WVP and WCA), as well as their structural, morphological, and antimicrobial performance,

aiming at the development of multifunctional nanocomposites for food packaging applications.

Chapter 3 EXPERIMENTAL SECTION

The methodology of this research is divided into four parts. The first section covers aspects of the kefiran biopolymer, including extraction, purification, characterization, and applications as edible film. The second involves synthesizing and characterizing ZnO nanoparticles, as well as their antimicrobial response against multi-resistant bacterial pathogens. The third part presents the process of producing films from CMC and Kefiran, optimizing casting process parameters. Finally, the barrier, mechanical, wettability, and antimicrobial properties of the nanocomposite films, in which ZnO NPs were added at different concentrations, will be discussed.

3.1 Part I: Obtaining kefiran, characterization, and application as an edible coating

3.1.1 Cultivation of kefir grains, extraction, and purification of kefiran

The kefir grains and grade A pasteurized milk (sonho de leite) were purchased at the municipal market in São Carlos, SP, Brazil. The milk was used as a carbon source for the growth of the bacterial culture that makes up the grains. The Kefir cultivation process started with the daily fermentation of 1 L of pasteurized type A milk (Figure 3.1), containing 20 g of the grains for 24 h at room temperature in a beaker without stirring [108]. The grains were separated from the milk daily by filtering through a plastic sieve. After this process, a new volume of milk (1 L) was added to the beaker, and the process was repeated uninterrupted for 30 days to obtain the required quantity for kefiran extraction. The biopolymer extraction and purification process was based on a previous methodology proposed by Piermaria et al. (2011)[43] with some modifications, as shown in the flowchart in Figure 3.1. Briefly, 10 g of kefir grains, previously washed with

distilled water, were added to a beaker containing 100 mL of deionized water, and stirred and heated at 80 ºC for 1 h. The solution was then centrifuged at 10.000 rpm for 20 min at a temperature of 20 ºC (Thermo Scientifi Sorvall RC 6 Plus Centrifuge). The resulting supernatant was separated from the precipitate, then added to 30 mL of cold ethanol (95%), and refrigerated for 18 h at -20 ºC to precipitate the polysaccharide in the supernatant. Subsequently, the samples were thawed slowly and centrifuged at 10,000 rpm for 20 min at 4 ºC. The EPS was purified by redissolving the samples in 200 mL of deionized water and repeating the process twice, followed by lyophilization using a Lablyo Plus freeze-dryer.

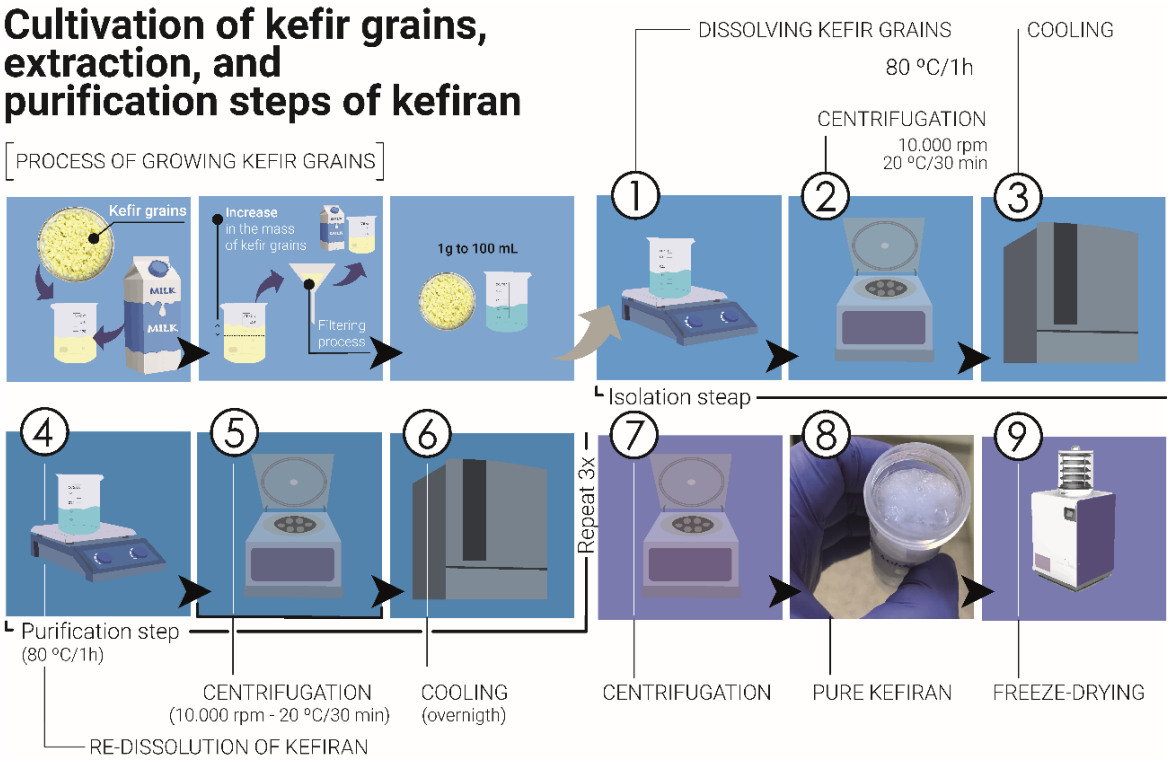

FIGURE 3.1 - Flowchart of the kefir cultivation, kefiran extraction, and purification process.

3.1.2 Characterization of the kefiran

The lyophilized polymer was ground using a grinder. Then, the kefiran powder was analyzed by attenuated total reflectance Fourier-transform infrared (ATR-FTIR) to identify the groups present in the polymer structure. The

measurement was carried out using a Shimadzu model IRAffinity 1 spectrophotometer in the 500 to 4000 cm^{-1} region using 54 scans and a resolution of 4 cm^{-1}. The kefiran powder was solubilized in deuterated water (D_2O). The ^{1}H and ^{13}C NMR spectra were recorded at a temperature of 27 °C on a Bruker AVANCE III NMR spectrometer (operating frequencies of 400 MHz for ^{1}H NMR and 101 MHz MHz for ^{13}C NMR). The chemical composition of kefiran powder was analyzed by X-ray photoelectron spectroscopy (XPS) using a Scientia Omicron ESCA+ spectrophotometer equipped with a monochromatic Al-Kα X-ray source (1486.7 eV) with an incident power of 280 W and a constant power mode of 50 eV. The XPS spectra were analyzed using the Casa-XPS software calibrated by the C 1 s peak, whose binding energy is around 284.8 eV. The crystallographic structure of the polymer was investigated by X-ray diffraction (XRD) using the Shimadzu diffractometer model XRD-6100 (Shimadzu Corporation, Japan). The measurement was carried out under Cu-Kα radiation (λ = 0.154 nm) using a scanning range of 5-90° (2θ), a rate of 0.05 °/s, and a voltage of 40 kV. The intensity of the diffractogram was previously normalized using PeakFit v4.12 software (SeaSolve Software, USA). The kefiran morphology lyophilized was observed using scanning electron microscopy by field emission (FE-SEM) using a ZEISS model SIGMA microscope.

3.1.3 Antifungal activity of Kefiran

Fungal strains of economic importance for strawberry cultivation, including *Fusarium solani*, two strains of *F. oxysporum*, and *Alternaria alternata*, were used in this study. The strains were obtained from the microorganism bank of the Laboratory of Microbiology and Biomolecules (LaMiB) at the Federal University of São Carlos. For reactivation, the strains were cultured on potato dextrose agar (PDA) medium and incubated at 28 °C for 7 days, ensuring proper growth and viability of the isolates. Previously crushed, 1.3 g of freeze-dried kefiran was solubilized entirely in deionized water under stirring and heating at

50 ºC. Subsequently, the fungal strains were inoculated onto PDA medium at different concentrations of the kefiran exopolysaccharide (13, 26, 39, 52, 65, 78µg/L). The experiment was conducted in triplicate for each concentration. The negative control consisted of plates containing PDA medium inoculated with the same strains without adding the exopolysaccharide. Once full fungal growth was achieved in the control plates, the kefiran-treated plates were examined for observable effects, such as growth inhibition, morphological alterations, changes in pigmentation, and impacts on sporulation. These parameters were carefully recorded to assess the exopolysaccharide's broader impact on the fungi's morphology.

3.1.4 Determination of Biofilm Eradication Capacity

The effect of kefiran on preformed biofilm was evaluated according to QIN[109], with modifications. This study used *Staphylococcus epidermidis* ATCC 35984, a potent biofilm-forming strain, as a positive control, and *S. epidermidis* ATCC 12228, a weak biofilm-forming strain, as the negative control. A single colony of each strain was taken from the overnight culture on brain heart infusion (BHI) agar and pre-cultured in BHI broth supplemented with 0.75% (w/v) glucose at 37 ºC for 24 h. The bacterial cultures were then adjusted using a Spectramax M5 (Molecular Devices, San Jose, CA, USA) to an optical density at 600 nm of 0.9 to 1.1 in phosphate-buffered saline (PBS; pH 7.4), transferred to a flat-bottom 96-well polystyrene microplate, and incubated at 37 ºC for 24 h to allow biofilm formation. The wells were washed three times with PBS to remove the planktonic cells. The biofilm was then incubated at 37 ºC for 24 h in fresh BHI broth supplemented with glucose for the control wells or in BHI containing kefiran at 512 mg/L for the test wells. After this period, the microplate was washed three times with PBS, stained with 0.2% (w/v) crystal violet for 15 min, and washed again three times with PBS. Finally, the stained biofilm was resuspended with

ethanol: acetone (80:20) solution, transferred to another microplate, and analyzed at 595 nm. Each condition was tested with 12 replicates.

The test control compares the average absorbance of *S. epidermidis* ATCC 35984 biofilm and the average absorbance of *S. epidermidis* ATCC 12228, both without compound. As for the compound's ability to eradicate biofilm, the data was analyzed by comparing the biofilm production of *S. epidermidis* ATCC 35984 with kefiran and *S. epidermidis* ATCC 35984 without the polymer. To do this, the average of the replicates and the standard deviation are used to analyze the consistency between the replicates. For the statistical evaluation, analysis of variance (ANOVA) was carried out on the mean absorbance of biofilm production by the *S. epidermidis* ATCC 35984 strain without kefiran and the mean absorbance of biofilm production by *S. epidermidis* ATCC 35984 in the presence of the polymer. The means were compared using the Student's t-test, whose P-value <0.05 indicating a statistically significant difference between the two samples. Similarly, when the analysis of variance (ANOVA) yelds a $P < 0.05$, it also indicates a significant difference.

3.1.5 Preparation of edible coating solutions and their application to strawberries

The fresh strawberries with an average size of 25 mm and no surface damage, purchased from a local market in Barcelona (Spain), were used in the shelf-life tests. First, the strawberries were thoroughly washed with distilled water and left to dry at room temperature (25 ºC) for approximately 20 min before being coated with the kefiran solutions. The strawberries used in the tests were divided into two groups: the first was stored at 5 ± 2 ºC, and the second at room temperature. Both groups consisted of strawberries with and without the polymer solution. Some strawberries were coated entirely with the kefiran solution, which had been previously prepared using an immersion technique. This technique

involves completely immersing the strawberry in the polymer solution and then drying it at room temperature. The kefiran solution was prepared by dissolving 1.3 g of the polymer (the initial mass used for the antifungal and antibiofilm tests) in 100 mL of water at 50 °C, and it was kept under constant stirring for 1 h. The coating process was followed by drying the strawberries at room temperature (± 20 ºC) for 1 h. The samples stored in the refrigerator were tested at 0, 3, 6, 9, 12, and 15 days. Samples at room temperature were tested at 0, 3, 6, and 9 days.

The weight loss of each group of strawberries stored at room temperature and under refrigeration was determined as the change in fruit weight measured every 3 days according to Equation 1, in which W_o represents the weight of fruits on day 0, while Wt is the weight in each analysis day.

$$\text{Weight loss (\%)} = \frac{Wo - Wt}{Wo} \text{ x } 100 \quad (1)$$

Every 3 days, 3e strawberries from each group were crushed using a household crusher until all the fruit appeared like a paste. Subsequently, 10 g of the paste produced was diluted in 50 mL of deionized water, and the resulting juice was filtered using filter paper. The pH of each sample was determined using a previously calibrated pH meter (Metria – M21). The methodology described by Al-Hilifi et al. (2024)[9] and Li et al. (2024)[56,110] with modifications, were used to determine the titratable acidity of the strawberries. 10 mL of the juice produced was diluted in 50 mL of distilled water, and then 3 drops of 1% phenolphthalein solution were added. Titration was carried out with a 0.1 M NaOH solution until a pink color appeared. The TA value was calculated using Equation 2.

$$\text{TA}(\%) = \frac{V.n.f}{V_j} \times 100 \quad (2)$$

Here, *V* corresponds to the volume of NaOH solution used to reach the pink color in the juice titration, *n* is the exact normality value of the 0.1 N NaOH solution, and f is a correction factor equal to 0.064 which represents the equivalent

amount in grams of citric acid for 1 mL of 0.1 N NaOH solution. *V* represents the volume of juice used in the titration.

A portable refractometer (Iorben profissional atc brix 0-32% Brix) was previously calibrated using deionized water to determine the total soluble solids (TSS) content. The experiments were performed in triplicate, and the data obtained was expressed in ºBrix. The possibility of significant differences between the results obtained was assessed using Student's t-test at a probability level of $P < 0.05$. The null hypothesis stated that the samples were identical. In cases where the calculated t-values were more significant than the tabulated values, the differences between the samples were considered necessary, and the null hypothesis was rejected.

3.2 Part II: Synthesis of ZnO NPs, characterization, and antimicrobial studies

3.2.1 Synthesis of ZnO NPs

In the preparation of the ZnO NPs, 50 mL of the ($Zn(NO_3)_2 \cdot 6H_2O$ or $Zn(CH_3COO)_2 \cdot 2H_2O$) solution, at a concentration of 0.06 M prepared with deionized water, was added in a beaker and kept under stirring at 60 °C for 20 min. Subsequently, 50 mL of a 1.2 M alkaline solution (NaOH or NH_4OH) was continuously dropped into the salt solution, as illustrated in Figure 3.2. During this process, the color change of the solution was observed as the ZnO precipitates were being formed. Then, the resulting solution was transferred to a Teflon-lined stainless-steel autoclave (100 mL) and heat treated in a microwave at 120 °C for different times (15 or 30 min). The white precipitate from this process was washed successively with distilled water and ethanol to remove impurities and then dried in an oven at 60 °C for 24 h. All reagents used in the synthesis of ZnO were of analytical grade. The samples produced were identified as shown in Table 1.

Table 1. Identification of the samples and characteristics related to each synthesis.

Identification samples	Characteristic		
	Metallic precursor	Base	Irradiation time (min)
ZnO – 1	$Zn(NO)_3$	NaOH	15
ZnO – 2	$Zn(NO)_3$	NaOH	30
ZnO – 3	$Zn(CH_3COO)_2$	NaOH	15
ZnO – 4	$Zn(CH_3COO)_2$	NaOH	30
ZnO – 5	$Zn(NO)_3$	NH_4OH	15
ZnO – 6	$Zn(NO)_3$	NH_4OH	30
ZnO – 7	$Zn(CH_3COO)_2$	NH_4OH	15
ZnO – 8	$Zn(CH_3COO)_2$	NH_4OH	30

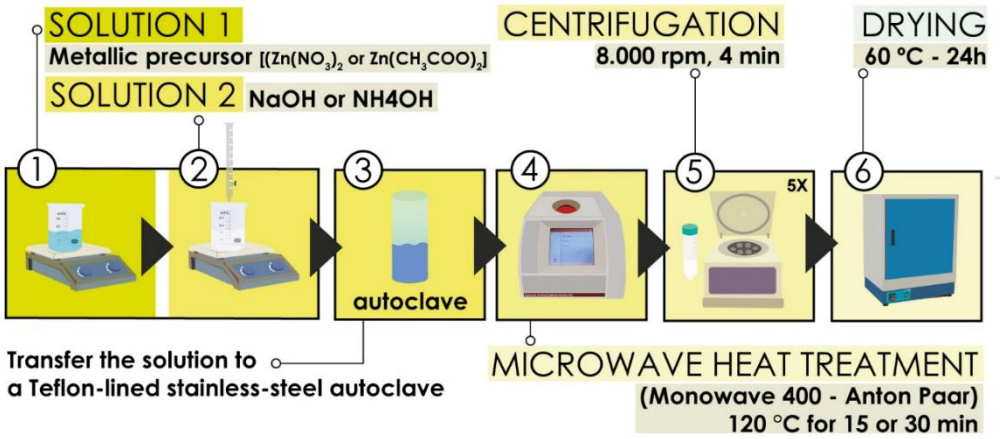

FIGURE 3.2 - Illustration of the steps adopted in synthesizing ZnO NPs by the microwave-assisted hydrothermal method.

The analysis of the crystalline structure of the powders was performed from X-ray diffraction (XRD) using a Shimadzu diffractometer model XRD-6100 with a range of 10-110º (2θ) voltage of 40 kV and a rate of 0.05 º/s. An additional study of the ZnO phase to investigate possible changes in the network parameters

of the materials was carried out from the Rietveld refinement using the General Structure Analysis System II (GSAS II) software[111]. The NPs' morphology was observed using scanning electron microscopy by field emission (FE-SEM) using a ZEISS model SIGMA microscope. Compositional analysis of the chemical elements in the samples was performed by dispersive X-ray spectroscopy (EDS) using an accelerating voltage of 10 and 20 kV on a Hitachi microscope, TM4000 Plus, with an integrated backscattered electron detector (BSE). The band gap values of the materials were calculated from the Kubelka-Munk method using the UV-vis spectra obtained using a Cary 7000 spectrophotometer coupled with an integrating sphere in the diffuse reflectance (DRS) mode in the region between 200 - 800 nm[112]. Zeta potential was respectively measured on a Malvern Zetasizer® nanoZS-equipment in pH = 6.5 (no adjustment).

3.2.2 Screening of Antibacterial Activity

The antimicrobial activity of ZnO NPs was evaluated against Gram-positive *S. epidermidis*, *S. aureus* ATCC 25923, *S. aureus* ATCC 8095, *E. faecalis* ATCC 29212, *E. faecium* ATCC 700221 and Gram-negative, *K. pneumoniae* ATCC 700603, *E. coli* 25922, *A. baumannii* ATCC 19606, and *P. aeruginosa* ATCC 27853 bacteria. Some of these bacteria are responsible for severe infections and have become resistant to many antibiotics and, because of this, are listed by the WHO as critical and priority pathogens[113]. To study the antibacterial activity of different ZnO-NPs, 5120 mg/L of the powders was prepared from dispersion in water and autoclaved to avoid contamination. Subsequently, the stock suspension was diluted at a ratio of 1:10 in Mueller Hinton Cation Adjusted Broth (MHCA) (BD, East Rutherford, NJ, USA) containing Biolog Redox Dye Mix H (100x) (Biolog, Hayward, CA, USA) at a ratio of 1.05%. After that, each ZnO-NPs was tested at 512 mg/L, and the inoculum was added as CLSI recommended for the broth microdilution method. The bacteria are grown in MHCA broth without ZnO NPs for positive control. The MHCA broth was conditioned without

the bacteria and ZnO NPs to show no contamination for the negative control. The incubation was performed at 36 °C ± 1 °C, and the reading of the results was done using the OmniLog® (Biolog, Hayward, CA) equipment every 15 min in the period of 24 h using Biolog's OmniLog Data Collection v. 3.0 software [114]. In the absence of bacterial metabolism, the screening was considered positive, indicating the occurrence of antibacterial activity at the concentration tested. The Minimum Inhibitory Concentration (MIC) in this case was ≤ 512 mg/L. In the presence of bacterial metabolism, the screening was considered negative, indicating the absence of antibacterial activity at the concentration tested. The negative screening does not exclude the possibility that this compound exhibits antibacterial activity at higher concentrations, so the result is expressed as ">512 mg/L". All assays were performed in triplicate, and both controls received Biolog Redox Dye Mix H (100×) in the same proportion.

3.2.3 Determination of the Minimum Inhibitory Concentration (MIC)

After a screening step, the ZnO NPs that inhibited the bacterial metabolism at 512 mg/L were tested against these bacterial isolates to determine the MIC. Daptomycin and imipenem (Gold Biotechnology, St. Louis, MO, USA) were used as controls against the Gram-positive and Gram-negative bacterial isolates, respectively. Daptomycin stock solution and broth were prepared as CLSI (2013) recommended. Serial dilutions (1:2) of ZnO NPs, daptomycin, and imipenem at 512 mg/L were prepared in MHCA broth plus 1× Biolog Redox Dye Mix H, ranging from 0.06 mg/L to 512 mg/L. Each dilution was tested against 10^5 CFU/mL of each bacterium in a final volume of 100 µL in a 96-well microplate to determine the ZnO NPs MIC. The microplates were incubated in the OmniLog apparatus (Biolog, Hayward, CA, USA) at 36 °C ± 1 °C for 24 h, with readings taken every 15 minutes. This was followed by a final visual observation of the plates to monitor the kinetics of bacterial metabolism. MIC was considered the

lowest concentration of the compound that inhibited the bacterium's metabolism. In the positive control, bacteria were added to the broth without ZnO-NPs to show they could grow in MHCA broth. In the negative control, only MHCA broth, without bacteria, was used to prove that no broth contamination occurred; both controls also received 1× Biolog Redox Dye Mix H. All assays were performed in triplicate.

3.2.4 Antimicrobial Mechanism Studies: ROS production and Zn^{2+} leaching

In a 100 mL glass beaker, 50 mg of photocatalyst and 50 mL of MB 20 mg L^{-1} solution were added. The mixture was stirred in the dark for 30 min to reach adsorption-desorption equilibrium and then irradiated for up to 60 min in a reactor containing 6 UV-C lamps (254 nm). Details of the reactor used in this study can be found in Moreira et al. (2019)[115]. At each 10 min interval, an aliquot of the sample (1 mL) was taken and subjected to centrifugation to separate the catalyst from the supernatant, which was then analyzed by UV-Vis spectrophotometry in scanning mode, using a wavelength range of 500 to 700 nm. To investigate degradation mechanisms, studies using 2 mmol silver nitrate ($AgNO_3$ - Sigma-Aldrich ≥ 99.0%), *tert*-butanol [$(CH_3)_3COH$ - Sigma-Aldrich ≥ 99.5%], methanol (CH_3OH, Sigma-Aldrich ≥ 99.8%), and 0.002 mol de p-benzoquinone ($C_6H_4O_2$ - Sigma-Aldrich ≥ 98.0%) as interfering/scavenger of reactive species of the electron, hydroxyl, hole, and superoxide types, respectively (e^-, OH^-,h^+ and O_2^-) [116]. Additionally, the specific probe assay for hydroxyl radicals using coumarin was performed as described in the literature by Moreira et al. (2020)[117]. To follow Zn^{2+} leaching after 60 min of irradiation using the photocatalytic conditions described above, the samples were filtered through a 0.22 μm membrane, the filtrate transferred to a polypropylene tube, acidified to 1% (v v^{-1}) with nitric acid (Sigma Aldrich, 65%) and analyzed by flame atomic

absorption spectroscopy (FAAS) using the same methodology described in Moreira et al. (2020)[117].

3.2.5 Statistical Treatment

Principal Component Analysis (PCA) is a widely employed statistical technique to uncover meaningful patterns and reduce the dimensionality of complex datasets[118]. In this study, particularly the analysis of MIC bacterial data, PCA offers a valuable approach to gaining insights from multidimensional information. The experimental procedure involved first collecting MIC values, which were organized into a matrix with antimicrobial agents as rows. PCA, using auto-scaling as a preprocessing step, was the default method of data analysis. By performing PCA on this matrix, the variability in MIC values was transformed into a set of orthogonal components known as principal components. Data import, pre-processing, and constructing multivariate models were performed within the R statistics platform (R Foundation for Statistical Computing) version 4.3.1 environment[119]. These components are ordered by the amount of variance they explain in the original data. This transformation highlights the most significant patterns and relationships between bacterial strains, antimicrobial agents, and their corresponding minimum inhibitory concentration (MIC) values.

3.3 Part III: Study of the production of films with and without nanoparticles

3.3.1 Sample preparation

The study on optimizing CMC production films was conducted using the solvent-casting method. The first part of this study investigated how changing the CMC concentration could influence the properties of the films that would later be produced with kefiran. All the steps of the film's production are illustrated in Figure 3.3a. First, for the complete homogenization of the different systems, each

solution of CMC was kept under constant stirring for a period of 24 h, without the use of heating, to avoid the formation of bubbles that could compromise the surface uniformity of the film and, consequently, its mechanical properties (step 1). After this period, volumes of 25 mL and 32.5 mL (corresponding to an additional 30% compared to the initial volume) of the solution were poured into PVC Petri dishes and left in a controlled oven at 30 ºC ± 2 ºC with air circulation for 24 h (step 2). After this time, the films were carefully removed from the plates and stored for the tests (step 3).

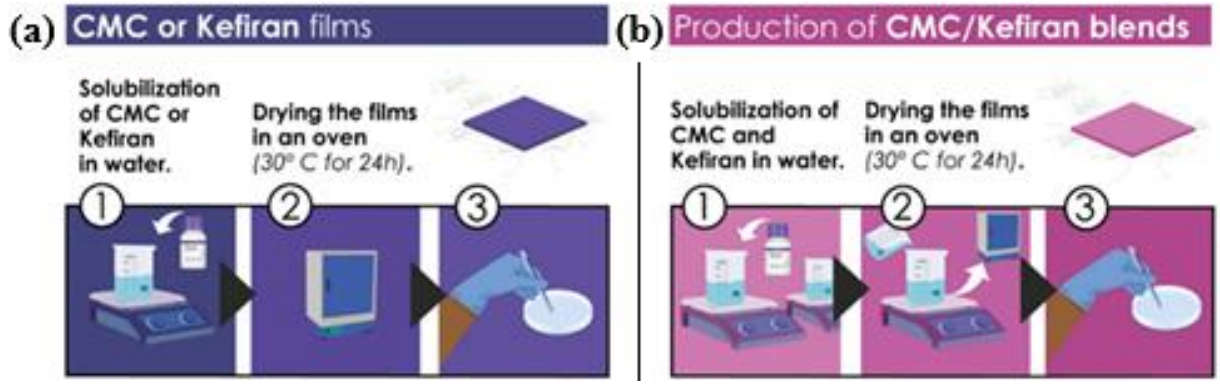

FIGURE 3.3 - Schematic of the manufacturing method for CMC films and CMC/Kefiran blends

To produce a blend with kefiran and CMC, 1.3 g of kefiran powder was initially added to 100 mL of distilled water and stirred constantly for 1 h at 50 ºC under heating (step 1 – Figure 3.3b). The kefiran used in this step was extracted, purified, and characterized as described previously in session 3.1.1. Following this, the kefiran solubilized was mixed in a CMC solution in the same proportion and kept under constant stirring for 24 h. Finally, 32.5 mL of the solution was poured into PVC Petri dishes and left in a controlled oven at 30 ºC ± 2 ºC with air circulation for 24 h (step 2). The films were carefully removed from the plates and stored for the tests (step 3). Codes were organized to facilitate the identification of all films produced, and the details are described in Table 2.

Table 2. Identification of samples according to film composition.

Sample ID	CMC Concentration (w/v)	Volume (mL)	Additional Components
A-32	1.0 g/100 mL	32.5	–
B-32	1.3 g/100 mL	32.5	–
C-32	2.0 g/100 mL	32.5	–
B-32-Gly12	1.3 g/100 mL	32.5	12% of glycerol
B-32-Gly25	1.3 g/100 mL	32.5	25% of glycerol
B-32-Gly50	1.3 g/100 mL	32.5	50% of glycerol
K-32	–	32.5	Kefiran only
K-32-G25	–	32.5	Kefiran + 25% glycerol
Blend	1:1 CMC:Kefiran mixture	32.5	25% glycerol

w/v represents the ratio between the CMC mass and the volume of water used to produce the polymer solution.

3.3.2 Film Characterization

3.3.2.1 Microscopy analysis, Thickness and Mechanical Assay

SEM images produced using a ZEISS Sigma microscope were used to observe the surface morphology and cross-section of the films to analyze whether the films were homogeneous and free of cracks. The film samples were fracture-prepared using liquid nitrogen and did not require coating. AFM images were produced in contact mode using a Bruker FastScan/Icon microscope from Bruker, USA to determine roughness parameters. The thickness of the films was measured at ten different points on each film using a digital micrometer (Mitutoyo Co., Kawasaki, Japan, MDC-25PX) with an accuracy of 0.001 mm. The mechanical properties of the prepared films were evaluated using the tensile strength (TS), elongation at break (EB), and Elastic modulus (EM), as per ASTM D882 (2018). This standard, specifically designed to determine the tensile properties of plastics in thin sheets and films, ensures the validity and comparability of our results. The

tests were conducted using film samples with dimensions of 60 mm in length and 7 mm in width and were performed on a universal testing machine, model MTS Adamel Lhomargy-DY34, equipped with a 10 kN load cell. The tests were conducted with an initial adhesion separation of 40 mm, and the speed used was 1 mm/min. Each group was tested using 10 samples.ASTM D882 (2018)

3.3.2.2 Water Contact Angle (WCA), Water Vapor Permeability (WVP), Moisture Content (MC), and Swelling Degree (SD)

The contact angle of the film surface using water as the solvent was determined using a goniometer (Ramé-Hart 260 F4) and the sessile drop method. Two drops were made per sample, and each sample was run in triplicate, with the behavior of the drop analyzed 10s after the drop was made. In addition, the hydrophilic/hydrophobic properties of the films were determined from the surface tension data using the Young-Laplace Theory, as described by BARBOSA[121]. The film's water vapor permeability (WVP) was measured gravimetrically, according to ASTM E96-80 (2000), with modifications proposed by CAZÓN[123]. The film samples were sealed in 10 mL of distilled water in test cells. The test cells were placed in a desiccator under controlled temperature and relative humidity (50 ± 5% RH and 30 ± 2 °C). The samples were weighed daily for 7 days to determine the water vapor transfer rate from inside the test cell to the silica. To determine the WVP value, it was necessary to establish the ratio between the change in mass obtained by weighing the test cells and the test time ($\Delta m / \Delta t$). This ratio is represented by the slope from the linear regression line formed by plotting the mass loss points against time, with an R^2 value greater than 0.99. The water vapor transmission rate (WVRT) value can be calculated using Equation 2.

$$\text{WVTR } \left(\frac{g}{s.m^2}\right) = \frac{\Delta w}{\Delta t.A} \quad (2)$$

Then, the ratio between the WVTR and the difference in the partial pressure of the water through the film (ΔP) was calculated, representing the

permeability value (Equation 3). In this case, 4245 Pa was used, which means the difference in water vapor pressure at 30 ºC [124,125]. The final step is multiplying the permeability value by the previously determined film thickness (Equation 4). Each test was performed in triplicate.

$$\text{permeance } \left(\frac{g}{s.m^2.Pa}\right) = \frac{WVTR}{\Delta P} \quad (3)$$

$$WVP\left(\frac{g}{s.m.Pa}\right) = \text{permeance.thickness} \quad (4)$$

The moisture content (MC) and degree of swelling (DS) of the films produced were determined using thermogravimetric tests[126]. Initially, 20 mm × 20 mm (w_1) samples were prepared and weighed. These samples were then placed in an oven at 110 ºC for 24 h to reach a constant weight. After this period, the samples had their weight determined (w_2) and were then immersed in a beaker containing 30 mL of distilled water and stirred under constant conditions for 24 h. The films were then carefully removed from the beaker and placed under a paper towel to remove excess water. The final mass of the films was obtained (w_3), and the MC and SD values were calculated using Equations 5 and 6.

$$MC\ (\%)\ \frac{(W1-W2)}{W1}\ x\ 100 \quad (5)$$

$$SD\ (\%)\ \frac{(W3-W2)}{W2}\ x\ 100 \quad (6)$$

3.3.2.3 UV-Vis and FTIR-ATR

The optical properties of the films were evaluated using a UV-Vis spectrophotometer (Cary 7000) calibrated in the 220-800 nm range at room temperature. The infrared spectra of the films produced were obtained at room temperature using a Shimadzu IRAffinity spectrophotometer, calibrated in Attenuated Total Reflection (ATR) mode with a resolution of 32 cm^{-1} and a range of 4000-600 cm^{-1}.

3.4 Part IV: Study of the nanocomposite films production

3.4.1 Nanocomposite film Characterization

3.4.1.1 Morphology , Structural and Chemical Characterization

The surface morphology and cross-sections of the nanocomposite films were observed using SEM, while their topography was scanned using the AFM technique. Both techniques were carried out in the same way as described above in section *3.2.2.1*. The crystal structure of the ZnO NPs and nanocomposite films was analyzed by XRD using a Shimadzu XRD-6100 diffractometer. Measurements were performed in the 2θ range of 5–80°, operating at 40 kV and with a step rate of 0.02°/s. Raman spectroscopy was used to investigate the vibrational modes of the samples. Measurements were obtained using a Witec alpha300 R micro-Raman system, coupled with a Nikon objective lens. The samples were excited using an Ar^+ ion laser (λ = 514 nm). X-ray photoelectron spectroscopy (XPS) was employed to evaluate the surface elemental composition and chemical states. The analyses were carried out using a Scientia Omicron ESCA+ spectrometer equipped with a monochromatic Al Kα X-ray source (1486.7 eV), operating at an incident power of 280 W and a pass energy of 50 eV in constant power mode. Spectra calibration was performed using the C 1s signal at 284.8 eV as an internal reference. Data analysis was conducted using CasaXPS software. The Raman bands were deconvoluted and fitted using PeakFit software. FTIR-ATR spectra of the films were acquired at room temperature using a Shimadzu IRAffinity spectrophotometer in ATR mode, with a resolution of 4 cm^{-1} across the range of 400–4000 cm^{-1}.

3.4.1.2 Thickness and Mechanical Assays

The thickness of the films was measured at ten different points on each film using a digital micrometer (Mitutoyo Co., Kawasaki, Japan, MDC-25PX)

with an accuracy of 0.001 mm. The mechanical properties of the prepared films were evaluated using the tensile strength (TS) response terms and Young's modulus (EM) values as defined in Equations 7 and 8, based on the ASTM D882 (2018), which is specific for thin plastic films and ensures the comparability of the results. Tests were performed on rectangular samples measuring 60 mm in length and 7 mm in width using a universal testing machine (MTS Adamel Lhomargy-DY34) equipped with a 10 kN load cell. The initial grip separation was set to 40 mm, and the test speed was 1 mm/min. Ten specimens per group were tested, and results are expressed as mean ± standard deviation.

$$\text{TS (MPa)} = \text{Fmax/ thickness} \tag{7}$$

$$\text{EAB (\%)} = \left(\frac{lmax}{lo}\right)\text{x}100 \tag{8}$$

3.4.1.3 WCA, WVP, Moisture Content (MC), and Swelling Degree (SD)

WCA was measured using the sessile drop method with a Ramé-Hart 260 F4 goniometer. WVP was determined gravimetrically according to ASTM E96-80 (2000). MC, SD, and other parameters commonly analyzed in CMC films were evaluated using the same methods.

3.4.1.4 Colorimetric Measurements (CIELAB) and UV-Barrier

Optical properties were evaluated through colorimetric and UV-barrier analyses. Color measurements were conducted using a digital spectrophotometer (Konica Minolta, Tokyo, Japan, model CR-400/410) based on the CIELAB system[127]. In this color space, L* represents lightness on a scale from 0 (black) to 100 (white). Positive a* and b* values correspond to red and yellow, respectively, while negative a* and b* values correspond to green and blue, respectively. UV-barrier, transparency, and opacity properties were assessed using a UV-Vis spectrophotometer (Cary 7000). To calculate Transparency and Opcity properties,

transmittance values at 280 and 660 nm were used and applied in Equations 9 and 10.

$$\text{UV-barrier (\%)} = \frac{\%T660}{\text{film thickness}}) \text{ x } 100 \quad (9)$$

$$\text{Transparency} = (-\log T_{600}/t)\text{x}100 \quad (10)$$

Where T660 and T280 represent transmittance at 660 and 280 nm, respectively, and $\boldsymbol{\tau}$ is the average film thickness in mm. To quantify ultraviolet (UV) radiation blocking, Equations 11 and 12 were applied to the UV-A (315–400 nm) and UV-B (280–315 nm) regions, respectively, using the average transmittance values within each range. All measurements were performed in triplicate.

$$\text{UV-A blocking (\%)} = 100 - T_{UV\text{-}A} \quad (11)$$

$$\text{UV-B blocking (\%)} = 100 - T_{UV\text{-}B} \quad (12)$$

Chapter 4 RESULTS AND DISCUSSION

4.1 Obtaining kefiran, characterization, and application as an edible coating

4.1.1 Characterization of kefiran using XRD, SEM, XPS, NMR, and ATR-FTIR

The X-ray diffraction pattern of kefiran powder, shown in Figure 4.1a, revealed a prominent peak observed at ~21° (2θ), which characterizes the polymer as semi-crystalline. This behavior agrees with what was reported by Exarhopoulos et al. (2018)[128]. The SEM images of the freeze-dried polymer (Figure 4.1b) show the presence of regions with different textures. Unlike what has already been reported in other work, residual microorganisms, such as bacteria, were not observed here, indicating the efficiency of the extraction procedure adopted for polymer [40]. In addition, the kefiran extraction process achieved a yield of 2%, similar to that reported by Montoille et al. (2021)[129]. Figure 4.1c shows the high-resolution XPS spectra for O1s and C1s. The central C 1s peak was broken down into four components, of which the binding energies of the peaks located at 286.1 and 287.3 eV show the presence of bonds between the hydroxyl group and carbon (C-OH) and C-O-C, respectively [130,131]. On the other hand, the deconvolution of the O1s spectrum resulted in two components positioned at 532 and 533.7, mainly attributed to the O - C and H - O - C bond [130]. The structure of kefiran was confirmed by ^{1}H and ^{13}C NMR analysis. Some signals appearing in the ^{13}C spectrum are related to the carbons present in the glucose ring in the pyranose form (Figure 4.1d); more specifically, the signals present at 75.56, 75.5, 75.3 and 71.6 indicate the carbons C-2, C-3 e C-4 present in the → 2,6) -b-D-Galp-(1 →, → 4) -b-D-Glcp -(1→, e → 4) -α-D-Glcp-(1→, respectively [129,132]. In addition, the peak located at 103.68 may be related to the presence of non-reducing terminal

carbon and internal α-(1→2)-D-pyranose units [129,132].

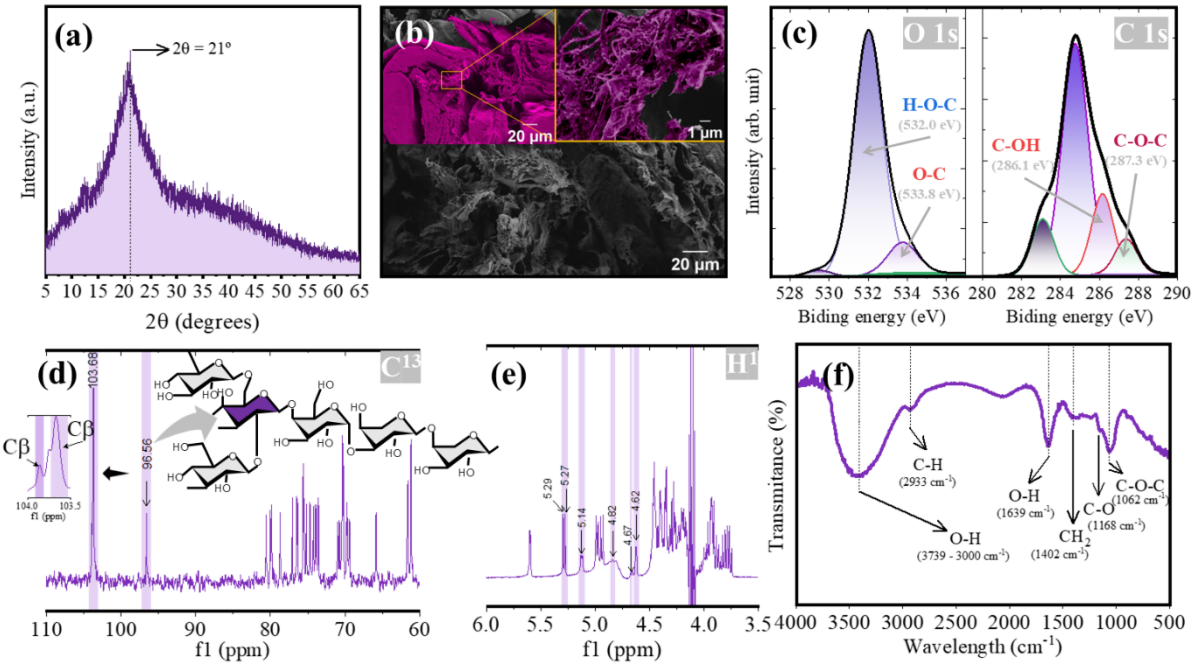

FIGURE 4.1 - (a) XRD, (b) SEM images, (c) O 1s and C 1s XPS spectrum, (d) C^{13}, (e) H^{1} RMN, and (f) FT-IR spectrum of kefiran extracted and purified.

Figure 4.1e shows 1H NMR signals located at 5.14, 4.82, 4.67, and 4.62, which are attributed to the presence of α-anomeric hydrogens and are like the signals reported by Radhouani et al. (2018)[130]. In addition, the signal present in 4.62 can be associated with the (1 → 6)-β-d-Galactose bond, which corresponds to the presence of anomeric protons from the β-D-Glcp-(1 →, → 2,6) - β -D-Galp-(1 →, → 6)- β -D-Glap-(1 →, → 4)- β -D-Glcp-(1 →, → 3)- β - D-Galp-(1 → and → 6)- β -D-Glcp-(1[132]. On the other hand, the signal located at 5.1 ppm may be related to the anomeric proton of → 4) -α-D-Galp-(1 →[132].

The ATR-FTIR spectrum shown in Figure 4.1f shows absorption bands in the region between 3430 and 2933 cm^{-1}, which are related to the presence of a significant number of O-H bonds in the polysaccharide [40,133–135]. The band at 2929 cm^{-1} is associated with the symmetrical and asymmetrical stretching of the CH bond present in the methyl (CH_3) and methylene (CH_2) groups [40]. The presence of vibration bands in the region between 1000 and 2000 cm^{-1}, characteristic of side groups and ring elongation with C - O - C, C - O – H, and C - H bonds are typical

of carbohydrates and confirms the purity of the polymer and the efficiency of the extraction and purification process [40]. The bands observed more specifically in the region of 1636, 1403, 1240, and 1064 cm^{-1} correspond, respectively, to the O-H vibration associated with the water molecule, C - H, C - OH, and C=O and are like those observed by Piermaría et al. (2016)[136] and Galdeano et al. (2009) [137].

4.1.2 Kefiran's antibiofilm and antifungal response

Biofilms represent a serious public health problem as they protect microbes from the action of antimicrobials, which can result in the persistence of infections and an increase in morbidity and mortality rates[138,139]. As well as posing a risk to the food chain, biofilms can also be found on medical devices such as catheters, in which case the microorganisms present can detach and infect patients even more seriously[139]. In this sense, searching for new molecules that can modify or prevent biofilm growth is the most effective strategy for treating chronic bacterial infections, rather than trying to get rid of the biofilm once it has formed[140]. Here, *S. epidermidis* ATCC 3598 strain was used to test the antibiofilm capacity of kefiran. Strain 35984 because it is a good biofilm-forming (Figure 4.2a). *S. epidermidis* ATCC12228 is a poor biofilm-forming strain used as a negative control in the assay. The comparison of the presence of biofilm between the strains showed a significant difference with $p<0.05$, showing that the controls used are significantly different in all cases. The ability to eradicate the biofilm formed by the *S. epidermidis* ATCC 35984 strain was analyzed in the presence of the kefiran polymer at a concentration of 512 mg/L. This compound decreased the pre-formed biofilm by 35.5% with a p-value below 0.001. According to Singh et al. (2021)[140], exopolysaccharides rarely have antibiofilm capacity, demonstrating the importance of this result for kefiran. Before the antibiofilm tests with kefiran, antimicrobial tests were carried out using 512 mg/L of kefiran with the same bacteria, but there was no inhibition. Based on this, it can be suggested that the reduction in biofilm occurs only through action on the matrix or alterations in

quorum-sensing and gene expression.

Sambanthamoorthy et al. (2014)[141] isolated a biosurfactant based on lactobacilli that demonstrated the ability to inhibit the development of *Acinetobacter baumannii*, *Escherichia coli,* and *Staphylococcus aureus* biofilms and induce their dispersion. The antibiofilm capacity of the biosurfactant has been reported at concentrations between 25 and 50 mg/mL. Several mechanisms can explain macromolecules' ability to prevent biofilm development. However, as illustrated in Figure 4.2b, it is well established that the difference in surface charges between the biofilm matrix and the exopolysaccharide can be enough to destabilize the matrix and alter the barriers that protect the cells from permeabilization by external agents [142]. According to Singh et al. (2021)[140], the antibiofilm capacity of EPS obtained from bacteria can be explained by the toxic attributes developed by the microbial community as a defense mechanism against external attacks.

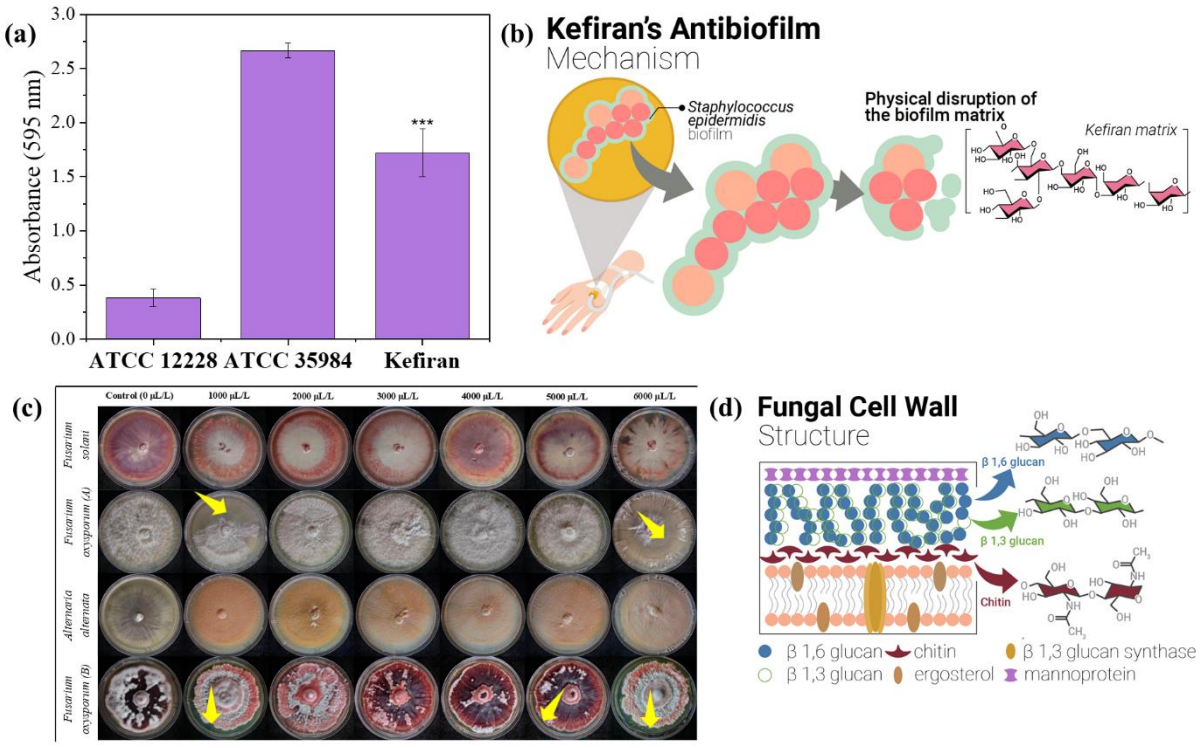

FIGURE 4.2 - (a) Amount of biofilm of *S. epidermidis* ATCC 35984 after treatment with kefiran polymer at 512 mg/L (*** p-value < 0.001), (b) kefiran's

antibiofilm mechanism proposed, (c) Antifungal effect tests using agar plates with *Fusarium solani, F. oxysporum (A), Alternaria alternata, F. oxysporum (B)* with different concentrations of kefiran, and (d) fungal cell wall structure.

The antifungal activity of kefiran was tested using six different concentrations of the polymer (13-78 mg/L), and the response was assessed by the inhibition of mycelial growth on the 5th day of incubation (Figure 4.2c). The fungi studied are of great industrial and agricultural interest, either because of the possibility of some of them affecting the food during its storage period, or because of the possibility of some fungi developing resistance to the pesticides currently used [143]. Figure 4.2c shows the results of the screening of kefiran's activity on the growth of different fungi on plates. Although there was no consistent action related to inhibiting fungal growth on the plate, significant changes were observed in the growth, color, shape, texture, and density of the mycelium, which may indicate the microorganism's susceptibility due to contact with the polymer. It is known that the morphology of fungi can be altered by the conditions to which the microorganism is exposed. At the same time, damage to the cell wall is the primary source of fungal inactivation and can be caused by genetic, chemical, or physical stimuli[144,145]. A possible mechanism involved in the changes in mycelium growth observed in the fungi tested may be related to the chemical reactions between the structure of kefiran and the composition of the membrane that protects the cell contents of the fungi, which is mainly composed of glucans containing mostly β-1,3 bonds and a small portion of β-1,6 and β-1,4 bonds [146] (Figure 4.2d). Other studies have shown the possibility of binding these glucans to polymers such as chitin, which also plays a vital role in protecting the cell contents. [146,147]. On the other hand, kefiran is an important glucogalactan that has enough bonding points to interact with these biopolymers present in the layer that protects the fungus, forming a polymeric membrane capable of preventing the transportation of nutrients[148]. In this context, the fact that kefiran does not significantly prevent the growth of fungi on the plate may be influenced by

various factors, such as molar mass, degree of substitution, concentration, and species of fungi[149].

4.1.3 Application of kefiran coating on strawberries

Increasing the shelf life of strawberries that have been covered and stored at room temperature is essential, mainly due to the climatic characteristics of this fruit, which cause it to lose its organoleptic properties and prevent it from being marketed. The strawberries were coated with kefiran by dip coating, as illustrated in Figure 4.3a. Characteristics such as freshness, color changes, and texture were evaluated for the groups of strawberries stored at 5 ºC ± 1 ºC (15 days) and 25 ºC ± 2 ºC (9 days). Storage was interrupted when the strawberries did not look fresh and showed wrinkles, brown spots, and a softened texture. As shown in Figure 4.3b-c, the kefiran-coated strawberries stored at 25ºC and 5ºC had no visual evidence of fungi or significant damage to the surface of the fruit until the 6th and 12th day, respectively. On the other hand, uncovered strawberries from both packaging groups began to show signs of rot, such as darkening and mold spots, from the 3rd (stored at 25ºC) and 9th day (stored at 5ºC).

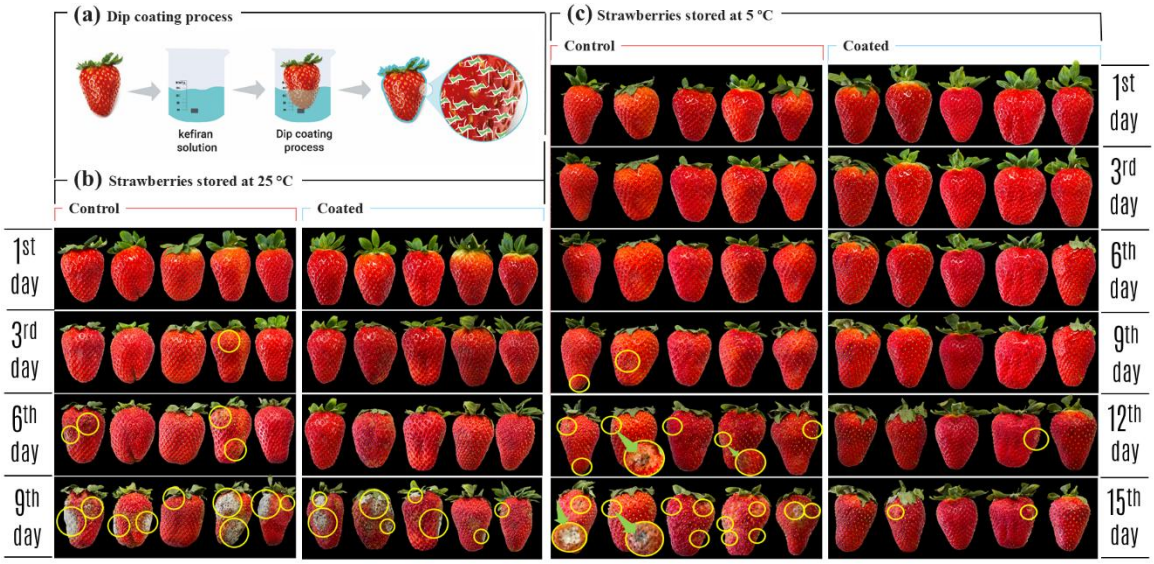

FIGURE 4.3 - (a) Illustration of the strawberry dip coating process, Changes in the visual appearance of strawberries stored at (b) 25 ºC and (c) 5 ºC (± 1 ºC)

during the period 9 and 15 days in uncoated (control) and coated with kefiran.

In general, fruits such as strawberries have a higher amount of moisture and have a longer shelf life at lower temperatures due to reduced respiration rates [150]. The increase in the rate of water loss from strawberries and damage to the surface encourages the presence of fungi and speeds up the process of fruit rot [151]. On the other hand, the group coated with kefiran showed degradation spots and the presence of fungi only on the 12th day, thus indicating the polymer's ability to increase the shelf life of strawberries. Similar results were shown in the study of Valenzuela et al. (2015)[152], which investigated the effect of coating fresh strawberries with chitosan, quinoa, sunflower oil, and a mixture of these on their shelf life. During the 15-day packaging period, the most intense rate of damage to the fruit was 50% (strawberries coated with the quinoa/chitosan/sunflower oil mixture), while the control group was completely damaged. Khodaei et al. (2021)[153] using edible coatings based on carboxymethylcellulose, pectin, Persian gum, and tragacanth gum helped reduce strawberries' deterioration rate by almost 70% compared to uncoated strawberries.

Percentage weight loss is a fundamental parameter for assessing the quality and shelf life of fruit, as well as providing essential data on respiration and transpiration processes [154]. As seen in Figure 4.4a, the weight of the strawberries studied at room temperature increased significantly over the test days ($p \leq 0.05$), reaching 47% in the case of the control group. On the other hand, the coated strawberries exhibited a 40% weight loss on the last day of the test, indicating that the biopolymer helps reduce the transfer of moisture from the fruit. Fruit weight loss is directly related to water loss resulting from the strawberry's transpiration and respiration process [155]. The high rate of respiration and the transfer of CO_2 are the main factors responsible for the high percentage of weight loss in strawberries. The lower weight loss registered for strawberries at 5ºC may be due to the difference in the vapor pressure gradient between the fruit house and the

atmosphere [156]. In addition, although not significant, the mass loss in the coated group was slightly more significant than in the control group. This behavior could be related to a lower efficiency of the polymer coating as a gas barrier for colder environments.

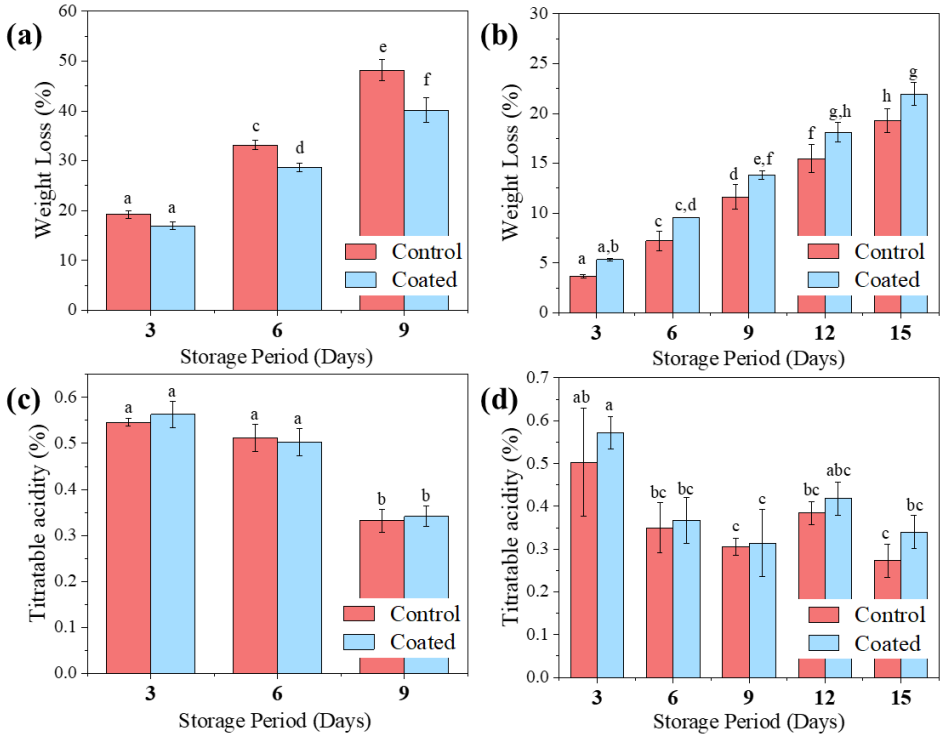

FIGURE 4.4 - Loss weight parameter of strawberries stored at (a) 25 ºC and (b) 5 ºC (± 1 ºC). Titrable acid of strawberry samples stored at (c) 25 ºC and (d) 5 ºC (± 1 ºC).

Figure 4.4c-d shows the titratable acidity (TA) percentages in the samples stored at different temperatures. As expected, TA levels decreased significantly with storage time ($p \leq 0.05$). However, the samples kept under refrigeration and coated with kefiran were slightly better able to retain the loss of TA than the control group. Similar results were reported by Maraei et al. (2017)[157]. The lower reduction in the TA values of the strawberries coated and stored at 5º C would be related to the decrease in the respiration rate of the fruits, which would prevent the deterioration of the organic acids, such as the irreversible oxidation of dehydroascorbic acid to dicetogulonic acid [158]. On the other hand, an increase in

the TA values of the group packed at 5 ºC for days 12 and 15 of storage could be explained by the activity of fungi in the strawberries, which would cause the production of acid metabolites [159]. The pH and the soluble solids (SS) content provide fundamental data on the quality of the fruit and the ripening and rotting process. Table 3 shows the fruit's pH values from both groups and the total soluble solids content expressed in °Brix (%). The analysis of variance shows that the storage period influences the pH of the strawberry juice ($p \leq 0.05$). The pH values increased with storage times, which is consistent with what was observed by Khodaei et al. (2021)[153]. Furthermore, it was shown that the rate of pH increases with the storage temperature of strawberries.

Table 3. Soluble solids content (°Brix) and pH for coated and uncoated strawberries stored at 25 ºC and 5 ºC.

Stored at (ºC)	**Storage time (day)**	**Parameters**			
		SS (º Brix)		**pH**	
		Control	Coated	Control	Coated
25	3	8.33 ± 0.57^{b}	10.00 ± 1.00^{ab}	$3.65 \pm 0.04^{\beta\lambda}$	$3.59 \pm 0.03^{\lambda}$
	6	9.53 ± 0.50^{ab}	10.00 ± 1.00^{ab}	$3.77 \pm 0.07^{\alpha\beta\lambda}$	$3.82 \pm 0.06^{\alpha\beta\lambda}$
	9	10.50 ± 0.50^{a}	11.33 ± 0.58^{a}	$3.97 \pm 0.03^{\alpha\beta}$	$3.84 \pm 0.18^{\alpha}$
5	3	8.50 ± 0.50^{AB}	7.50 ± 0.50^{B}	$3.67 \pm 0.18^{\ddagger\S}$	$3.47 \pm 0.02^{¥}$
	6	9.00 ± 1.0^{AB}	9.37 ± 0.64^{AB}	$3.67 \pm 0.04^{\ddagger\S}$	$3.72 \pm 0.02^{\ddagger\S}$
	9	8.67 ± 1.15^{AB}	8.73 ± 0.64^{AB}	$3.74 \pm 0.02^{\dagger\ddagger\S}$	$3.79 \pm 0.04^{\dagger\ddagger\S}$
	12	9.67 ± 0.58^{A}	8.83 ± 0.76^{AB}	$3.80 \pm 0.06^{\dagger\ddagger\S}$	$3.94 \pm 0.15^{\dagger\ddagger}$
	15	8.33 ± 0.59^{AB}	9.93 ± 0.12^{A}	$3.82 \pm 0.01^{\dagger\ddagger\S}$	$3.95 \pm 0.01^{\dagger}$

Values represent mean ± standard deviation, and statistical analysis was carried out by ANOVA plus Tukay's test. Statistical significance ($p < 0.05$) was indicated with different Tukay tests carried out between coated and control groups for each

parameter (pH or ºBrix). Equal letters or symbols indicate no significant difference between the groups (Tukey's test, $p < 0.05$).

According to Jokari et al. (2023)[158], the changes in pH and total soluble solids in fruit would be related to the breakdown of carbohydrates, pectin, and glycosaccharides, and the hydrolysis of proteins during respiration. An edible coating on fruit generally reduces the respiration rate and slows the degradation of organic acids and sugars, thus preventing pH changes. However, other articles have shown that there is no difference between the pH of fruit with and without coating [160]. As can be seen in Table 3, the rate of pH increase was lower for strawberries compared with kefiran than the respective control samples. Table 3 also shows the SS content values of the fruit packed at 25 and 5 ºC. The SS content increased with the storage time and temperature, which indicates that the fruit was sweeter with these variables [150]. This behavior is related to weight loss due to fruit dehydration and respiration and the consequent increase in juice concentration [150,160].

4.2 Synthesis of ZnO NPs, characterization, and antimicrobial studies

4.2.1 Characterizations associated with the antibacterial properties of NPs

To comprehend the antibacterial activity of ZnO nanostructures, it is imperative to initiate the analysis with a comprehensive characterization of these structures. To confirm the ZnO structure, Figure 4.5 shows the XRD patterns of the samples produced using NaOH (Figure 4.5a) or NH_4OH (Figure 4.5b) in synthesis times of 15 and 30 min, applying nitrate or zinc acetate as a metallic precursor. Only peaks related to the wurtzite ZnO structure are observed (ICDD

crystal card no. 36-1451, space group P63mc), indicating, within the limit of detection of the technique, the absence of secondary phases [161].

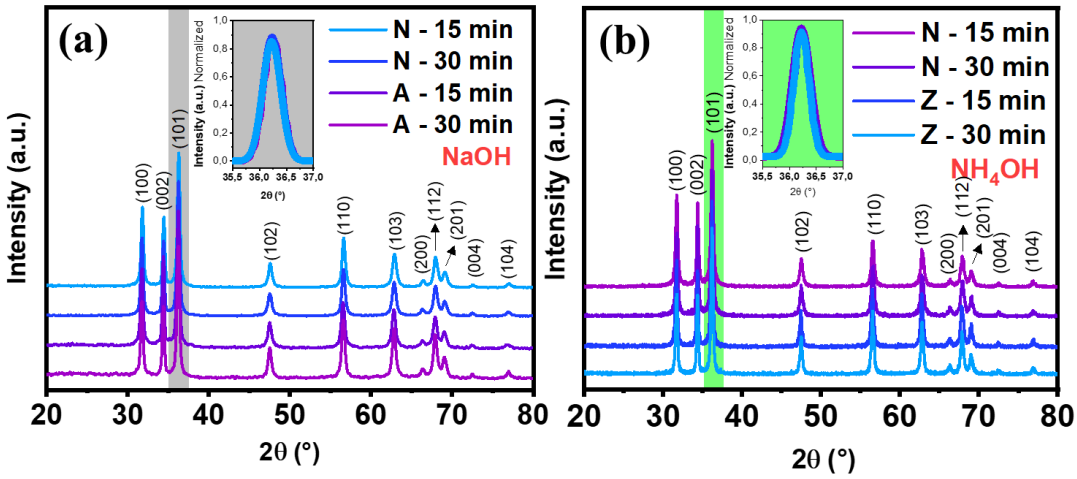

FIGURE 4.5 - XRD patterns of samples obtained using (a) NaOH and (b) NH_4OH. Reprinted with permission from Marques et al. (2024)[80], Copyright 2024, Elsevier.

From the kinetic metabolism curves of each bacterium analyzed at 512 mg/mL ZnO-NPs, presented in the Appendix (Figures 5.1-5.8), it was possible to determine whether antibacterial activity was present. The screening results demonstrated that the ZnO NPs exhibited antibacterial activity against Gram-positive bacteria, primarily against *S. epidermidis, S. aureus* (ATCC 25923), and *E. faecium*. The MICs of imipenem for the Gram-negative bacteria *K. pneumoniae*, *E. coli*, *A. baumannii,* and *P. aeruginosa* were 0.25, 0.25, 8, and 4 mg/L, respectively. The metabolism kinetics curves of the bacterial strains tested against several ZnO NPs concentrations were obtained from the OmniLog over 24 h and used to determine the MIC (Table 4). To ensure that the ZnO NPS synthesized in this study are composed of the pure wurtzite phase, the Rietveld refinement was applied, and the fits obtained were satisfactory (Figure 5.9 - Appendix).

Table 4. Minimal inhibitory concentration of ZnO NPs and daptomycin against gram-positive bacteria.

Bacterial strains	MIC (mg/L)					
	ZnO 1	ZnO 2	ZnO 3	ZnO 4	ZnO 7	Dap
S. epidermidis ATCC 35984	512	512	256	256	512	< 0.125
S. aureus ATCC 25923	>512	512	512	256	512	0.5
S. aureus ATCC 8095	>512	>512	512	512	>512	1
E. faecium ATCC 700221	512	512	512	>512	512	1

Dap – Daptomycin

Through refinement, it was also possible to extract data on the structural parameters (*a,b*, and c), density and cell volume of the ZnO phases (Table 5) based on a CIF file obtained from the Inorganic Crystal Structure Database. (ICSD) nº 26170.

Table 5. Rietveld refinement parameters and ZnO unit-cells.

Sample	a=b (Å)	c (Å)	c/a (Å)	Volume (Å^3)	Density	x^2	Crystallite size (nm)
ZnO-1	3.2490 (5)	5.2073 (5)	1.6027	47.605 (3)	5.683 (3)	2.15	18.43 ± 3.22
ZnO-2	3.2499 (5)	5.2084 (5)	1.6026	47.644 (3)	5.723 (3)	2.23	18.50 ± 3.40
ZnO-3	3.2499 (5)	5.2088 (5)	1.6027	47.646 (3)	5.706 (3)	2.06	19.33 ± 3.23
ZnO-4	3.2499 (5)	5.2087 (5)	1.6027	47.645 (3)	5.708 (3)	2.00	18.51 ± 3.41
ZnO-5	3.2534 (5)	5.2134 (5)	1.6027	47.792 (3)	5.586 (3)	1.34	18.83 ± 3.40
ZnO-6	3.2491 (5)	5.2074 (5)	1.6027	47.608 (3)	5.708 (3)	2.05	18.66 ± 3.02

ZnO-7	3.2499 (5)	5.2087 (5)	1.6027	47.644 (3)	5.700 (3)	2.06	21.65 ± 2.77
ZnO-8	3.2510 (5)	5.2105 (5)	1.6027	47.695 (3)	5.675 (3)	2.04	22.24 ± 4.19

Based on the calculated values, it is evident that the change in the metallic precursor does not significantly impact the values of the two network parameters, *a* and *c*. This similarity corroborates the heights of the two diffraction peaks corresponding to the plane (101), which also did not present differences in both groups of samples (insert Figure 4.6a-b). This result agrees with Gatou et al. (2022)[162], which investigated the effect of zinc acetate, nitrate, chloride, or sulfate on the preparation of ZnO-NPs. The degree of distortion of the unit cell (R) was also calculated from values of a and c substituted in Equation 13, in which values of R = 1 are attributed to a distortion-free unit cell [163].

$$R = \frac{\left(2a\sqrt{\frac{2}{3}}\right)}{c} \quad (13)$$

The *R* values presented in Table 6 confirm that the synthesis methods applied in this study efficiently produce ZnO with high crystallinity and without distortion in the unit cells, regardless of the variable used (Table 6). Given the similarity in the structural characterization results of the ZnO samples, the inhibitory selectivity of ZnO NPs against gram-positive bacteria can be attributed to surface interactions. This is because there are different interactions at the solid-liquid interface (nanoparticles-test medium) and the solid-liquid contact zone with biological groups (bacteria). These interactions depend on the polarity of the crystalline facets of the ZnO NPs and the characteristics of the cell membranes of the studied bacteria [164].

Table 6. Comparison between the positions and relative intensities (normalized) of the diffraction peaks corresponding to the planes of 100, 002, and 101 the ZnO

NPs.

Sample	Peak position[a] (2q)			Normalized Intensity (a.u)			R
	100	002	101	100	002	101	
ZnO -1	31.790	34.432	36.274	0.6259	0.4555	1	1.0189
ZnO -2	31.800	34.443	36.283	0.6389	0.4485	1	1.0189
ZnO -3	31.778	34.417	36.259	0.6569	0.4541	1	1.0189
ZnO -4	31.780	34.420	36.262	0.6456	0.4538	1	1.0189
ZnO -5	31.687	34.331	36.165	0.5992	0.4861	1	1.0191
ZnO -6	31.788	34.429	36.272	0.6541	0.4557	1	1.0189
ZnO -7	31.778	34.418	36.259	0.6545	0.4527	1	1.0189
ZnO -8	31.768	34.407	36.249	0.6545	0.4546	1	1.0189

[a] Positions of diffraction peaks and relative intensities (normalized) obtained from the Rietveld refinement produced in the GSAS 2 software.

The plane (101) corresponding to the facet of semi-polar nature showed the highest peak intensity in the XRD analyses (Figure 4.5). This plane is characterized by presenting an angle of ~ 45º about the eixo-*c* (axial) in the 3D ZnO structures contributing to the formation of pointed shapes in the axial or oval direction when combined with axial growth in the (100) plane[165]. The morphological characteristics of nanomaterials were evaluated from the type of base solution (NaOH or NH_4OH), Zn^{2+} [Zn $(NO_3)_2$ or Zn $(CH_3COO)_2$] precursor, and reaction time (15 or 30 min). In NaOH solution, Figure 4.6a shows that using the $Zn(NO_3)_2$ precursor and 15 min synthesis time, spherical particles (Insert-Fig. 4.6a) with an average diameter of 44.17 ± 17.13 nm are obtained as agglomerates. Increasing the synthesis time up to 30 min, particles increase in 30% their average diameter (57.59 nm ± 17.00 nm) with preferential growth in the radial direction

(100), (101), and moderate in the axial direction (002) until obtaining the oval form [166].

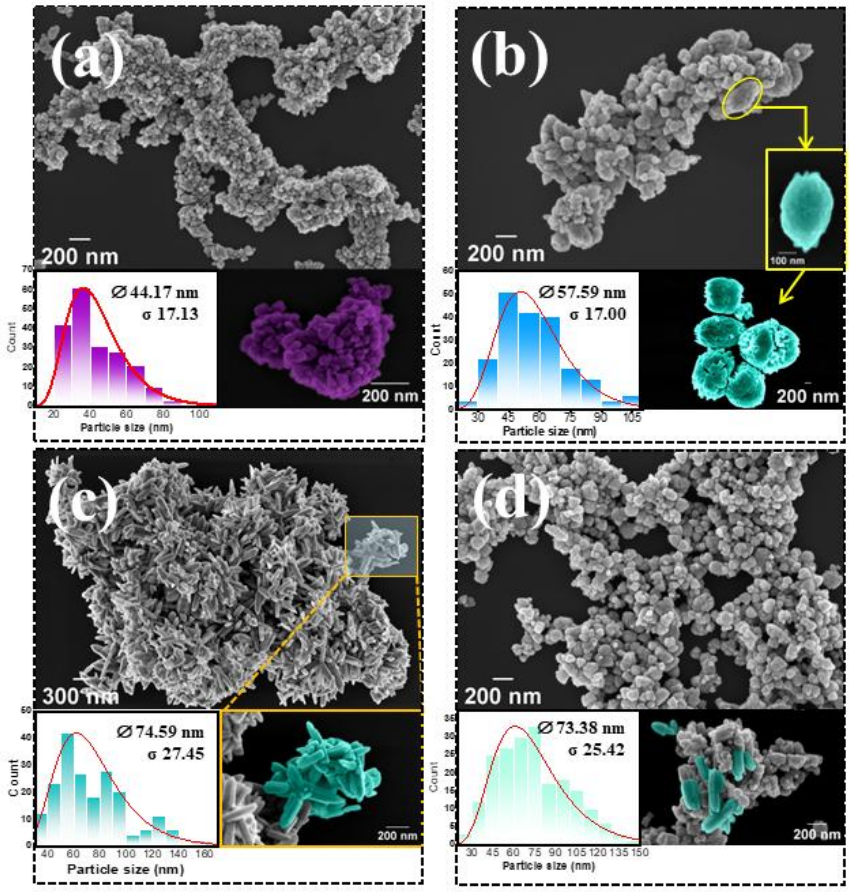

FIGURE 4.6 - SEM micrographs of (a) ZnO-1, (b) ZnO-2, (c) ZnO-3, and (d) ZnO-4 prepared in an alkaline medium using NaOH. Reprinted with permission from Marques et al. (2024) [80], Copyright 2024, Elsevier.

Still in NaOH solution, when applying $Zn(CH_3COO)_2$ as a precursor of Zn^{2+}, nanorods with an average diameter of 74.59 ± 27.45 nm and face (002) with reduced diameter in the radial direction are produced in 15 min of synthesis (Figure 4.6c). Increasing time to 30 min, the amount of nanorods decreases, and a mixture of spherical particles and rods is observed, possibly due to the dissolution of the rods and re-precipitation in an oval shape (Figure 4.6d).To understand the influence of the metallic precursor on the morphology of the

particles, the reactions from 14 to 16 describe the formation of ZnO in a basic medium [167].

$$Zn^{2+}_{(aq)} + 2OH^{-}_{(aq)} \rightarrow Zn(OH)_{2(s)} \quad (14)$$

$$Zn(OH)_{2(s)} + (x-2)OH^{-}_{(aq)} \rightarrow Zn(OH)^{2-x}_{x} \quad (15)$$

$$Zn(OH)^{2-x}_{x} \rightarrow ZnO + H_2O + (x-2)OH^{-} \quad (16)$$

As seen in Equations 14 to 16, the anions NO_3^- and CH_3COO^- do not participate directly in the precipitation of Zn^{2+} in the form of ZnO. However, when crystallization nuclei are formed, the polar facets (002) alternate between negative (O^{2-}) and positive (Zn^{2+}) due to the O-Zn-O bonds increasing in the axial direction [168]. Thus, the non-polar facets (101), (002) interact with the NO_3^- or CH_3COO^- anions when the O-polar characteristics assume the axial growth plane[169]. Considering that the acetate ion has a less polar character than NO_3^-, this is preferentially deposited on the non-polar facet of ZnO. On the other hand, $Zn(OH)_4^{2-}$ and NO_3^- compete for deposition on the Zn-polar facet. When the O-polar facet takes over the growth face, $Zn(OH)_4^{2-}$ can deposit on the non-polar face in competition with the acetate ion. This behavior results in radial and ax; however, in the presence of an acetate ion, axial growth is preferable more significantly greater interaction than the acetate ion presents with the non-polar face [167]. In addition, $Zn^{2+}_{(aq)}$ or $Zn(OH)_2$, formed in NaOH solution, interact with the non-polar face (101), (002), increasing the diameter in the radial direction, which produces spherical-shaped particles. As the reaction time increases, the adsorption-desorption equilibrium exposes all facets, resulting in more significant interaction in these positions. Consequently, moderate ZnO precipitation in the axial direction is achieved within 30 min to obtain a surface that tends to smaller diameters (tape) [170].

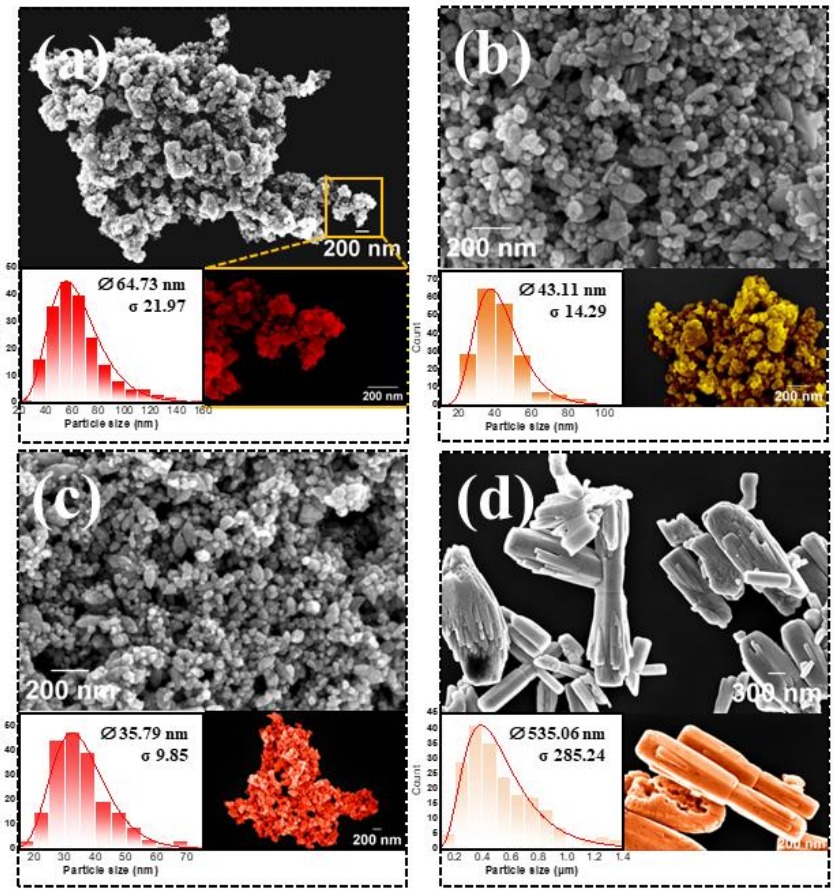

FIGURE 4.7 - SEM micrographs of (a) ZnO-5, (b) ZnO-6, (c) ZnO-7, and (d) ZnO-8 prepared in an alkaline medium using NH_4OH. Reprinted with permission from Marques et al. (2024) [80], Copyright 2024, Elsevier.

Unlike the NaOH solution, using NH_4OH can form other complexes with Zn^{2+}. Thus, the morphological characteristics of nanomaterials when using an NH_4OH solution in the presence of precursors $Zn(NO_3)_2$ or $Zn(CH_3COO)_2$ after 15 or 30 min of reaction are shown in Figure 4.7. In addition to the $[Zn(OH)_4]^{2-}$ complex and $Zn(OH)_2$ formed in the presence of hydroxyls, the dissolved ammonia when the base used is NH_4OH produces the complex $[Zn(NH_3)_4]^{2+}$ (Equation 17) [97].

$$Zn^{2+}_{(aq)} + 4NH_{3(aq)} \leftrightarrows [Zn(NH_3)_4]^{2+} \quad (17)$$

Then, the $[Zn(NH_3)_4]^{2+}$ complex reacts with excess hydroxyls, releasing ammonia to convert to the $[Zn(OH)_4]^{2-}$ complex, as shown in Equation 18.

$$[Zn(NH_3)_4]^{2+}{}_{(aq)} + 4OH^-{}_{(aq)} \leftrightarrows [Zn(OH)_4]^{2-}{}_{(aq)} + 4NH_{3(aq)} \quad (18)$$

In the last step, the reaction proceeds as described in Equation 19, and ZnO is finally formed [97].

$$Zn(OH)_2(s) + [Zn(OH)_4]^{2-}(aq) \rightarrow \Delta\, 2ZnO(s) + 2H_2O_{(l)} + 2OH^-(aq) \quad (19)$$

The chemical composition of non-reacting Zn^{2+} species is more complex in the presence of NH_4OH compared to NaOH. In NH_4OH solution, Zn^{2+} appears as $Zn^{2+}{}_{(aq)}$, $Zn(OH)_{2(s)}$, $[Zn(OH)_4]^{2-}{}_{(aq)}$ and $[Zn(NH_3)_4]^{2+}{}_{(aq)}$. As a crystallization nucleus is formed, electrostatic interaction can occur in all facets due to the different polarities of the Zn^{2+} intermediates. When the $Zn(NO_3)_2$ precursor is used, the NO_3^- ion interacts with the polar-Zn facet and inhibits axial growth. However, the interaction of the polar-Zn facet with $[Zn(OH)_4]^{2-}$ can also occur moderately since the mobility of $[Zn(OH)_4]^{2-}$ is lower compared to NO_3^- [171]. Furthermore, positively charged Zn^{2+} species can interact with the O-polar face and grow in the axial direction. However, the adsorption energy of the O-polar facet is unfavorable, and the smaller number of interaction sites limits growth in this direction [172]. Thus, the interactions of the O-polar facet can be enhanced in the presence of $[Zn(NH_3)_4]^{2+}$, distributing axial growth with the Zn-polar facet, forming rod structures. At the same time, $Zn(OH)_2$ can precipitate in the non-polar facet and increase in diameter in the radial direction. In general, the complex composition of the system allows growth in all directions, with a greater tendency towards the radial direction due to the saturation of the Zn-polar face by NO_3^- ions at any reaction time. In the presence of the zinc acetate precursor, the non-polar facets are restricted by the more efficient adsorption of the acetate ions, resulting in preferential growth in the axial direction. This tendency increases with reaction time, which is evidenced by the more significant number of rods observed in Figure 4.7d.

FTIR analyses showed that for the ZnO-3, ZnO-4, and ZnO-8 samples, peaks centered at 1405 and 1550 cm^{-1}, especially, were more intense (Figure 4.8).

These peaks are attributed to the presence of acetate ions of the Zn-precursor [173], which were adsorbed with greater efficiency on the non-polar facets, contributing to the axial growth and formation of rods in these samples. Therefore, the ZnO-5 sample mostly showed the presence of nanospheres, and, in some regions of the image, it was possible to observe the presence of particles with the shape of a straight hexagonal prism with a central cavity (insert of Figure 4.8d). Particle size was also affected by the microwave oven treatment time when the histograms of Figure 4.7a-b are compared for samples ZnO-5 and ZnO-6. Nanospheres formed in sample ZnO-5 have an average length of 64.73 nm (± 21.97 nm), while in piece ZnO-6 was 43.11 (± 14.29). The EDX of ZnO NPs reveals the presence of Zn and O, confirming pure ZnO nanoparticle synthesis (Figure 4.9).

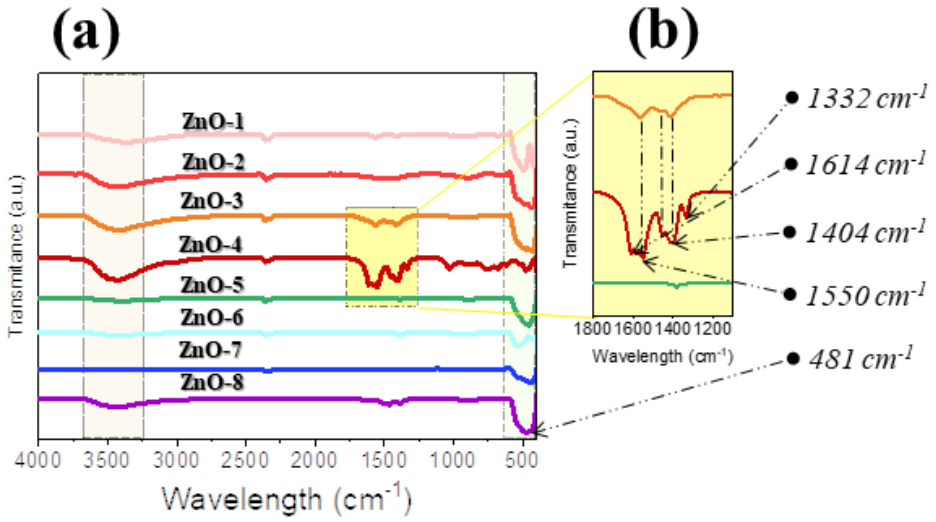

FIGURE 4.8 - (a) FTIR spectra of ZnO NPs samples with different morphologies and (b) magnification of the region 1800 - 1100 cm-1. Reprinted with permission from Marques et al. (2024) [80], Copyright 2024, Elsevier.

182

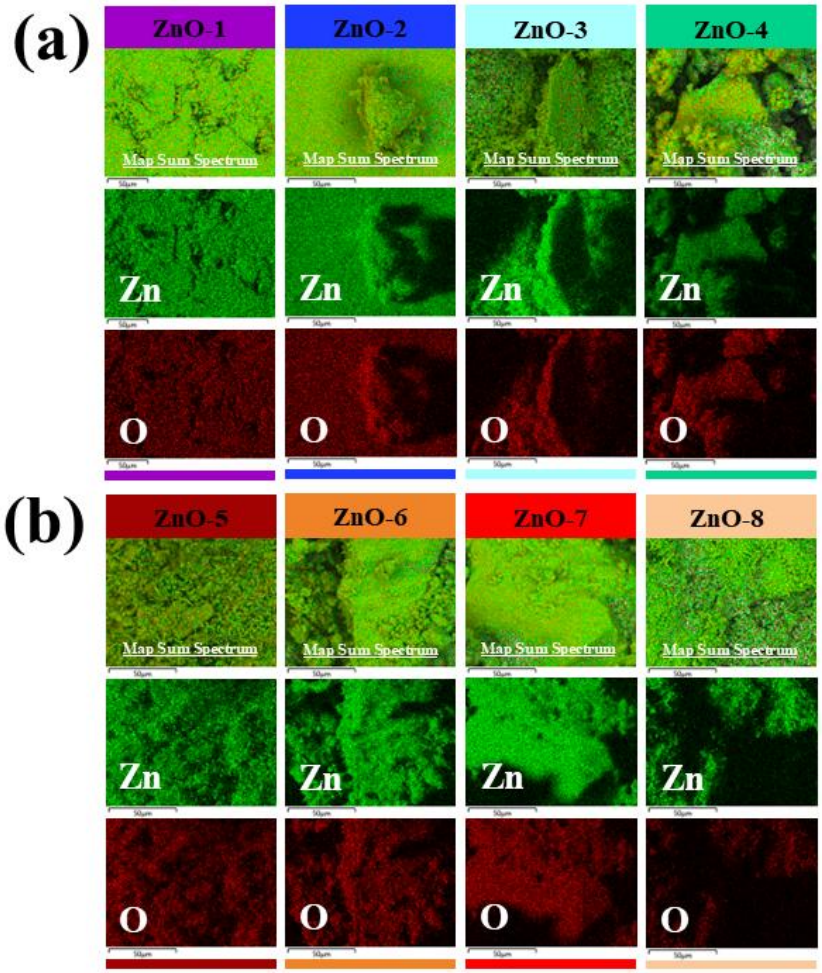

FIGURE 4.9 - EDS spectrum of the samples produced using (a) NaOH and (b) NH4OH. Reprinted with permission from Marques et al. (2024) [80], Copyright 2024, Elsevier.

Crystallite size is a structural parameter associated with preferential growth in NPs, and their size can be significantly dependent on the synthesis conditions [174]. Therefore, we chose it as a response to analyze the effect of metallic precursor, base type, and MW irradiation time on ZnO synthesis. Thus, the percentage of each effect on the crystallite size and your cumulative sum have been calculated to evaluate the strategies that have a significant effect (Figure 4.10a).

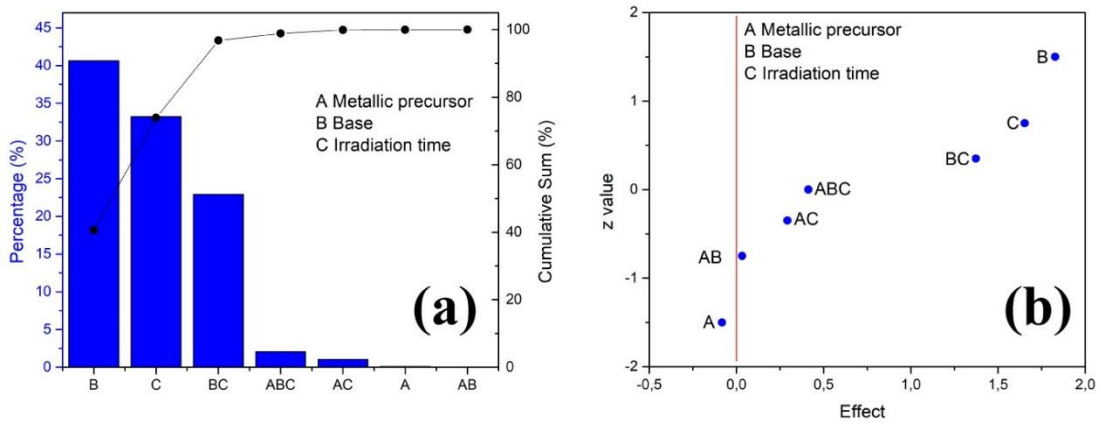

FIGURE 4.10 - (a) Percentage of each effect on the crystallite size (μm) and cumulative sum and (b) the probability graph of effects. Reprinted with permission from Marques et al. (2024) [80], Copyright 2024, Elsevier.

The base (effect B) and the MW irradiation time (effect C) were the most relevant effects on the crystallite size. The metallic precursor (effect A) contributed less than 1% to the response and the remaining secondary and tertiary effects. Figure 4.10b illustrates the magnitude, direction, and significance of the effects. The negligible effects conform to a normal distribution with a mean of zero on the x-axis, as indicated by the fit line (red). The significant effects exhibit nonzero means and are more distant from the red straight line. The positive estimated effect B revealed that the crystallite size increased with increasing B at the studied levels. This is because, in the presence of NH_4OH (upper B level), the different complex structures of Zn^{2+} interact with more ZnO facets, promoting an increase in crystallite size. Variable C has also had a significant effect on the system, increasing the crystallite size due to the longer interaction time of the ions on the ZnO facets. The negative estimated effect A reveals that the change in metallic precursor type is related to the decrease in crystallite size. The mechanisms of ZnO formation associated with the presence of A, B, and C are detailed below.

The preferential growth associated with the facets [(100), (002), and (101)] proved to be an essential factor in obtaining different morphologies. As their polarities improve interaction with the bacterial cell wall, the intensity of the

3 principal peaks [(100), (002), and (101)] was normalized by the highest intensity peak (101), and the ratio I(100)/I(002) was calculated [175]. All the calculated values of $I_{(100)}/I_{(002)} > 1$ confirm that the non-polar (100) and semi-polar (101) facets compose the majority of the ZnO nanostructures.

The selective toxicity of ZnO-NPs against gram-positive bacteria is explained by the more significant electrostatic interaction that the non-polar facets (100, 101) show with the exposed peptidoglycan layer in this group of bacteria[176,177].

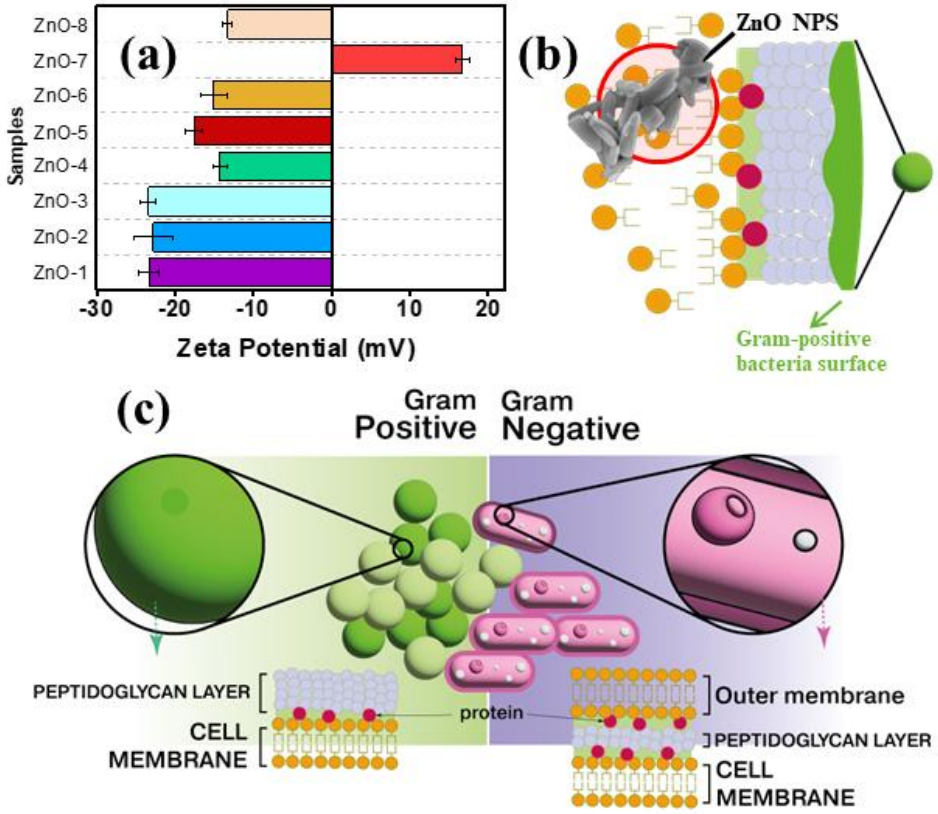

FIGURE 4.11 - (a) zeta potential values (b) illustration of the mechanism of damage to the surface of gram-positive bacteria (membrane disruption and cytoplasmic leakage) caused by electrostatic interaction between NPs and the microorganism, and (c) characteristic structures of the bacterial membrane. Reprinted with permission from Marques et al. (2024)[80] Copyright 2024, Elsevier.

Pranjali et al. (2019) [178] suggested that ZnO-NPs can interact and adsorb biological fluids, such as proteins, lipids, and metabolites, which could hinder the

stability and reduce the antibacterial action of this [179]. Furthermore, zeta potential analyses (Figure 4.11a) showed negative surface charges due to hydroxyl or acetate on the surface of ZnO-NPs. The acetate and hydroxyl groups on the ZnO-NPs surface can easily link with the amine or hydroxyl groups of peptidoglycans to increase bacteria exposure to ZnO-NPs [180]. In this way, when the electrostatic interaction (ZnO-NPs/Gram-positive bacteria) occurs, in addition to the damage caused to the peptidoglycan layer, the Zn^{2+} ions dissolved in the solution or present in the polar facet (001) more easily reach the cell cytoplasm [181]. Only ZnO-7 showed a positive surface charge, which can be attributed to the more significant amount of Zn^{2+} ions on the surface of this material (Figure 4.11b).

As Zn^{2+} ions are also highly toxic to bacteria, their bactericidal activity is also noted. The inactivity observed for Gram-negative bacteria is due to the thinner and more complex cell wall, composed of an outer layer of lipopolysaccharides that can act as a protective shield against damage to the surface and, consequently, override the inactivation mechanisms [180,182–186]. Figure 4.11c shows the characteristic structures of the bacterial membrane. Other results of the antibacterial activity of ZnO-NPs are reported in the literature [187,188]. Considering the properties of ZnO NPs discussed above, the samples that exhibited antibacterial activity, namely ZnO-1, ZnO-2, ZnO-3, ZnO-4, and ZnO-7, were chosen for determining the MIC followed by the PCA analysis.

4.2.2 Minimum Inhibitory Concentration and PCA Analysis

The objective was to apply the MIC values in conjunction with PCA to evaluate the metabolic response of bacterial strains after treatment with ZnO antibacterial materials. By transforming MIC values into a reduced set of uncorrelated components, PCA reveals hidden relationships and trends that might be obscured in the original high-dimensional data. The plot of the PCAs discrimination functions with the MIC values (Figure 4.12) revealed a degree of

segregation between the classes, meaning that the methodology allowed for detecting variables that differentiate antimicrobial agent groups.

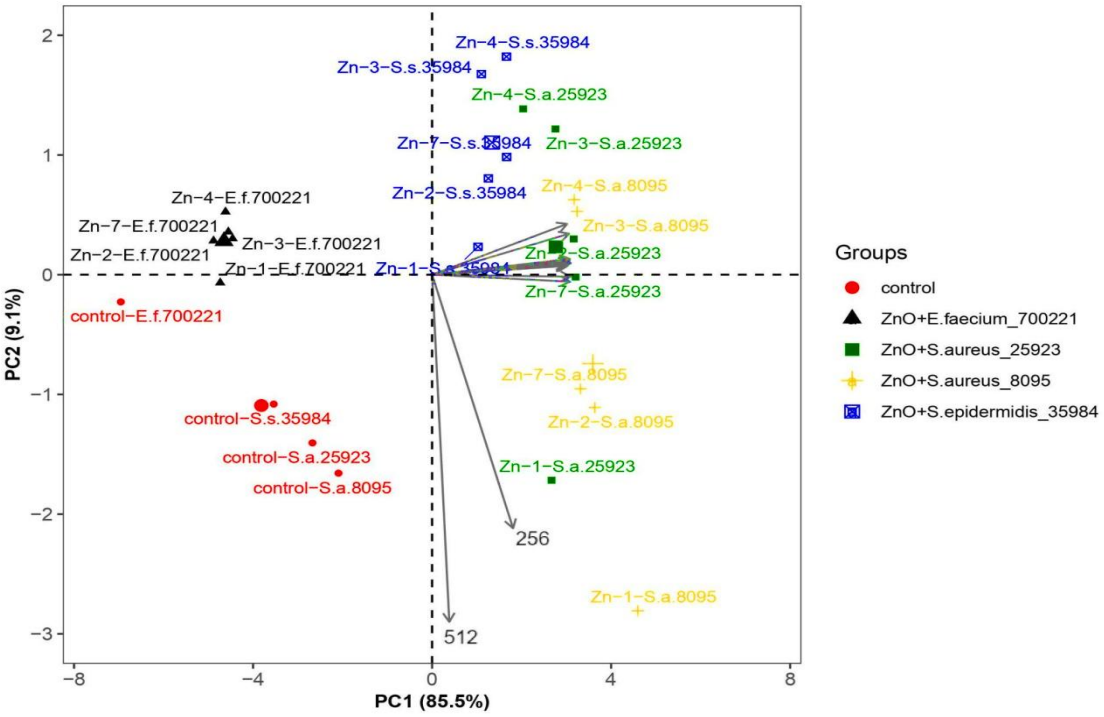

FIGURE 4.12 - PCA results: Projections of scores and loadings for the first two principal components. Reprinted with permission from Marques et al. (2024) [80] Copyright 2024, Elsevier.

PCA eigenvalues indicate that the first two axes explain 94.6% of the total variability (PC1 explains 85.5% and PC2 9.1%). Therefore, these two PCs were selected for further analysis and visualization. The contribution of each variable, their relationships, and the resulting principal components were illustrated in Figure 4.12. The PC1 exhibited a strong positive correlation with the ≤128 mg/mL concentrations, i.e., inhibition is not overly evidenced compared to controls. However, the antibacterial activity at 256 and 512 mg/mL concentrations showed a significant negative correlation with PC2, indicating that the bactericidal action is inhibited at these concentrations. A few observations were made from the score plot for PC1 to PC2 for all treatments (Figure 4.12), where the samples of bacterial strain pure and those treated with ZnO materials (ZnO-1,

ZnO-2, ZnO-3, ZnO-4, and ZnO-7) are grouped. It is essential to notice that the PCAs models could distinguish well the samples of all non-treated bacterial strains, as a bacterial control group, from those exposed to one of the antibacterial agents. In one quadrant, the control samples are positioned as a distinct cluster, markedly distant from other classes, displaying exclusively negative score values for both PCs. The bacterial strains (*S. aureus* ATCC 25923 and 8095, and *S. epidermidis* ATCC 35984) treated with ZnO materials in the upper right quadrant, e.g., ZnO-3 and ZnO-4, were compelling and inhibited bacterial growth. In contrast, materials on the low right quadrant, e.g., ZnO-1, ZnO-2, ZnO-3, and ZnO-7, were less effective. The *E. faecium* ATCC 700221 samples are mainly placed in a cluster on the upper left quadrant of the plot. Similarly, *E. faecium* ATCC 700221 samples treated with ZnO materials such as ZnO-3 and ZnO-4 effectively inhibit bacterial growth—conversely, other tests like ZnO-1, ZnO-2, ZnO-3, and ZnO-7 are comparatively less effective.

This tendency could be associated with the mentioned nanoparticles' high antibacterial activity and structural differences. The different MIC values are due to the sensitivity by which other mechanisms can inactivate each type of Gram-positive bacteria. Our results showed that the possible tools are the direct interaction between material-bacteria in the non-polar facets, the presence of Zn^{2+} ions in the solution, and especially ROS. For the latter, the production of ROS by the ZnO-NPs is an essential mechanism for inhibited bacterial activity since these can be produced even without light [189,190]. The formation of ROS ($OH^{\bullet}$, H_2O_2, $O_2^{\bullet-}$ and $^{\bullet}O_2$) and the interaction of these species with DNA, proteins, and enzymes can lead to the deregulation of vital processes for the cellular maintenance of these microorganisms. Among the ROS species with the most significant potential to cause oxidative stress, the hydroxyl radical ($OH^{\bullet}$) can react with virtually all constituents present in bacteria. Its first targets are proteins, DNA, and lipids, which can form other secondary ROS from the interaction and reaction [191]. As the

formation of ROS is enhanced under light, photocatalytic studies have been carried out.

4.2.3 Unraveling the antimicrobial mechanism from the formation of ROS

From diffuse reflectance measurements, the bandgap energy (E_{gap}) of the ZnO samples was calculated using the Tauc equation (Figure 4.13) [192]. The E_{gap} values varied from 3.09 to 3.12 eV, and considering all the samples, an $E_{gap(mean)} = 3.11 \pm 0.01$ eV was obtained. The results reveal that the absorption of light energy does not show significant variation for the different samples and that the photocatalytic activity is expected for $\lambda < 401$ nm, corresponding to the region of transition of ultraviolet-visible absorption.

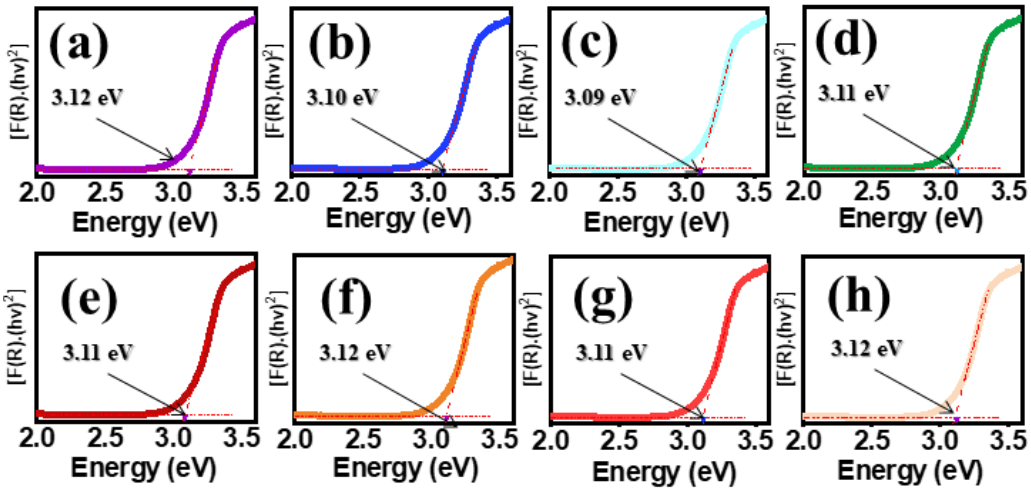

FIGURE 4.13 - Band gap estimation of (a) ZnO -1, (b) ZnO – 2, (c) ZnO -3, (d) ZnO – 4, (e) ZnO -5, (f) ZnO – 6, (g) ZnO -7, (h) ZnO – 8 samples using Tauc plot. Reprinted with permission from Marques et al. (2024)[80], Copyright 2024, Elsevier.

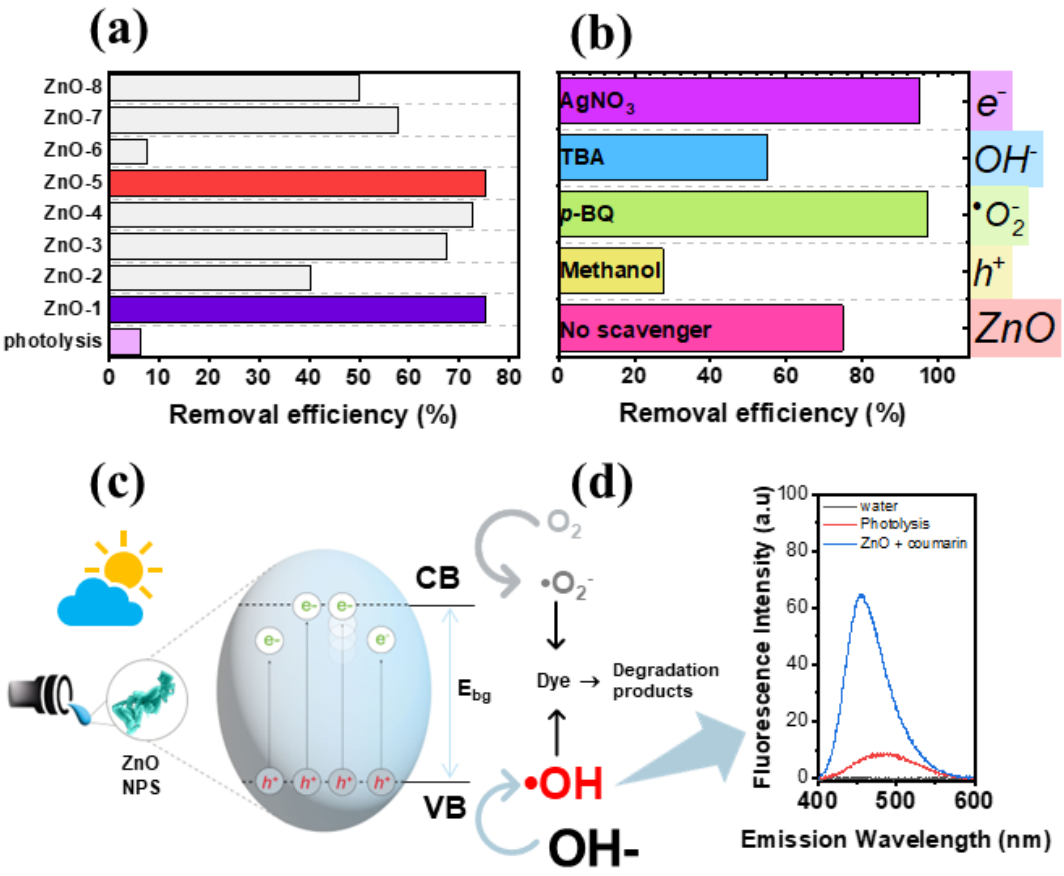

FIGURE 4.14 - (a) Efficiency of the MB photodegradation process using different ZnO NPs samples, (b) scavenger tests for determination of reactive oxygen species (ROS) using the ZnO – 5 sample, (c) proposed photodegradation mechanism and (d) fluorescence spectra of OH generation using coumarin (λ exc = 332 nm). Reprinted with permission from Marques et al. (2024) [80], Copyright 2024, Elsevier.

Therefore, the photocatalytic mechanism was studied in detail using ROS scavengers, with the reference sample being ZnO-5, which achieved the optimal removal in the MB photodegradation assays. The results shown in Figure 4.14b confirm a reduction in photocatalytic efficiency when MeOH and TBA are used as $^{\bullet}OH$ and h^+ scavengers, respectively. The contribution of h^+ and $^{\bullet}OH$ to the photochemistry mechanism directly correlates with each other and shows that the optimal photocatalytic response of materials occurs in the oxidation sites. However, removal efficiency was increased in the presence of $AgNO_3$ and p-BQ

compared to pure photocatalysts. These results show that the electrons photogenerated and available in the BC are easily transferred to the respective electron acceptors, maintaining the flow of formation of h^+ and consequent oxidation of water to produce the $^{\bullet}OH$. Thus, in the absence of electron acceptors, the formation of $O_2^{\bullet-}$ cannot be ruled out even if its activity is insignificant compared to the h^+ and $^{\bullet}OH$ in the degradation mechanism (Figure 4.14c). In summary, when ZnO is stimulated by light, the VB electrons are excited to BC. The photogenerated holes are active to oxidize water into hydroxyl radicals, which were verified in this study using the coumarin probe assay and shown in Figure 4.14d. In this test, when $^{\bullet}OH$ is formed, it reacts with coumarin and forms umbelliferone, which exhibits an emission peak centered at 453 nm when excited with $\lambda = 332nm$ [117].

In sequence, the photo-excited electrons for CB can reduce O_2 to $O_2^{\bullet-}$, and the series of reactions described in Equations 20 to 24, promote the efficient oxidation of the organic pollutant.

$$\text{ZnO-NPs} + hv \rightarrow h^+(VB) + e^-(CB) \quad (20)$$

$$h^+(VB) + H_2O \rightarrow {}^{\bullet}OH + H^+ \quad (21)$$

$$^{\bullet}OH + MB \rightarrow \text{byproducts} \quad (22)$$

$$e^-(CB) + O_2 \rightarrow O_2^{\bullet-} \quad (23)$$

$$O_2^{\bullet-} + MB \rightarrow \text{byproducts} \quad (24)$$

Zn^{2+} leaching after 60 min of photocatalysis was monitored by FAAS and reached values of 3.13 ± 0.01% (ZnO-1), 23.4 ± 0.11% (ZnO-2), 0.77 ± 0.01% (ZnO-3), 2.80 ± 0.00% (ZnO-4), 10.3 ± 0.09% (ZnO-5), 0.60 ± 0.01% (ZnO-6), 4.28 ± 0.01% (ZnO-7) and 1.33 ± 0.01% (Zn)-8). Except for the ZnO-2 and ZnO-5 samples, the leaching was insignificant, confirming that the Zn^{2+} was

crystallized in the form of ZnO with high efficiency. However, the highest leaching values observed for the ZnO-2 and ZnO-5 samples indicate the presence of Zn^{2+} ions adsorbed on the surface of the materials, which migrate easily into the solution. As the literature reports that Zn^{2+} ions are excellent bactericidal agents, in addition to the evidenced photocatalytic activity, the bactericidal activity of the materials can be obtained.

4.3 Compatibilization study of kefiran and CMC films

4.3.1 Optimization of the CMC-based film production process

The effect of the CMC concentration used to prepare the plates directly affects the film thickness, as shown in Figure 4.15a. The analysis of variance (ANOVA) indicated that, at the 95% confidence level, the average thicknesses were significantly different ($p < 0.05$). CMC is a cellulose derivative that possesses β-(1,4)[51]. The thickness of sample CMC-1/100 increased from ~43 μm to ~65 μm in CMC-1.3/100, corresponding to a ~40% increase. A more pronounced effect was observed for CMC-2/100, whose thickness reached ~120 μm, representing a 140% increase compared with the initial sample. The increase observed in the thickness of the film with higher CMC content can be attributed to the greater amount of solids present in the molding solution. As the CMC concentration increased from CMC-1/100 to CMC-1.3/100 and subsequently to CMC-2/100, the viscosity of the solution also increased, resulting in less spreading and shrinkage during solvent evaporation. In addition, the higher degree of chain entanglement at high polymer concentrations contributed to the formation of thicker and more compact films [51,54]. Additionally, the water contact angle (WCA) of the films was evaluated, as this parameter is crucial for determining their hydrophilic or hydrophobic character, which directly influences performance in food packaging applications [71]. Sample CMC-1.3/100 exhibited WCA values below 60° (Figure 4.15b), indicating its hydrophilic nature, as also

reported by Nazri et al. (2021) [193]. Moreover, samples CMC-1/100 and CMC-2/100 showed even lower WCA values compared with CMC-1.3/100; however, these values are still comparable to those reported for CMC-based films in which plant leaf polysaccharides were incorporated to reduce their hydrophilic characteristics[194]. It suggests a stronger polymer-polymer interaction when compared to polymer-water interaction. Typically, polysaccharides have lower WAC values due to polar functional groups, such as carbonyl (C=O) and hydroxyl groups, which tend to bind to water molecules [195]. Nevertheless, these values are similar to those reported by Michelin et al. (2020) [196], who produced pure CMC films with a WAC of 40.96°. In contrast, the lignin films showed slightly higher values, just above 50° (Table 7).

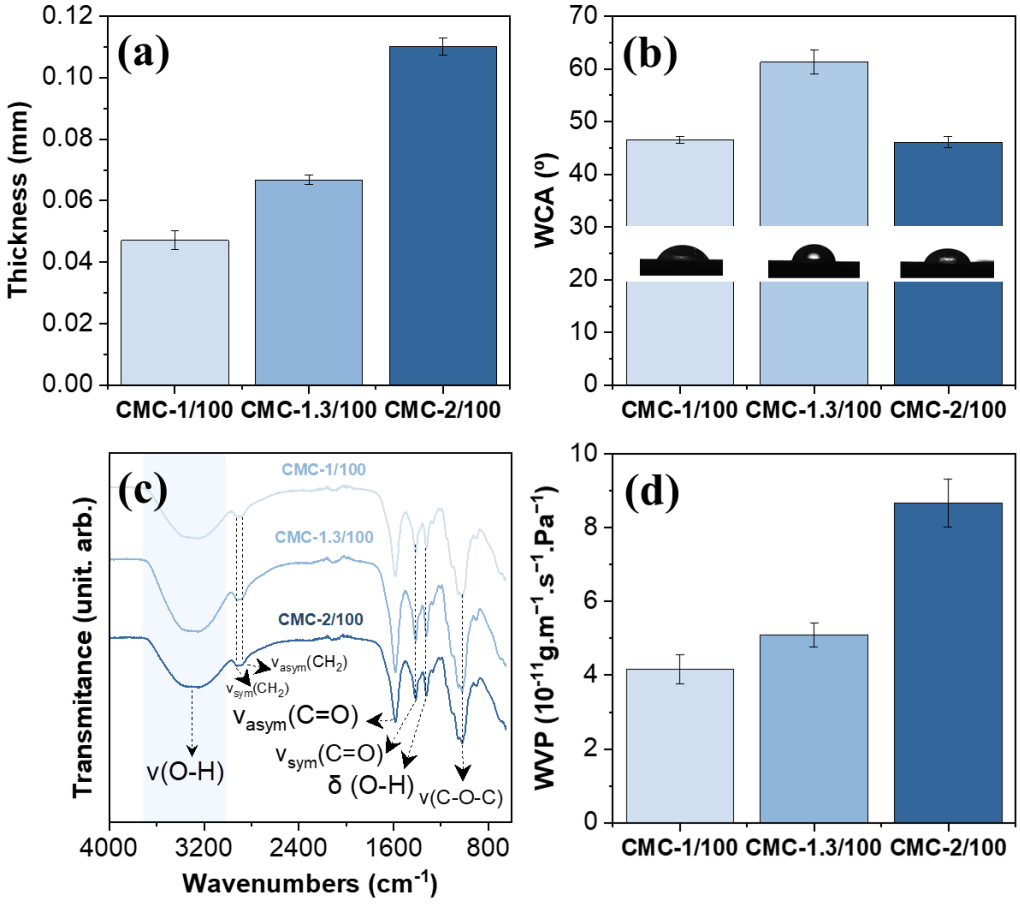

FIGURE 4.15 - (a) Thickness, (b) WCA, (c) FT-IR measurements and (d) WVP of films produced with different volumes and concentrations of CMC.

Figure 4.15c shows the FTIR spectra of films produced with different CMC formulations. The broad vibration band located at 3294 cm^{-1} refers to the stretching frequency of the hydroxyl group (-OH) present in the CMC structure [197,198]. The C-H bond stretching vibration is represented in the spectrum by the peak at 2924 cm^{-1}. The band at 1600 cm^{-1} is related to the bond vibrations of the carboxyl group attached to the cellulose structure [199]. The peaks at 1584 and 1411 cm^{-1} are representative of the symmetrical and asymmetrical vibrations of the carboxyl group (-COOH) and $-CH_2$ [197]. The bands at 1319 and 1020 cm^{-1} are attributed to the bending vibrations of O-H and ether groups, respectively. The band observed at 1054 cm^{-1} is characteristic of the C-O stretching of CMC chains and is considered the fingerprint of this polysaccharide [200].

Additionally, concerning the WAC behavior, the WVP data can also be evaluated regarding the chemical structure of the films[71]. Regarding the films' ability to prevent water vapor permeability (WVP), it can be observed in Figure 4.15d that the increase in CMC concentration contributes to reducing the films' resistance, thereby decreasing their water vapor barrier capacity. This behavior may be attributed to the increased free volume between the CMC chains, which facilitates moisture transfer [201,202]. The increase in the WVP value is the opposite of what is expected for films that can protect food against spoilage [194]. The increase in WVP values for the 2/100 sample can be attributed to the film thickness, as previously discussed [194]. Verma et al. (2024)[201] state that thicker films can absorb more water molecules than thinner films. This behavior changes only in sample B-32, which shows a reduction of ~6% compared to sample B-25.

When comparing the WVP values found in the literature with those of sample B-32 (Table 7), it can be observed that it exhibits a barrier capacity like that of other CMC films with comparable compositions, as well as films produced with the addition of other biopolymers, such as chitosan [203]. This is significant in

optimizing film production parameters, as it suggests that films with properties like those of blends can be produced.

Table 7. Comparison of water vapor permeability (WVP) and water contact angle (WCA) values of CMC-based films reported in the literature.

CMC solution composition (mCMC in g to 100 mL of water)	**WCA** (º)	**WVP** ($g.s^{-1}m^{-1}Pa^{-1}x10^{-10}$)	**Reference**
1*	┼	0.78	[204]
1.3	61.26	0.51	This work (1.3/100)
2**	┼	0.52	[203]
2***	40.96	3.61	[196]
2	┼	8.95	[194]
2	┼	~1.1	[202]
2	45.39	2.73	[205]
2	┼	0.92	[56]
6.75	34.00	┼	[193]

* It was addicted to glycerol based on CMC weight.
** It was addicted to 2g of chitosan.
*** CMC aqueous solution was prepared by dissolving 2% (w/w) CMC in an ethanolic solution (50%, v/v)
┼ Not informed

Figure 4.16 shows the SEM and AFM images of the films produced with different CMC concentrations. All the films generally had a smooth, uniform, and homogeneous surface. However, as indicated by the blue circles in samples 1/100 and 1.3/100, a few agglomerates were evident in various areas of the micrographs. The presence of these agglomerates may indicate incomplete solubilization of the polymer and may also negatively impact the mechanical and barrier properties of the film [206,207]. The cross-sectional images of the films (insert) demonstrate that the increase in CMC concentration and the volume used in the casting process both contribute to the increase in thickness, as previously

mentioned. The topographic images of the samples produced using an atomic force microscope help confirm that the presence of agglomerates observed in the SEM images does not occur in all samples (Insert Figure 4.16). In addition, the average roughness values (Ra) obtained from the AFM images increased with the CMC concentration in each system. This increase was approximately 11% in the CMC-1.3/100 sample and 58% in the CMC-2/100 sample, when compared with CMC-1/100 (Insert Fig. 4.16).

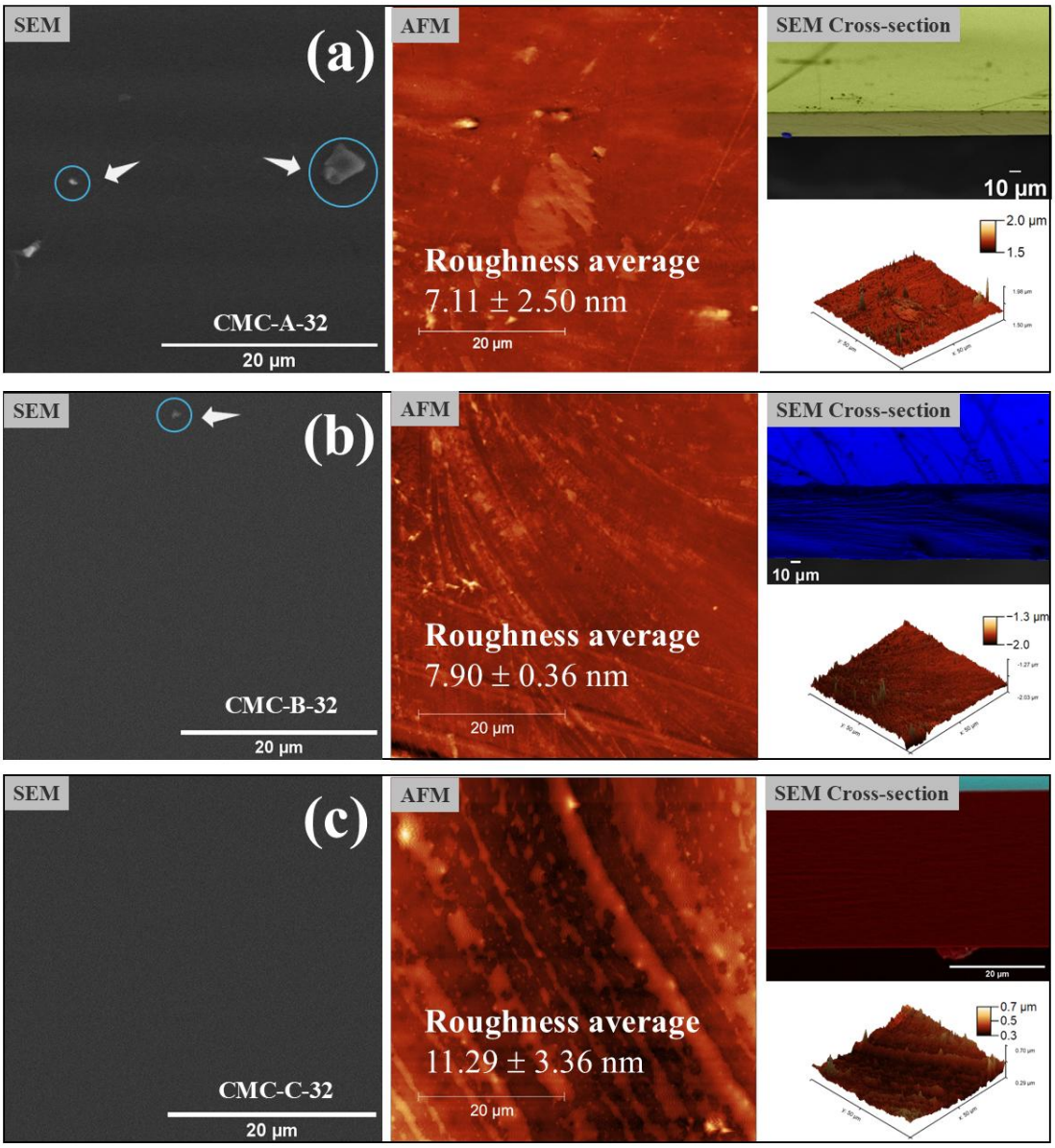

FIGURE 4.16 - SEM images of the surface and cross-section of the films prepared using different concentrations. 1D and 3D AFM images.

The increase in surface roughness observed in the materials may be a determining factor in the enhanced hydrophilicity of the films. The CMC concentration also influenced the mechanical behavior of the films. The MS, TS, and EB results obtained from the tensile tests are summarized in Table 8. A closer analysis of the EM and TS values indicates that the CMC-1.3/100 sample exhibited higher values than CMC-2/100. This result suggests that an intermediate CMC concentration promotes a better balance between structural rigidity and chain mobility, leading to stronger films. In contrast, the higher polymer content in CMC-2/100 may have increased chain aggregation and heterogeneity within the matrix, which can generate stress concentration points and ultimately reduce mechanical performance. Such rigidity and brittleness are common features of polysaccharide-based films, as widely reported for CMC and related biopolymers. For this reason, adding plasticizers to the solution to increase ductility is generally reported [208,209]. Additionally, the EM and TS values in CMC pure films are generally significantly higher than in the EB [196,205,210]. The primary cause of this reduced behavior in films is the presence of hydrogen bonds between the CMC chains. These bonds enhance the cohesiveness between the chains and prevent them from sliding [208].

Table 8. Mechanical properties (EM, TS, and EB), Moisture Content (MC), and Swelling Index (SI) parameters of the CMC-based films.

Films	**EM**† (MPa)	**TS**† (MPa)	**EB**† (%)	**MC**†† (%)	**SI**†† (%)
1/100	36.05 ± 6.92^{b}	27.95 ± 9.24^{a}	$2.21\pm0.20^{a,b}$	25.46 ± 3.23^{a}	3364.14 ± 49.01^{b}
1.3/100	82.97 ± 12.28^{a}	121.84 ± 21.31^{b}	4.33 ± 0.93^{b}	12.06 ± 0.82^{b}	1734.32 ± 112.03^{c}
2/100	65.33 ± 14.69^{a}	79.53 ± 13.49^{c}	$6.14\pm1.94^{b,d}$	14.97 ± 1.82^{b}	4163.57 ± 218.11^{d}

Values with the same superscript letter in the same column are not significantly different ($p < 0.05$) by Tukey's test. † ME, TS, and EB values are represented as mean ± SD (n = 5). †† MC and SI values are represented as mean ± SD (n = 3).

Parameters such as moisture content (MC) and swelling index (SI) are crucial for assessing plastic stability in food packaging applications where water is released. In this sense, the data shown in Table 8 reveal significant differences in the behavior of the samples' MC and SI as a function of the variables analyzed ($p < 0.05$). In the case of MC, the value of the film decreased as the concentration of CMC in the solution increased, indicating a reduction in the interaction between the CMC chains and water. This reduction in the MC value can also be associated with a decrease in the free volume of the polymer chain [204]. Although the MC data observed here are similar to those of other CMC films reported previously, these values are high, and depending on the application, can facilitate the proliferation of microorganisms in food products stored with these materials [126]. Regarding SI, an important characteristic that indicates the film's resistance to water, it was observed that the increase in thickness, caused by the change in concentration and volume of the CMC solution, contributed to the rise in the swelling rate of the films (Table 8). Finally, the 2/100 sample exhibited high SI values, indicating a high swelling capacity of the film and suggesting that the higher polymer concentration may result in increased free spaces between chains, thereby promoting greater water diffusion through the films [126]. On the other hand, the thicker films, i.e., those produced with 1.3 and 2g of CMC, exhibited greater resistance to water solubility, in contrast to films 1/100, which lost their integrity after being immersed in water for 24 hours. Furthermore, these findings align with previous studies [126,211].

4.3.2Effect of adding glycerol and kefiran

Based on the data observed and compared in earlier tests using different concentrations of CMC, the 1.3/100 formulation was selected to continue the study, which involves adding glycerol (12.5%, 25%, and 50% w/w relative to the weight of CMC) as a plasticizer and producing mixtures with kefiran at a proportion 1:1. As shown in Figure 4.18a, the addition of glycerol significantly

increased the thickness of CMC films by 85% when comparing CMC 1/100 with the Gly50 sample. At the same time, the concentration of glycerol also affected the WAC value (Figure 4.18b), resulting in a greater hydrophilicity of the film surface ($\theta < 65$ °), even at low concentrations (Gly 12%), similar to that reported by Chen et al. (2020) [212,213]. In contrast, the Gly25 sample did not show a difference from a sample without plasticizer. This difference in the wettability of CMC samples with glycerol can be attributed to the free energy of the groups available on the film surface [214]. In the case of films based on cellulose or its derivatives without the addition of plasticizers or other materials, the possibility of polar groups such as -OH and C=O being buried is unlikely due to the planar configuration of the chain [214]. In this case, where glycerol was added in different concentrations (Figure 4.18c), we consider that the availability of polar groups on the surface can be adjusted according to the ability of this plasticizer to bind to the CMC network, weaken the hydrogen bonds, and increase or decrease the free volume of the biopolymer [200,213,214].

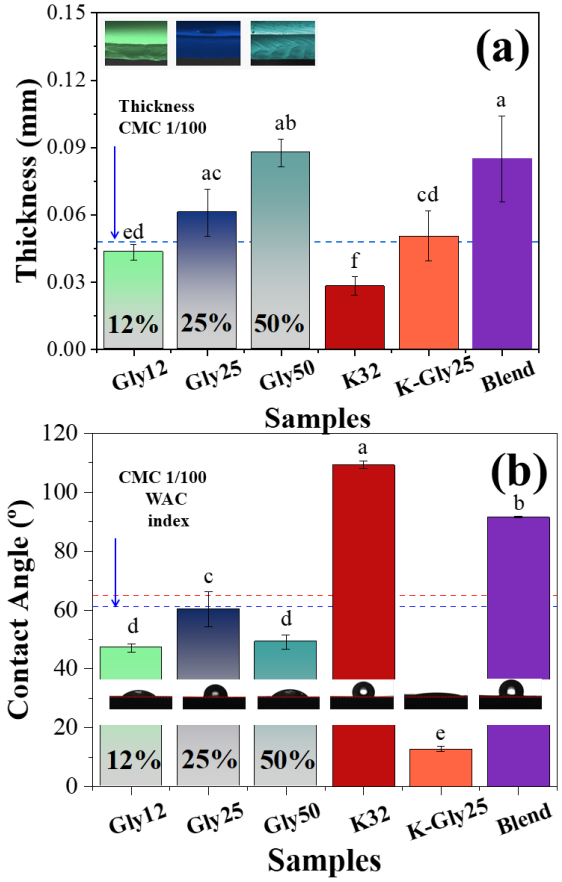

FIGURE 4.17 - (a) Thickness measurement and (b) Water contact angle of CMC samples (under optimized conditions with 1.3 g of carboxymethylcellulose per 100 mL of water) and different concentrations of glycerol.

After selecting a 25% glycerol concentration as a plasticizer, the study on the production of the CMC-kefiran blend was conducted. In terms of thickness, the pure sample was thinner than 1.3/100 sample (Figure 4.18a); it was still possible to produce a firm, integral, and non-cracking film with a thickness ~150% less than that reported by Pop et al. (2021). However, this changed with the addition of 25% glycerol, and consequently, the production of the blend between CMC and Kefiran. The WAC value of the kefiran pure sample was 43% higher than that of the 1.3/100 sample, which is a value similar to that reported by Ghasemlou et al. (2011) and Shahabi-Ghahfarrokhi et al. (2015)[215,216]. Meanwhile, compared to 1.3/100, the addition of the plasticizer reduced the water contact angle by approximately 85%. This increase in hydrophilic character

observed in the K-Gly25 film may be related to the increased exposure of hydroxyl groups on the surface or free volume in the chain [217]. However, the material exhibited a hydrophobic characteristic when combined with kefiran and CMC/glycerol. This could probably be due to effective compatibility between the materials, which would reduce the availability of hydroxyl groups in both phases [200].

The study of the ideal concentration of plasticizer also makes it possible to balance the properties obtained previously, such as the water vapor permeability of the films [217]. In this sense, the impact of different glycerol concentrations on CMC films, pure kefiran films and the blend is shown in Figure 4.19a. As can be seen, the increase in plasticizer resulted in a decrease in the barrier capacity of the films, which is in line with the increase in film thickness. On the other hand, pure kefiran films have a lower WVP value than CMC films (blue dashed line). This low WVP value for kefiran film is lower than that reported by Ghasemlou et al. (2011) [216] and may be associated with the lower mobility of the EPS chains and reduced diffusibility. In the kefiran sample with plasticizer, a concentration of 25% was used, in which no significant difference was observed concerning the CMC sample with the same amount of glycerol. This behavior can be attributed to changes in the conformation of the chains, their reduced mobility, and the increased structural density of the film, which reduces the diffusibility of water from the surface [207,218]. On the other hand, the WVP value for the blend increases, resulting in a decrease in the film's barrier capacity. This phenomenon may be associated with greater electrostatic repulsion between the two polymers, increased free volume, and enhanced water vapor diffusion [207].

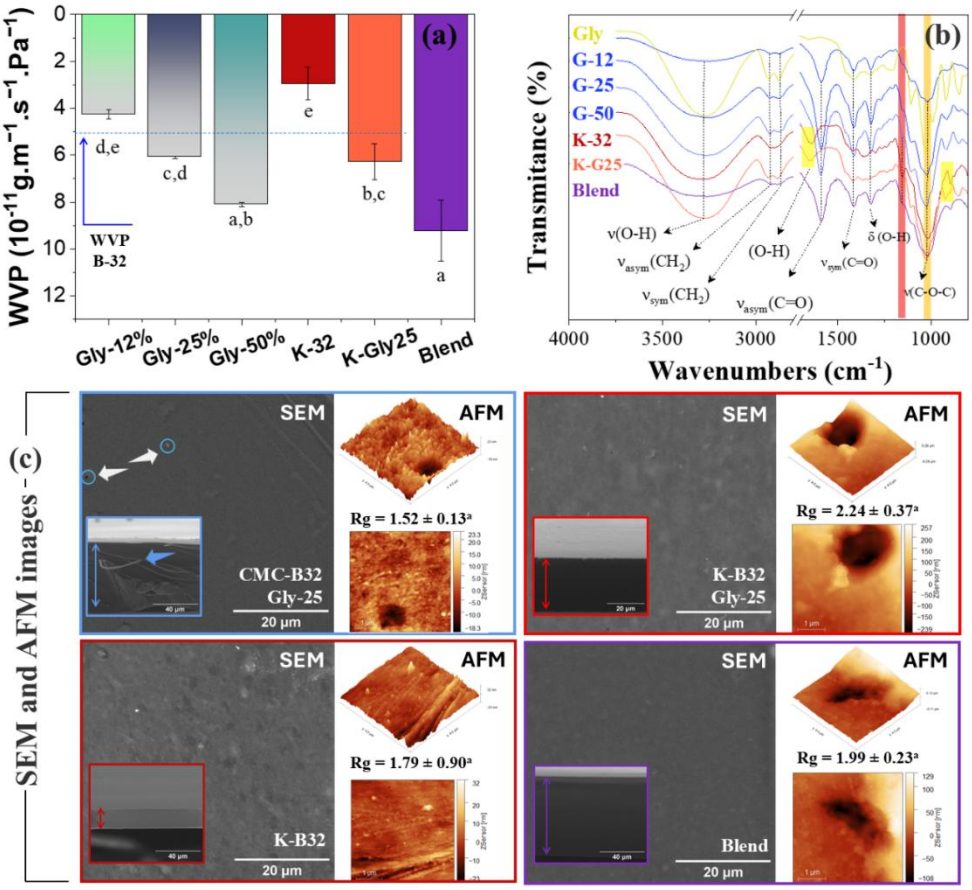

FIGURE 4.18 - (a) WVP values, (b) FT-IR spectra and (c) SEM and AMF images of CMC samples (under optimized conditions with 1.3 g of carboxymethylcellulose per 100 mL of water) and different concentrations of glycerol.

Figure 4.29b displays the FT-IR spectra of the CMC films prepared with varying glycerol concentrations, the pure kefiran film, and the blend. The glycerol bands are similar to those observed in CMC spectra [219]. The peak located at 1644 cm^{-1} (first yellow box), adjacent to this one, is present in the samples containing Kefiran and can be attributed to the presence of -OH[24,43]. This more prominent peak can be attributed to the greater presence of these groups in the kefiran chain than in CMC. In addition, the peak located at 1152 cm^{-1} (highlighted red bar), also observed in samples containing kefiran, is a characteristic fingerprint of the polymer, as it is associated with the vibrational modes of glucose, galactose, and the β bond[43]. In addition, the peak located at ~1022 cm^{-1} (highlighted orange bar)

shows a shift between the samples with added glycerol, which may be indicative of the plasticizer's interaction with the CMC chain. Finally, the peak located at ~900 cm^{-1} is indicative of the presence of glucose and galactose [24]. In the case of the kefiran samples, a significant shift in the position of this band can be observed (second yellow box).

It is possible to observe rougher regions on the surface of the film produced with Kefiran alone (Figure 4.19c). In contrast, a reduction in the film's roughness is observed when the plasticizer is added. The surface of the film produced from the blend shows greater homogeneity between the polymers compared to the micrographs of the K-B-32 films and K-B-32-Gly. The cross-sectional images show an increase in the thickness of the films, both in the samples with glycerol and in the film produced from the blend (insert Figure 4.19c). It is also evident that the cross-section of the films is free of voids, cavities and cracks. This homogeneity can be attributed to the establishment of electrostatic interactions and hydrogen bonds between the CMC/Glycerol, Kefiran/Glycerol, and CMC/Glycerol/Kefira networks [220]. The 2D and 3D AFM images show that the B-32-Gly25% sample has an inhomogeneous surface and low roughness, with a value of 1.52 ± 0.13 nm (Figure 4.19c). On the other hand, despite the increase in surface roughness of the pure kefiran film (1.79 ± 0.90 nm), no cavitations or very pronounced unevenness were observed. In the kefiran sample with the addition of the plasticizer, there was greater homogenization of the surface and an increase in roughness (2.24 ± 0.37 nm). In the case of the film produced from the mixture of kefiran and CMC, there was a decrease in roughness (1.99 ± 0.23 nm).

The improvement in the elasticity of CMC films is one of the most notable characteristics following the addition of glycerol to the polymer matrix [221]. This behavior was observed in the Gly25% sample, which showed a reduction in TS of ~75% compared to the B-32 sample. At the same time, EB values

increased significantly from 4.33% (B-32) to 25.95% (B32-G50). This reduction in TS values and increase in EB is yet another indication of the decrease in intermolecular forces between the polymer chains caused by the addition of glycerol (Table 9) [209].

Table 9. Mechanical properties, including Elastic modulus (EM, MPa), Tensile Strength (TS, MPa), Elongation at break (EB, %), and water contact angle, of films based on the optimized CMC sample with different glycerol concentrations as plasticizer.

Films	EM† (MPa)	TS† (MPa)	EB† (%)	MC†† (%)	SI†† (%)
B-32	82.97±12.28	121.84±21.31	4.33 ± 0.93	12.06±0.82	1734.32±112.03
CMC-G12	23.97±5.13	29.88±4.31	3.34±0.55	9.81±0.70	947.91±162.03
CMC-G25	10.36±2.09	11.32±1.23	5.63±0.67	21.44±2.63	847.24±110.87
CMC-G50	3.47±0.83	14.42±1.73	25.95±2.26	26.79±2.34	1193.52±22.61
K32	38.49±11.88	37.82±4.08	1.56±0.25	16.06±1.69	195.91±5.81
K32-G25	**	**	**	52.89±3.43	651.63±10.37
BLEND	10.19±2.63	11.70±1.39	14.78±1.87	20.80±2.18	349.84±7.55

B-32 represents the optimized CMC condition (1.3 g of carboxymethylcellulose per 100 mL of water). CMC-G12, CMC-G25, and CMC-G32 correspond to the films prepared with different glycerol concentrations used in the casting process. K32 and K32-G25 represent, respectively, the pure kefiran film and the kefiran film containing 25% glycerol.

The moisture content of the samples with varying plasticizer concentrations increased significantly ($p < 0.05$), ranging from 9.81% to 26.79%. These results are consistent with those reported by Akhtar et al. (2023) [194]. At the

same time, the moisture content (MC) values of the pure kefiran film are low and comparable to those reported by Pop et al. (2021)[59] and Ghasemlou et al. (2011)[222]. This behavior may be related to the formation of covalent bonds between glycerol and kefiran, which limits the availability of hydroxyl groups. This, in turn, directly affects the interaction of the ESP with water, consequently influencing the film's moisture content. Adding glycerol to the kefiran matrix significantly increased the film's interaction with water, increasing the moisture content to approximately 53%. On the other hand, the film produced from the blend demonstrated that polymer compatibilization effectively reduces strong interactions with water, resulting in a lower moisture content (~21%) compared to the Gly25 sample. Regarding the degree of swelling of the films after 24 hours of immersion in water, the film produced with 25% glycerol showed a reduction of approximately 95% compared to the CMC sample without plasticizer. This reduction in swelling observed for Gly-25% supports the hypothesis of decreased free space between polymer chains, as proposed in the mechanism illustrated in Figure 4.18c. In kefiran films, both with and without plasticizer, swelling values higher than those commonly reported in the literature were observed [59,222].

Considering these results, the films produced here show a good balance between mechanical properties suitable for food packaging applications and controlled hydrophobicity due to the combination of CMC, kefiran, and the plasticizer. Although the swelling index and moisture content values were relatively high for all the films presented, this is a highly positive aspect considering the intended application. These polysaccharide-based films strongly interact with water and can dissolve and subsequently undergo hydrolysis reactions into low molecular weight sugars and final mineralization into CO_2 and H_2O [223].

4.4 Nanocomposite films based on CMC-kefiran and ZnO

The optimal film formulation previously developed using 25% glycerol and a 1:1 ratio of CMC to kefiran served as the basis for preparing the nanocomposite films. Figure 4.20a shows the X-ray diffractograms of nanocomposite films produced with different concentrations of ZnO (5, 10, and 25 wt%). In the ZnO-containing samples, the intensity of the central diffraction peaks corresponding to the ZnO phase (JCPDS No. 36-1451), specifically those associated with the (100), (002), and (101) planes, increases proportionally with the ZnO content. These peaks are characteristic of the hexagonal wurtzite structure of ZnO. Notably, the nanocomposite films exhibit preferential growth along the (100) plane, whereas in the ZnO powder sample, the (101) plane is more prominent [224]. In addition, these XRD patterns show a broad peak at ~20º relative to 2θ, which corresponds to the crystalline phase of both kefiran and CMC and confirms the presence of both in the composite [27,83]. Raman spectroscopy was employed to investigate the vibrational properties of ZnO within the nanocomposite films (Figure 4.20b). This technique is particularly useful for analyzing materials such as ZnO's structural characteristics and crystallinity. In the hexagonal wurtzite structure, which belongs to the space group $P6_3mc$, ZnO's phonon modes at the Γ point can be classified as: $A_1 + E_1 + 2E_2 + 2B_1$ [225]. Among these, the E_2 modes (low and high) are Raman-active and are commonly used to assess crystal orientation and defects [225,226].

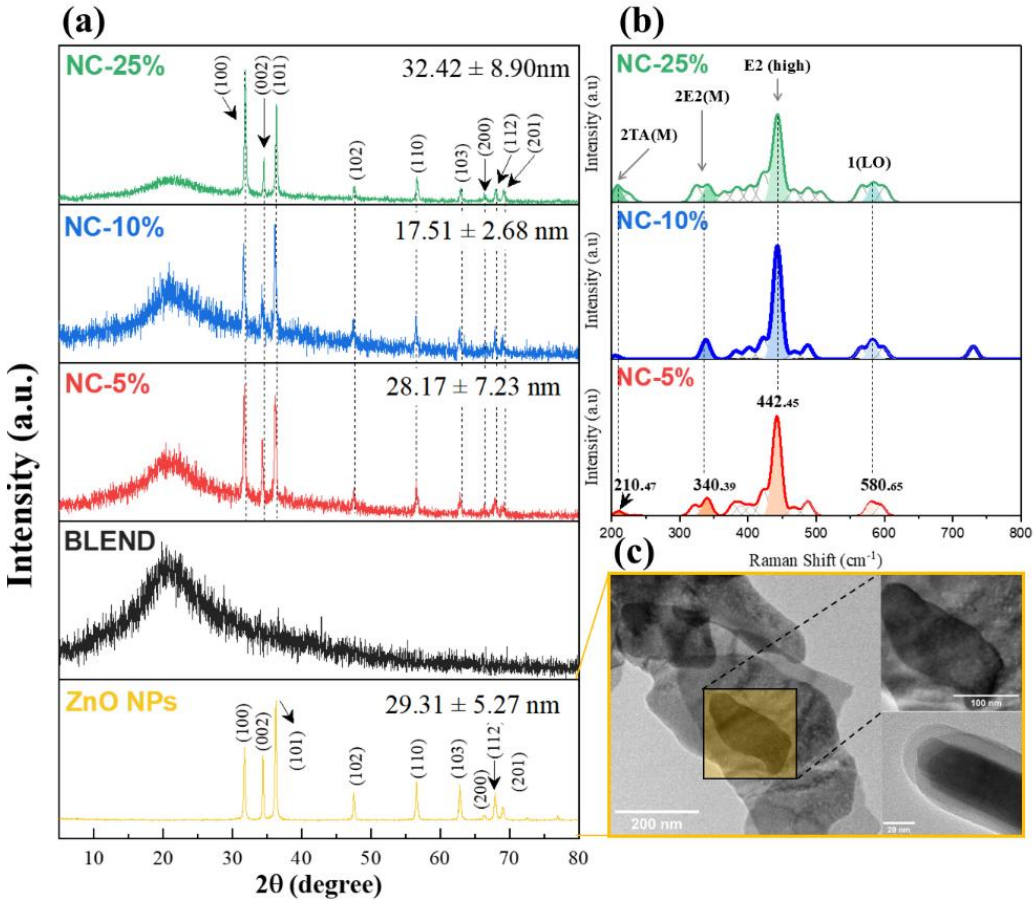

FIGURE 4.19 - (a) XRD patterns of the nanocomposite films, (b) Raman spectra of the nanocomposite films, and (c) TEM images of ZnO nanoparticles. The films were produced with ZnO contents of 5, 10, and 25%.

As shown in Figure 4.20b, prominent Raman peaks appear at approximately 210 cm^{-1}, 342 cm^{-1}, 443 cm^{-1}, and 582 cm^{-1}. The peak at ~210 cm^{-1} is attributed to the second-order transverse acoustic mode 2TA(M), while the one at ~342 cm^{-1} corresponds to either a second-order mode $2E_2(M)$ or a difference mode [$E_2(high) – E_2(low)$]. The sharp peak at ~443 cm^{-1} is associated with the nonpolar $E_2(high)$ mode, which is indicative of the wurtzite phase and reflects the presence of well-crystallized ZnO[226]. The broad peak at ~582 cm^{-1} is typically assigned to the $A_1(LO)$ or $E_1(LO)$ longitudinal optical modes, often associated with structural defects, oxygen vacancies, or surface phonon effects[226]. Collectively, the presence of these modes confirms the incorporation of ZnO with preserved wurtzite structure in the nanocomposite[227]. Figure 4.21c shows a TEM

image of the ZnO powder sample, revealing that the nanoparticles possess a nanoplate-like morphology and an average size of 90 ± 17 nm. These nanoplates exhibit well-defined edges and flat surfaces, which may contribute to the observed preferential growth orientation in the XRD patterns.

The incorporation of ZnO NPs into the CMC and kefiran matrix led to films with a noticeable increase in surface roughness, as observed in the SEM images (Figure 4.21a–c). This effect became more pronounced with increasing ZnO concentration, where the formation of nanoparticle aggregates contributed to greater surface irregularity. Despite this, the films remained free of cracks or bubbles, indicating good structural integrity. Furthermore, the cross-sectional SEM images (insets in Figure 4.21a–c) clearly show that the film thickness increases with ZnO loading and confirm the presence and dispersion of the nanoparticles throughout the film matrix. AFM measurements revealed a progressive increase in surface roughness (Ra), with values of 2.44 ± 0.77 nm, 3.46 ± 1.10 nm, and 7.25 ± 1.47 nm for films containing 5%, 10%, and 25% ZnO, respectively. This indicates that higher nanoparticle content contributes to increased surface irregularity. These findings are also in line with those reported by Jaleh et al. (2022)[228] on nanocomposite films produced with polycarbonate and ZnO. The EDX mapping confirmed the presence and distribution of ZnO throughout the film thickness, with a more intense Zn signal at higher concentrations.

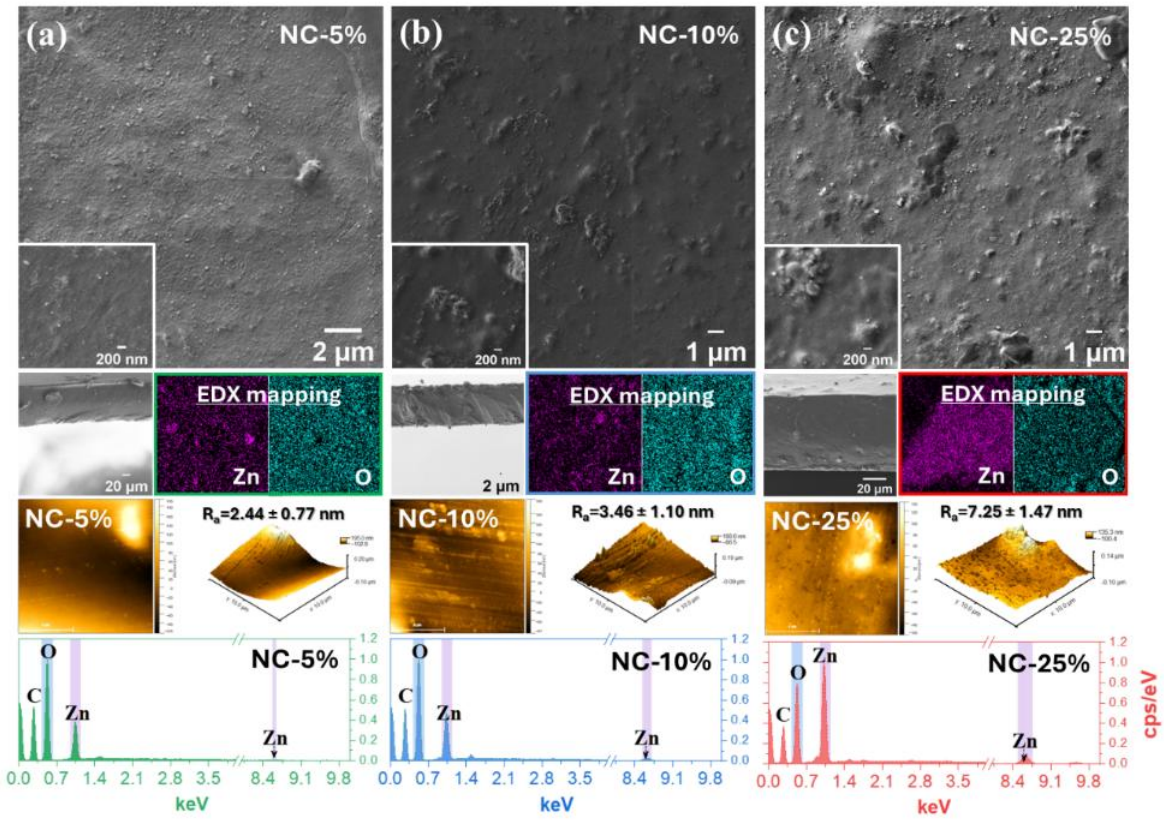

FIGURE 4.20 - Surface, compositional, and morphological characterization of nanocomposite films containing (a) 5%, (b) 10%, and (c) 25% ZnO. Top: SEM micrographs of the film surfaces at different magnifications. Middle: Cross-sectional SEM images and EDX elemental mapping of Zn and O. Bottom: 1D and 3D AFM images for 5%, 10%, and 25% ZnO, respectively.

XPS analysis provided detailed information on the surface composition and chemical states present in the nanocomposite films, confirming the incorporation of the ZnO NPs into the matrix. As shown in Figure 4.27a, the survey spectra confirm the presence of C, O, and Zn in the ZnO-containing samples, along with a Na signal attributed to the sodium salt form of CMC used in the formulation. The detection of Zn 2p peaks exclusively in the NC-5%, NC-10%, and NC-25% samples confirms the successful incorporation of ZnO nanoparticles into the blend matrix. High-resolution C 1s spectra (Figure 4.22b) exhibit components assigned to C–C/C–H (~284.4 eV), C–O (~285.8–286.2 eV),

and O–C=O (~288.2–288.3 eV), consistent with the chemical structure of the polysaccharide-based matrix [228].

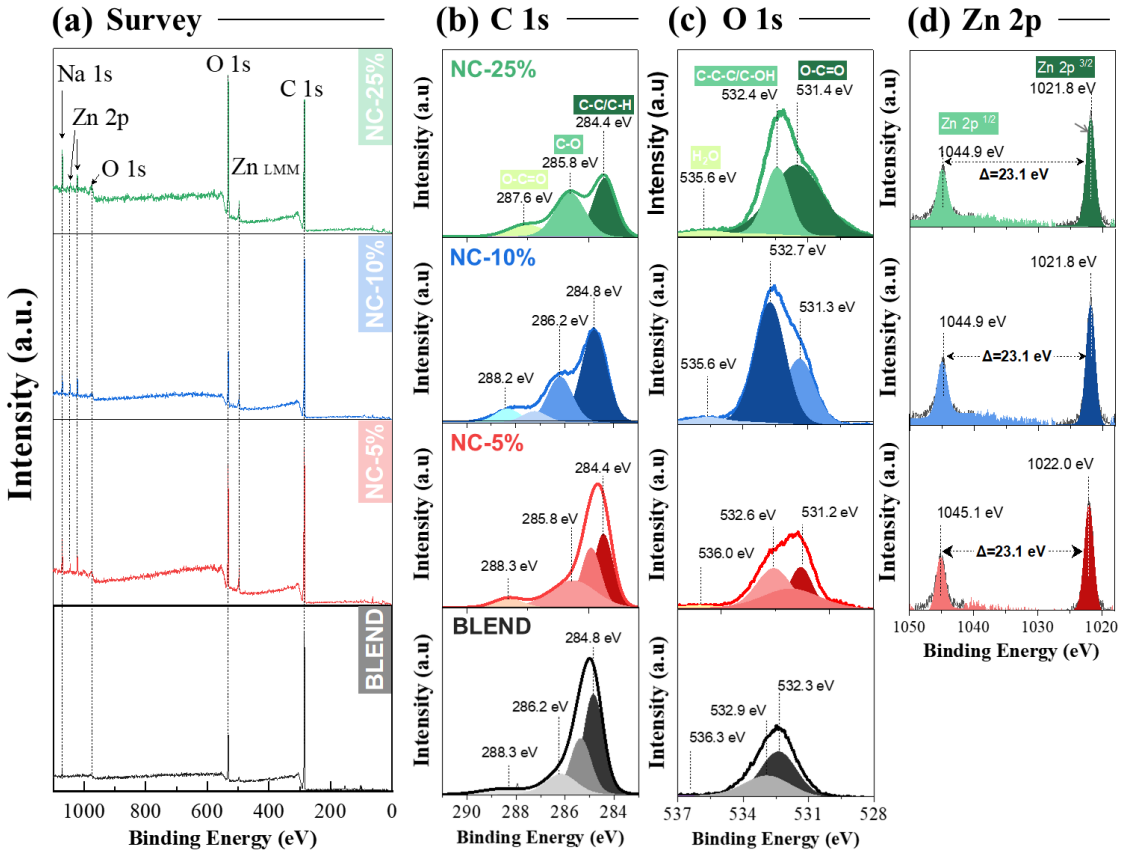

FIGURE 4.21 - XPS analysis of nanocomposite films containing 0% (BLEND), 5%, 10%, and 25% ZnO. (a) Survey spectra show signals corresponding to C 1s, O 1s, and Zn 2p; (b) High-resolution C 1s spectra are deconvoluted into components, (c) High-resolution O 1s spectra, and (d) Zn 2p region.

The O 1s region Figure 4.22c reveals peaks corresponding to C–O/C–OH or Zn-OH, typically associated with chemically or physically adsorbed water (~532.4–532.9 eV), as well as Zn–O bonds (~531.2–531.6 eV). Notably, both the shape of the O 1s peak and the position of its deconvoluted components shift slightly with increasing ZnO content. These variations may reflect changes in the local bonding environment of Zn–O, likely due to differences in particle distribution or interaction with the polymeric matrix. In addition, the presence of C–O–C/C–OH and O–C=O bonds is dominant in all samples, consistent with the

findings reported by Guerrero et al. (2013)[229]. Finally, the Zn 2p spectra (Figure 4.23d) show characteristic peaks of Zn^{2+} located at ~1021.5 eV (Zn $2p_{3/2}$) and ~1044.6 eV (Zn $2p_{1/2}$). The measured spin–orbit splitting of approximately 23.1 eV aligns with previously reported values, confirming that ZnO within the films remains in its typical oxidation state and retains the wurtzite crystalline structure of composite films [230].

The FT-IR spectra of the films, shown in Figure 4.23a, display a broad band centered around 3257 cm^{-1}, corresponding to the stretching vibrations of hydroxyl groups (–OH). This band exhibits a shift towards shorter wavelengths, which aligns with the observation by Li et al. (2021) [84], who attributed this behavior to strong H-bonding interactions between Zn^{2+} and the hydroxyl groups of cellulose. In the spectrum of the film without ZnO nanoparticles, distinct peaks at approximately 2992 and 2875 cm^{-1} are observed, which are attributed to the asymmetric and symmetric stretching vibrations of CH_2 groups, respectively[83,231]. These bands remain essentially unchanged upon ZnO incorporation, indicating that the polymer structure is maintained [85]. The band at 1585 cm^{-1}, associated with the asymmetric stretching of C=O groups, exhibits a slight shift to higher wavenumbers in ZnO-containing films, suggesting potential interactions between ZnO and carboxylate groups [85,231]. In addition, the C–O–C stretching vibration, observed initially at 921 cm^{-1} in the blend film, shifts to lower wavenumbers (as low as 892 cm^{-1} in NC-10%), which may indicate alterations in the ether bonding environment resulting from cross-linking interactions between the kefiran/CMC chains and the ZnO nanoparticles. Similar C–O–C and C=O band shifts have been reported in CMC/ZnO and chitosan/ZnO nanocomposites, where FT-IR shifts were associated with coordination between ZnO and polymer functional groups [232].

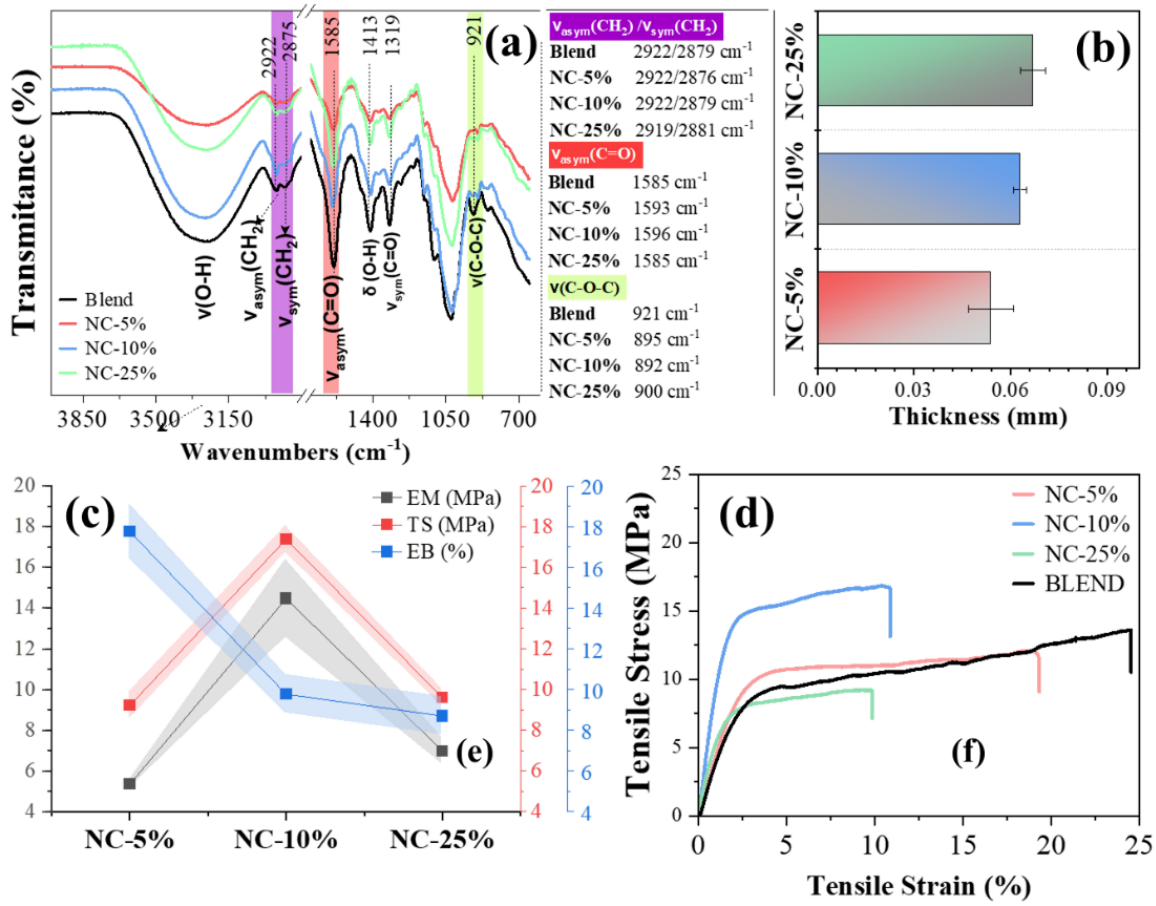

FIGURE 4.22 - (a) FT-IR spectra of the films, (b) Thickness, (c) Mechanical parameters: EM, TS, and EB, and (d) Representative stress–strain curves of the films: Blend, NC-5%, NC-10%, and NC-25%.

As expected, the addition of ZnO NPs significantly influenced the film thickness, as shown in Figure 4.23b. This increase in thickness had a direct impact on the mechanical performance of the films, likely due to changes in structural density and nanoparticle distribution within the matrix. Firstly, the blend film displayed the lowest elastic modulus (EM) and tensile strength (TS) values, but the highest elongation at break (EB), suggesting a softer and more stretchable material. In contrast, the nanocomposite film containing 10% ZnO NPs exhibited the most favorable mechanical profile, with the highest values for both EM and TS, indicating enhanced stiffness and resistance. The film with 25% ZnO NPs exhibited a decline in both EM and TS, likely due to excessive nanoparticle loading, which led to agglomeration and microstructural defects that can serve as

stress concentrators. Additionally, the EB decreased progressively with increasing ZnO content, reflecting reduced film flexibility and extensibility.

The influence of ZnO NPs content on the physical and barrier properties of the nanocomposite films is summarized in Figure 4.24. The WCA values of the films containing 5% and 10% ZnO were $82.08 \pm 3.31°$ and $86.26 \pm 8.94°$, respectively, indicating hydrophobic surface characteristics (Figure 4.24a) However, the difference between them was not statistically significant ($p > 0.05$); nonetheless, the 10% ZnO sample exhibited wettability similar to that of the nanoparticle-free blend film. On the other hand, the film containing 25% ZnO exhibited a marked decrease in WAC ($50.78 \pm 3.71º$), indicating increased surface wettability and a more hydrophilic character. Yu et al. (2023) [233] also reported a reduction in the WCA of chitosan films with ZnO and attributed this effect to the hydrophilicity of the NPs. On the other hand, it is more common to observe an increase in the hydrophobic character of films containing nanoparticles. The opposite behavior observed in the sample with 25% ZnO may be attributed to a higher accumulation of nanoparticles at the surface, which, as previously discussed, is accompanied by a significant increase in surface roughness. This greater surface irregularity may lead to the formation of micro-fissures or discontinuities, facilitating water penetration and enhancing wettability[234]. Consequently, despite the inherent hydrophobicity of ZnO, the morphological changes introduced at higher concentrations may promote a more hydrophilic surface response.

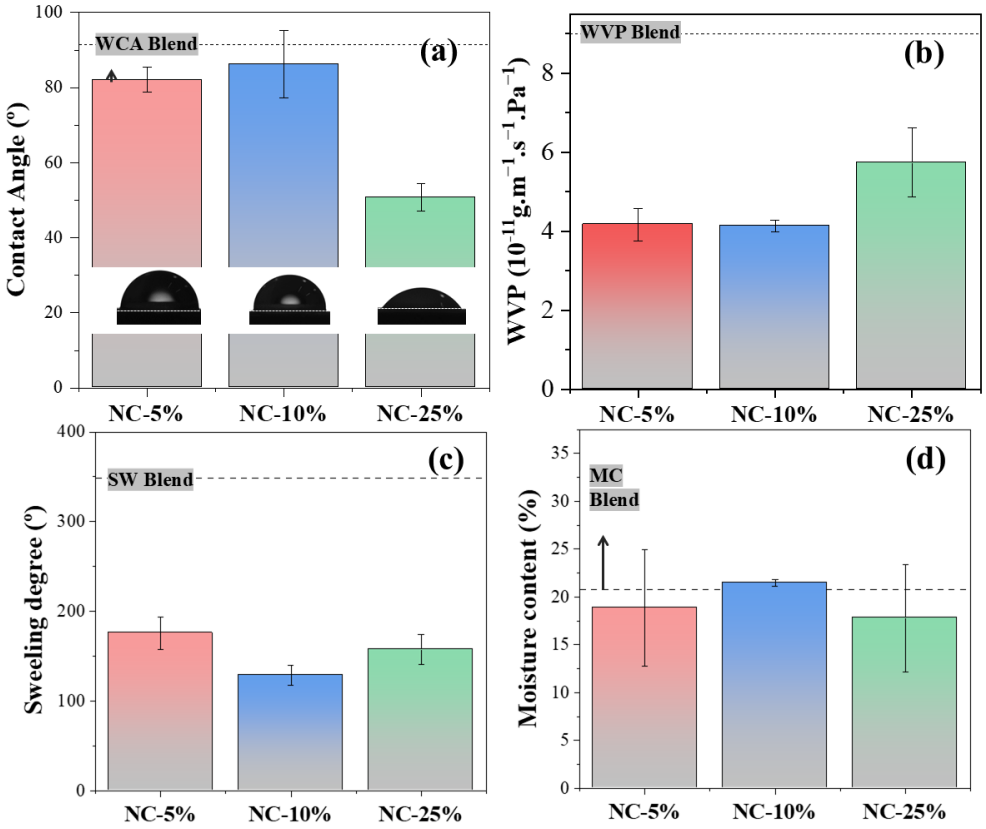

FIGURE 4.23 - Water-related properties of nanocomposite films containing different ZnO concentrations (NC-5%, NC-10%, and NC-25%) compared to the blend film. (a) Water vapor permeability (WVP), (b) water contact angle (WCA) with inset images of water droplets, (c) swelling degree (SW), and (d) moisture content (MC). Dashed lines indicate the respective values for the blend film. Error bars represent standard deviations.

The WVP values (Figure 4.24b) slightly increased in the NC-25% film compared to NC-5% and NC-10%, indicating a possible reduction in barrier efficiency at higher ZnO concentrations. This may be attributed to the formation of microdefects or discontinuities in the film structure resulting from excessive nanoparticle loading. However, these values are lower than those observed in the blend film, indicating that the incorporation of ZnO improved water vapor resistance. This enhancement may be attributed to several factors, including the reduction in the availability of free hydroxyl groups due to interactions between ZnO and the polymer chains of CMC and kefiran, as well as the filling of

intermolecular voids by the nanoparticles. These effects likely contribute to a denser film structure, which hinders the diffusion of water molecules through the matrix. Swelling degree (Figure 4.24c) was reduced in NC-10% and NC-25% compared to NC-5%, indicating improved dimensional stability in aqueous environments. Lastly, the moisture content (MC) (Figure 4.24d) increased slightly in NC-10%. In contrast, NC-25% showed the lowest value among the ZnO-containing samples, which may reflect differences in ZnO dispersion and interactions with the polymeric matrix.

The visual appearance of the films, as presented in Figure 4.25a, indicates that they became progressively less transparent as the concentration of ZnO NPs increased; however, it was still possible to see through them. This visual characteristic is critically essential in packaging applications because it enables consumers to monitor the food's state, thereby enhancing consumer acceptance[235]. The addition of NPs also affects the color of the film, as demonstrated by CIELab measurements (Figure 4.25b). Analysis of the CIELab color space (Figure 4.25b) revealed small shifts toward the green-yellow region. In addition, the L* values (Figure 4.25c) indicated a moderate reduction in luminosity for the films with higher ZnO content. On the other hand, optical properties such as UV-blocking are crucial in food packaging applications, as they help prevent photodegradation and photocatalytic reactions in photosensitive foods. The UV-blocking performance of the nanocomposite films was significantly affected by ZnO content, as illustrated in Figure 4.25d. Unlike the film obtained from the blend, the nanocomposites exhibited a notable reduction in light transmittance in both the UV-A (315–400 nm) and UV-B (280–315 nm) regions. Studies have shown that UV radiation can induce photochemical reactions that degrade the color, texture, flavor, and nutritional quality of food, ultimately shortening its shelf life[236]. Quantitative analysis confirmed that both UV-A and UV-B blocking efficiencies increased proportionally with ZnO content (Figure 4.25e). As expected, transparency (Figure 4.25f) decreased and opacity (Figure 4.25g)

increased as more ZnO was incorporated, consistent with the greater light scattering caused by the nanoparticles. These results confirm the dual function of ZnO in improving UV protection while modulating optical clarity, making these films promising for active food packaging and light-sensitive applications.

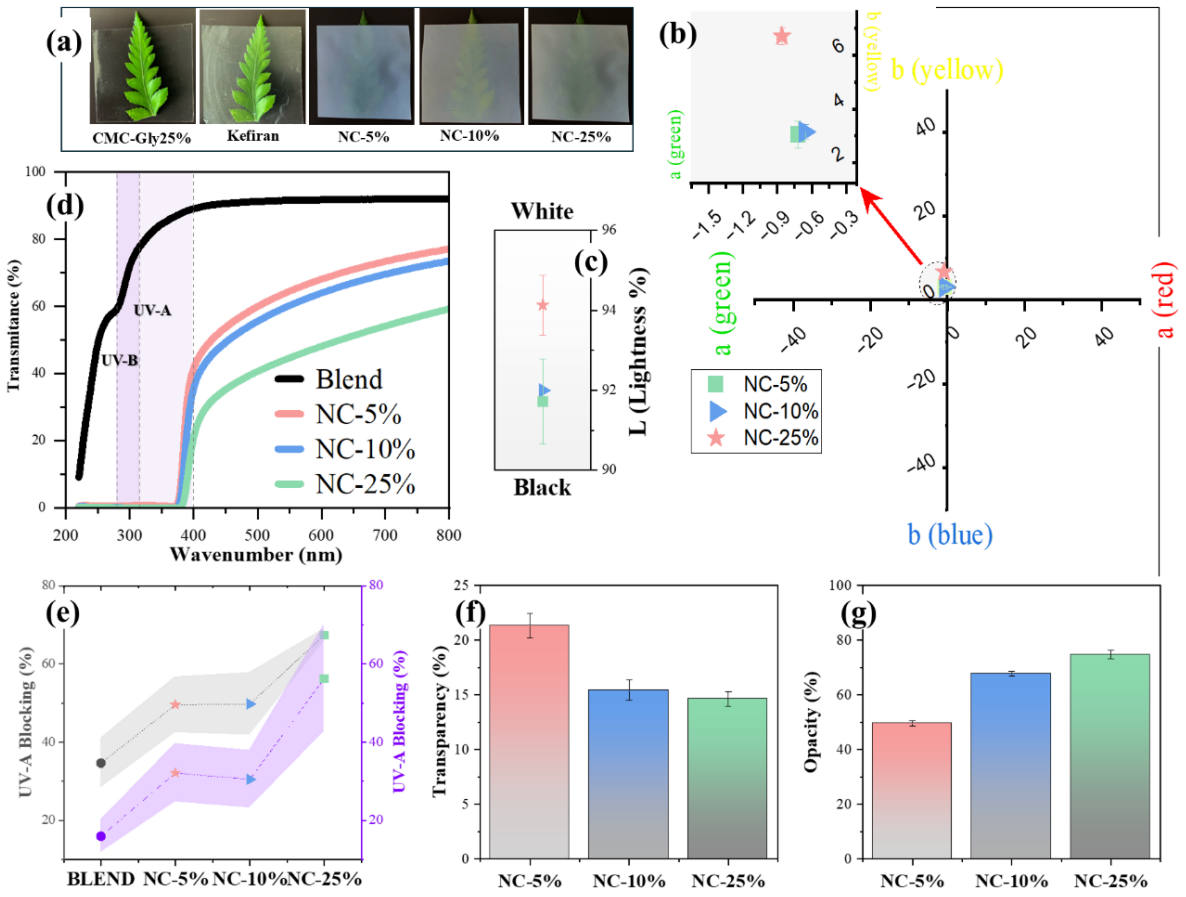

FIGURE 4.24 - Optical, colorimetric, and UV-blocking properties of nanocomposite films containing different concentrations of ZnO, (a) Photographs of film samples, (b) CIELab of the films, (c) Lightness* values, (d) UV–vis transmittance spectra with UV-A and UV-B regions remarked, (e) UV-blocking efficiency for UV-A and UV-B regions, (f) Transparency, and (g) Opacity of the films.

The antibacterial activity of the films was assessed against *E. coli* and *S. aureus* using the agar diffusion method, as shown in Figure 4.26. The bacteriostatic zones of the nanocomposite films showed inhibition comparable to

that reported by Rincón et al. (2023) [237]. These bacteriostatic zones increased with the concentration of ZnO and were slightly larger in the sample with 25% ZnO. This concentration-dependent response supports the well-established antimicrobial activity of ZnO NPs, which is primarily attributed to the generation of ROS, the release of Zn^{2+} ions, and the disruption of bacterial membranes. At the same time, the aggregation and entrapment of ZnO within the polymeric matrix likely reduced the practical exposure of bacteria to the nanoparticle surfaces, thereby limiting the antimicrobial efficiency of the nanoparticles. Notably, the NC-25% composite films exhibited a larger bacteriostatic inhibition zone against *S. aureus* compared to *E. coli*, indicating a higher susceptibility of Gram-positive bacteria. This behavior is consistent with findings reported in previous studies.

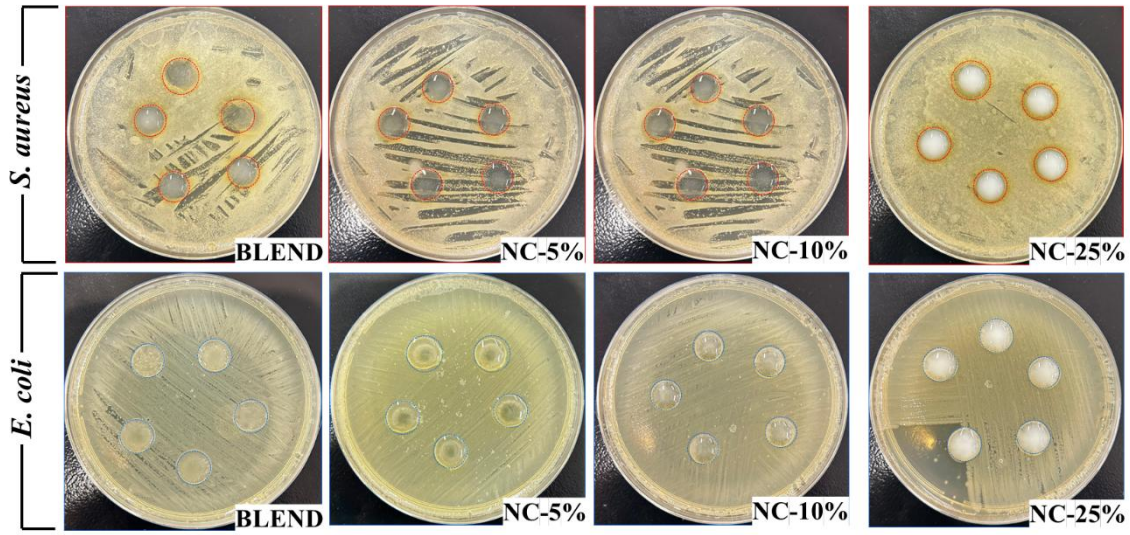

FIGURE 4.25 - Bacteriostatic inhibition zones of blend and nanocomposite films containing different concentrations of ZnO NPs against Escherichia coli and Staphylococcus aureus. The diameters of the inhibition zones indicate the antibacterial effectiveness of the films.

Chapter 5 CONCLUSIONS

In this work, nanocomposite films based on kefiran, CMC and ZnO nanoparticles were developed and characterized with a view to applications in active food packaging. The following conclusions can be drawn from the results obtained:

- ZnO nanoparticles were produced by HaM, showing physicochemical properties that varying experimental parameters can modulate. The ZnO NPs showed selective antimicrobial activity against multidrug-resistant strains of the ESKAPE group, demonstrating their potential as an agent for functionalizing packaging.
- Kefiran was successfully extracted and purified, displaying notable antibiofilm properties. Its application as an edible coating contributed to the preservation of strawberries under both ambient and refrigerated conditions, confirming its functional potential.
- The incorporation of ZnO NPs into kefiran/CMC films led to significant modifications in morphology, structure, and surface properties. Characterization techniques, including SEM, AFM, XRD, XPS, FTIR, and Raman spectroscopy, confirmed the dispersion of the nanostructures, changes in surface roughness, crystalline phases, and chemical interactions between ZnO and the polymer matrix.
- Mechanical properties were notably improved, especially TS and EM, for films with intermediate ZnO contents. However, higher concentrations (25% ZnO) led to increased stiffness and reduced elongation, likely due to aggregation and reduced mobility of the polymer chains.

- Optical properties such as UV-blocking capacity were significantly enhanced by ZnO incorporation. Films showed markedly reduced transmittance in the UV-A and UV-B regions, indicating strong potential to prevent photo-oxidation in sensitive food products.

In summary, the synergistic combination of kefiran, CMC, and ZnO nanoparticles yielded nanocomposite films with enhanced mechanical, structural, barrier, optical, and antimicrobial properties. These results highlight the potential of such systems as sustainable and effective alternatives for active food packaging applications. In addition, it presents, for the first time, the application of kefiran as an edible coating for fruit preservation, along with a comprehensive investigation of kefiran/CMC films functionalized with ZnO NPs. These findings advance current knowledge on polysaccharide-based nanocomposites and open new perspectives for the development of multifunctional materials for food packaging applications.

REFERENCES

1. THIVYA, P., GURURAJ, P. N., REDDY, N. B. P. & RAJAM, R. “Recent advances in protein-polysaccharide based biocomposites and their potential applications in food packaging: A review”. Int J Biol Macromol 268, 131757, 2024.

2. FAYSHAL, M. A. “Current practices of plastic waste management, environmental impacts, and potential alternatives for reducing pollution and improving management.” Heliyon 10, e40838, 2024.

3. YAO, Q. BO ET AL. “Polysaccharide-based food packaging and intelligent packaging applications: A comprehensive review”. Trends Food Sci Technol 147, 104390, 2024.

4. BARNES, D. K. A., GALGANI, F., THOMPSON, R. C. & BARLAZ, M. “Accumulation and fragmentation of plastic debris in global environments”. Philosophical Transactions of the Royal Society B: Biological Sciences 364, 1985–1998, 2009.

5. ARDESTANI, M. M. “Microplastics in the environment: their sources, distribution, and dangerous status”. Water Air Soil Pollut 233, 161, 2022.

6. BRIDSON, J. H., GAUGLER, E. C., SMITH, D. A., NORTHCOTT, G. L. & GAW, S. “Leaching and extraction of additives from plastic pollution to inform environmental risk: A multidisciplinary review of analytical approaches”. J Hazard Mater 414, 125571, 2021.

7. LIU, Z., JIAO, Y., WANG, Y., ZHOU, C. & ZHANG, Z. “Polysaccharides-based nanoparticles as drug delivery systems”. Adv Drug Deliv Rev 60, 1650–1662, 2008.

8. NEŠIĆ, A. ET AL. “Prospect of Polysaccharide-Based Materials as Advanced Food Packaging”. Molecules 2020, Vol. 25, Page 135 25, 135, 2019.

9. AL-HILIFI, S. A., AL-ALI, R. M., DINH, L. N. M., YAO, Y. & AGARWAL, V. “Development of hyaluronic acid based polysaccharide-protein composite edible coatings for preservation of strawberry fruit”. Int J Biol Macromol 259, 128932, 2024.

10. CAZÓN, P., VELAZQUEZ, G., RAMÍREZ, J. A. & VÁZQUEZ, M. “Polysaccharide-based films and coatings for food packaging: A review”. Food Hydrocoll 68, 136–148, 2017.

11. KLEMM, D., HEUBLEIN, B., FINK, H. P. & BOHN, A. “Cellulose: Fascinating Biopolymer and Sustainable Raw Material”. Angewandte Chemie International Edition 44, 3358–3393, 2005.

12. ZHAO, Y. ET AL. “Comprehensive Review of Polysaccharide-Based Materials in Edible Packaging: A Sustainable Approach”. Foods 2021, Vol. 10, Page 1845 10, 1845, 2021.

13. MOHAMMED, A. S. A., NAVEED, M. & JOST, N. “Polysaccharides; Classification, Chemical Properties, and Future Perspective Applications in Fields of Pharmacology and Biological Medicine (A Review of Current Applications and Upcoming Potentialities)”. J Polym Environ 29, 2359, 2021.

14. HARUGADE, A., SHERJE, A. P. & PETHE, A. “Chitosan: A review on properties, biological activities and recent progress in biomedical applications”. React Funct Polym 191, 105634, 2023.

15. SUBRAMANI, G. & MANIAN, R. “Bioactive chitosan films: Integrating antibacterial, antioxidant, and antifungal properties in food packaging”. Int J Biol Macromol 278, 134596, 2024.

16. CHICEA, D. & NICOLAE-MARANCIUC, A. “A Review of Chitosan-Based Materials for Biomedical, Food, and Water Treatment Applications”. Materials 17, 5770, 2024.

17. HU, B. ET AL. “Layer-by-layer assembly of polysaccharide films with self-healing and antifogging properties for food packaging applications”. ACS Appl Nano Mater 1, 3733–3740, 2018.

18. SAPPER, M. & CHIRALT, A. “Starch-Based Coatings for Preservation of Fruits and Vegetables”. Coatings 2018, Vol. 8, Page 152 8, 152, 2018.

19. VADANAN, S. V., BASU, A. & LIM, S. “Bacterial cellulose production, functionalization, and development of hybrid materials using synthetic biology”. Polymer Journal 2022 54:4 54, 481–492, 2022.

20. LINDMAN, B. ET AL. “The relevance of structural features of cellulose and its interactions to dissolution, regeneration, gelation and plasticization phenomena”. Physical Chemistry Chemical Physics 19, 23704–23718, 2017.

21. NORGREN, M. ET AL. “Perspectives on the Lindman Hypothesis and Cellulose Interactions”. Molecules 2023, Vol. 28, Page 4216 28, 4216, 2023.

22. LIU, X., QIN, Z., MA, Y., LIU, H. & WANG, X. “Cellulose-Based Films for Food Packaging Applications: Review of Preparation, Properties, and Prospects”. J Renew Mater 11, 3203–3225, 2023.

23. TRACHE, D. ET AL. “Nanocellulose: From Fundamentals to Advanced Applications”. Front Chem 8, 535734, 2020.

24. MORADI, Z. & KALANPOUR, N. “Kefiran, a branched polysaccharide: Preparation, properties and applications: A review”. Carbohydr Polym 223, 115100, 2019.

25. SIMONELLI, N., GAGLIARINI, N., MEDRANO, M., PIERMARIA, J. A. & ABRAHAM, A. G. “Kefiran. in Polysaccharides of Microbial Origin 99–116”, Springer International Publishing, Cham, 2022. doi:10.1007/978-3-030-42215-8_6.

26. MEDRANO, M., HAMET, M. F., ABRAHAM, A. G. & PÉREZ, P. F. “Kefiran protects Caco-2 cells from cytopathic effects induced by Bacillus cereus infection”. Antonie Van Leeuwenhoek 96, 505–513, 2009.

27. MARANGONI JÚNIOR, L., VIEIRA, R. P. & ANJOS, C. A. R. “Kefiran-based films: Fundamental concepts, formulation strategies and properties”. Carbohydr Polym 246, 2020.

28. SHIOMI, M., SASAKI, K., MUROFUSHI, M. & AIBARA, KAGEAKI. “Antitumor activity in mice of orally administered polysaccharide from kefir grain”. Jpn J Med Sci Biol 35, 75–80, 1982.

29. PIERMARIA, J. A., DE LA CANAL, M. L. & ABRAHAM, A. G. “Gelling properties of kefiran, a food-grade polysaccharide obtained from kefir grain”. Food Hydrocoll 22, 1520–1527, 2008.

30. TAN, K. X., CHAMUNDESWARI, V. N. & LOO, S. C. J. “Prospects of kefiran as a food-derived biopolymer for agri-food and biomedical applications”. RSC Adv 10, 25339–25351, 2020.

31. OLIVEIRA FILHO, J. G. DE ET AL. “Recent advances in kefiran polymer to produce nanofibers and films for food packaging applications”. Food and Humanity 4, 100603, 2025.

32. POTHURAJU, R., YENUGANTI, V. R., HUSSAIN, S. A. & SHARMA, M. “Fermented Milk in Protection Against Inflammatory Mechanisms in Obesity. in Immunity and Inflammation in Health and Disease 389–401”, Elsevier, 2018. doi:10.1016/B978-0-12-805417-8.00029-9.

33. KESENKAŞ, H., GÜRSOY, O. & ÖZBAŞ, H. “Kefir. in Fermented Foods in Health and Disease Prevention 339–361”. Elsevier, 2017. doi:10.1016/B978-0-12-802309-9.00014-5.

34. Georgalaki, M., Zoumpopoulou, G., Anastasiou, R., Kazou, M. & Tsakalidou, E. Lactobacillus kefiranofaciens: From Isolation and Taxonomy to Probiotic Properties and Applications. Microorganisms 2021, Vol. 9, Page 2158 9, 2158 (2021).

35. ALVES, E. ET AL. “Characterization of Kefir Produced in Household Conditions: Physicochemical and Nutritional Profile, and Storage Stability”. Foods 10, 1057, 2021.

36. BENSMIRA, M., NSABIMANA, C. & JIANG, B. “Effects of fermentation conditions and homogenization pressure on the rheological properties of Kefir”. LWT - Food Science and Technology 43, 1180–1184, 2010.

37. GUZEL-SEYDIM, Z. B. ET AL. “Review: Functional Properties of Kefir”. http://dx.doi.org/10.1080/10408390903579029 51, 261–268, 2011.

38. WANG, M. & BI, J. “Modification of characteristics of kefiran by changing the carbon source of Lactobacillus kefiranofaciens”. J Sci Food Agric 88, 763–769, 2008.

39. CHEIRSILP, B. & RADCHABUT, S. “Use of whey lactose from dairy industry for economical kefiran production by Lactobacillus kefiranofaciens in mixed cultures with yeasts”. N Biotechnol 28, 574–580, 2011.

40. MARTINS, E. F. ET AL. “Determination and standardization of the kefiran extraction protocol for possible pharmacological applications”. Carbohydrate Polymer Technologies and Applications 3, 100198, 2022.

41. GRZEBIENIARZ, W., BISWAS, D., ROY, S. & JAMRÓZ, E. “Advances in biopolymer-based multi-layer film preparations and food packaging applications”. Food Packag Shelf Life 35, 101033, 2023.

42. RAD, F. H., SHARIFAN, A. & ASADI, G. “Miscibility and morphology of kefiran/waterborne polyurethane blend films”. Int J Food Prop 20, S2764–S2775, 2017.

43. PIERMARIA, J. ET AL. “Kefiran films plasticized with sugars and polyols: water vapor barrier and mechanical properties in relation to their microstructure analyzed by ATR/FT-IR spectroscopy”. Food Hydrocoll 25, 1261–1269, 2011.

44. EXARHOPOULOS, S., GOULAS, A. & DIMITRELI, G. “Biodegradable Films from Kefiran-Based Cryogel Systems”. Macromol 2, 324–345, 2022.

45. HASHEMINYA, S. M. ET AL. “Development and characterization of biocomposite films made from kefiran, carboxymethyl cellulose and Satureja Khuzestanica essential oil”. Food Chem 289, 443–452, 2019.

46. MOTEDAYEN, A. A., KHODAIYAN, F. & SALEHI, E. A. “Development and characterisation of composite films made of kefiran and starch”. Food Chem 136, 1231–1238, 2013.

47. ESHAGHI, R., MOHSENZADEH, M. & AYALA-ZAVALA, J. F. “Bio-nanocomposite active packaging films based on carboxymethyl cellulose, myrrh gum, TiO2 nanoparticles and dill essential oil for preserving fresh-fish (Cyprinus carpio) meat quality”. Int J Biol Macromol 263, 129991, 2024.

48. CHEN, Z. ET AL. “Highly TVB-N sensitive film with CMS as the ‘bridge’ via electrostatic interaction and hydrogen bond self-assembly for monitoring food freshness in intelligent packaging”. Talanta 252, 123881, 2023.

49. VOLOKHOVA, A. S., EDGAR, K. J. & MATSON, J. B. “Polysaccharide-containing block copolymers: synthesis and applications”. Mater Chem Front 4, 99–112, 2019.

50. OLIVEIRA, R. N. ET AL. “Absorbent polyvinyl alcohol-sodium carboxymethyl cellulose hydrogels for propolis delivery in wound healing applications”. Polym Eng Sci 57, 1224–1233, 2017.

51. RAHMAN, M. S. ET AL. “Recent developments of carboxymethyl cellulose”. Polymers (Basel) 13, 1345, 2021.

52. HASHMI, M. ET AL. “Carboxymethyl Cellulose (CMC) Based Electrospun Composite Nanofiber Mats for Food Packaging”. Polymers 2021, Vol. 13, Page 302 13, 302, 2021.

53. ROY, S. & RHIM, J. W. “Carboxymethyl cellulose-based antioxidant and antimicrobial active packaging film incorporated with curcumin and zinc oxide”. Int J Biol Macromol 148, 666–676, 2020.

54. YILDIRIM-YALCIN, M., TORNUK, F. & TOKER, O. S. “Recent advances in the improvement of carboxymethyl cellulose-based edible films”. Trends Food Sci Technol 129, 179–193, 2022.

55. ROY, S., KIM, H. J. & RHIM, J. W. “Synthesis of Carboxymethyl Cellulose and Agar-Based Multifunctional Films Reinforced with Cellulose Nanocrystals and Shikonin”. ACS Appl Polym Mater 3, 1060–1069, 2021.

56. LI, H., SHI, H., HE, Y., FEI, X. & PENG, L. “Preparation and characterization of carboxymethyl cellulose-based composite films reinforced by cellulose nanocrystals derived from pea hull waste for food packaging applications”. Int J Biol Macromol 164, 4104–4112, 2020.

57. YATAKA, Y., SUZUKI, A., IIJIMA, K. & HASHIZUME, M. “Enhancement of the mechanical properties of polysaccharide composite films utilizing cellulose nanofibers”. Polym J 52, 645–653, 2020.

58. LONG, J., ZHANG, W., ZHAO, M. & RUAN, C. Q. “The reduce of water vapor permeability of polysaccharide-based films in food packaging: A comprehensive review”. Carbohydr Polym 321, 121267, 2023.

59. POP, C. R. ET AL. “The Effect of Extraction Conditions on the Barrier and Mechanical Properties of Kefiran Films”. Coatings 2021, Vol. 11, Page 602 11, 602, 2021.

60. TAVARES, K. M. ET AL. “Effect of carboxymethyl cellulose concentration on mechanical and water vapor barrier properties of corn starch films”. Carbohydr Polym 246, 116521, 2020.

61. MOHAMMADI, H., REZAEIGOLESTANI, M. & MOHSENZADEH, M. “Optimization of antimicrobial nanocomposite films based on carboxymethyl cellulose incorporating chitosan nanofibers and Guggul gum polysaccharide”. Sci Rep 14, 1–17, 2024.

62. AMAREGOUDA, Y. & KAMANNA, K. “Physico-chemical, in-vitro cytotoxicity and antimicrobial evaluation of L-valine functionalised CuO NPs on polyvinyl alcohol and blended carboxymethyl cellulose films”. Indian Chemical Engineer 64, 543–552, 2022.

63. VALIZADEH, S., NASERI, M., BABAEI, S., HOSSEINI, S. M. H. & IMANI, A. “Development of bioactive composite films from chitosan and carboxymethyl cellulose using glutaraldehyde, cinnamon essential oil and oleic acid”. Int J Biol Macromol 134, 604–612, 2019.

64. MOTEDAYEN, A. A., KHODAIYAN, F., ATAI SALEHI, E. & HOSSEINI, S. S. “Characterisation of biocomposite film made of kefiran and carboxymethyl cellulose (CMC)”. Journal of Food and Bioprocess Engineering 2, 61–70, 2019.

65. SHAHABI-GHAHFARROKHI, I., KHODAIYAN, F., MOUSAVI, M. & YOUSEFI, H. “Preparation of UV-protective kefiran/nano-ZnO nanocomposites: Physical and mechanical properties”. Int J Biol Macromol 72, 41–46, 2015.

66. MORADI, Z., ESMAIILI, M. & ALMASI, H. “Development and characterization of kefiran-Al 2 O 3 nanocomposite films: Morphological, physical and mechanical properties”. 2018. doi:10.1016/j.ijbiomac.2018.10.193.

67. ABDELGHANY, T. M. ET AL. “SARS-CoV-2, the other face to SARS-CoV and MERS-CoV: Future predictions”. Biomedical Journal Preprint at https://doi.org/10.1016/j.bj.2020.10.008, 2021.

68. MARQUÈS, M. & DOMINGO, J. L. “Contamination of inert surfaces by SARS-CoV-2: Persistence, stability and infectivity. A review”. Environmental Research vol. 193 Preprint at https://doi.org/10.1016/j.envres.2020.110559, 2021.

69. BUNGAU, S., TIT, D. M., BEHL, T., ALEYA, L. & ZAHA, D. C. “Aspects of excessive antibiotic consumption and environmental influences correlated with the occurrence of resistance to antimicrobial agents.” Curr Opin Environ Sci Health 19, 100224, 2021.

70. FU, D. ET AL. “Polylactic acid/polyvinyl alcohol-quaternary ammonium chitosan double-layer films doped with novel antimicrobial agent CuO@ZIF-8 NPs for fruit preservation”. Int J Biol Macromol 195, 538–546, 2022.

71. SABU MATHEW, S., JAISWAL, A. K. & JAISWAL, S. “A comprehensive review on hydrophobic modification of biopolymer composites for food packaging applications”. Food Packag Shelf Life 48, 101464, 2025.

72. CHANDRABABU, V. ET AL. “Progress in food packaging applications of biopolymer-nanometal composites — A comprehensive review”. Biomaterials Advances 162, 213921, 2024.

73. HASHEMINYA, S. M. ET AL. “Influence of simultaneous application of copper oxide nanoparticles and Satureja Khuzestanica essential oil on properties of kefiran–carboxymethyl cellulose films”. Polym Test 73, 377–388, 2019.

74. HASHEMINYA, S.-M., REZAEI MOKARRAM, R., GHANBARZADEH, B., HAMISHEKAR, H. & KAFIL, H. S. “Physicochemical, mechanical, optical, microstructural and antimicrobial properties of novel kefiran-carboxymethyl cellulose biocomposite films as influenced by copper oxide nanoparticles (CuONPs)”. Food Packag Shelf Life 17, 196–204, 2018.

75. ZOLFI, M., KHODAIYAN, F., MOUSAVI, M. & HASHEMI, M. “Development and characterization of the kefiran-whey protein isolate-TiO2 nanocomposite films”. Int J Biol Macromol 65, 340–345, 2014.

76. YUNTAWATTANA, N., BUABAN, T. & SIRI, T. “Sustainable Active Packaging from On-Demand Degradable PLA/PBAT and Zn-Doped TiO2 Composites”. ACS Omega, 2025. doi:10.1021/ACSOMEGA.4C09138/ASSET/IMAGES/LARGE/AO4C09138_0003.JPEG.

77. RIAHI, Z., EZATI, P., RHIM, J. W., BAGHERI, R. & PIRCHERAGHI, G. “Cellulose Nanofiber-Based Ethylene Scavenging Antimicrobial Films Incorporated with Various Types of Titanium Dioxide Nanoparticles to Extend the Shelf Life of Fruits”. ACS Appl Polym Mater 4, 4765–4773, 2022.

78. ARJUNAN, A. ET AL. “3D Printed Cobalt-Chromium-Molybdenum Porous Superalloy with Superior Antiviral Activity”. International Journal of Molecular Sciences 2021, Vol. 22, Page 12721 22, 12721, 2021.

79. SILVA, T. E. M. ET AL. “Hierarchical structure of 3D ZnO experimentally designed to achieve high performance in the sertraline photocatalysis in natural waters”. Chemical Engineering Journal 475, 146235, 2023.

80. MARQUES, G. N. ET AL. “Selective inhibitory activity of multidrug-resistant bacteria by zinc oxide nanoparticles”. J Environ Chem Eng 12, 111870, 2024.

81. LI, Y. & SHEN, W. “Tuning the Morphology of Metal Oxides for Catalytic Applications”. Nanocatalysis Synthesis and Applications 333–403, 2013. doi:10.1002/9781118609811.CH10.

82. MARQUES, G. N. ET AL. “Synthesis of yttrium aluminate doped with Cr3+ using MgF2–Na2B4O7 as mineralizers to obtain red pigments for ceramic tiles application”. Ceram Int 46, 27940–27950, 2020.

83. LI, N. ET AL. “Development of carboxymethyl cellulose/starch films enriched with ZnO-NPs and anthocyanins for antimicrobial and pH-indicating food packaging”. Int J Biol Macromol 282, 136814, 2024.

84. LI, X. ET AL. “Facile in situ fabrication of ZnO-embedded cellulose nanocomposite films with antibacterial properties and enhanced mechanical strength via hydrogen bonding interactions”. Int J Biol Macromol 183, 760–771, 2021.

85. BADRY, R., SABRY, N. M. & IBRAHIM, M. A. “Enhancing the structural and optoelectronic properties of carboxymethyl cellulose sodium filled with ZnO/GO and CuO/GO nanocomposites for antimicrobial packaging applications”. Sci Rep 14, 1–27, 2024.

86. VASILE, B. S. ET AL. “Synthesis and characterization of a novel controlled release zinc oxide/gentamicin–chitosan composite with potential applications in wounds care”. Int J Pharm 463, 161–169, 2014.

87. SHAHMOHAMMADI JEBEL, F. & ALMASI, H. “Morphological, physical, antimicrobial and release properties of ZnO nanoparticles-loaded bacterial cellulose films”. Carbohydr Polym 149, 8–19, 2016.

88. AL-NABULSI, A. ET AL. “Antimicrobial activity of chitosan coating containing ZnO nanoparticles against E. coli O157:H7 on the surface of white brined cheese”. Int J Food Microbiol 334, 108838, 2020.

89. ATTIA, G. H. ET AL. “Antiviral zinc oxide nanoparticles mediated by hesperidin and in silico comparison study between antiviral phenolics as anti-SARS-CoV-2”. Colloids Surf B Biointerfaces 203, 111724, 2021.

90. SERAY, M., SKENDER, A. & HADJ-HAMOU, A. S. “Kinetics and mechanisms of Zn2+ release from antimicrobial food packaging based on poly (butylene adipate-co-terephthalate) and zinc oxide nanoparticles”. Polymer Bulletin 78, 1021–1040, 2021.

91. URIBE-LÓPEZ, M. C. ET AL. “Photocatalytic activity of ZnO nanoparticles and the role of the synthesis method on their physical and chemical properties”. J Photochem Photobiol A Chem 404, 112866, 2021.

92. SAHU, K. & KAR, A. K. “Counterion-Induced Tailoring of Energy Transfer in Hydrothermally Grown Nanostructured ZnO for Photocatalysis”. Cryst Growth Des 21, 3656–3667, 2021.

93. CATTO, A. C. ET AL. “The role of counter-ions in crystal morphology, surface structure and photocatalytic activity of ZnO crystals grown onto a substrate”. Appl Surf Sci 529, 147057, 2020.

94. BARUAH, S. & DUTTA, J. “Hydrothermal growth of ZnO nanostructures”. Sci Technol Adv Mater 10, 013001, 2009.

95. YANG, G. & PARK, S. J. “Conventional and Microwave Hydrothermal Synthesis and Application of Functional Materials: A Review”. Materials 12,, 2019.

96. TANG, J. ET AL. “ZnO Nanorods with Low Intrinsic Defects and High Optical Performance Grown by Facile Microwave-Assisted Solution Method”. ACS Appl Mater Interfaces 7, 4737–4743, 2015.

97. GUSMÃO, L. A. ET AL. “Alkali influence on ZnO and Ag-doped ZnO nanostructures formation using the microwave-assisted hydrothermal method for fungicidal inhibition”. Journal of Physics and Chemistry of Solids 158, 110234, 2021.

98. ESPARZA GONZÁLEZ, S. C. ET AL. “Antibacterial and anticancer activity of ZnO with different morphologies: a comparative study”. 3 Biotech 11, 68, 123AD.

99. KRISHNAMOORTHY, R. ET AL. “Antibacterial Mechanisms of Zinc Oxide Nanoparticle against Bacterial Food Pathogens Resistant to Beta-Lactam Antibiotics”. Molecules 2022, Vol. 27, Page 2489 27, 2489 , 2022.

100. MARQUES, G. N. ET AL. “Antiviral leather: A functional coating based on SiO2-AgNPs to eliminate pathogens”. J Environ Chem Eng 11, 110919, 2023.

101. ASSIS, M. ET AL. “SiO2-Ag Composite as a Highly Virucidal Material: A Roadmap that Rapidly Eliminates SARS-CoV-2”. Nanomaterials 11, 2021.

102. BISWAS, A., KAR, U. & JANA, N. R. “Cytotoxicity of ZnO nanoparticles under dark conditions via oxygen vacancy dependent reactive oxygen species generation”. Physical Chemistry Chemical Physics 24, 13965–13975, 2022.

103. LIPOVSKY, A. ET AL. “EPR Study of Visible Light-Induced ROS Generation by Nanoparticles of ZnO”. The Journal of Physical Chemistry C 113, 15997–16001, 2009.

104. SÁNCHEZ-LÓPEZ, E. ET AL. “Metal-Based Nanoparticles as Antimicrobial Agents: An Overview”. Nanomaterials 10, 292, 2020.

105. MENICHETTI, A., MAVRIDI-PRINTEZI, A., MORDINI, D. & MONTALTI, M. “Effect of Size, Shape and Surface Functionalization on the Antibacterial Activity of Silver Nanoparticles”. Journal of Functional Biomaterials 2023, Vol. 14, Page 244 14, 244, 2023.

106. CHOI, O. & HU, Z. “Size Dependent and Reactive Oxygen Species Related Nanosilver Toxicity to Nitrifying Bacteria”. Environ Sci Technol 42, 4583–4588, 2008.

107. TAKAHASHI, C., YAMADA, T., YAGI, S., MURAI, T. & MUTO, S. “Preparation of silver-decorated Soluplus® nanoparticles and antibacterial activity towards S. epidermidis biofilms as characterized by STEM-CL spectroscopy”. Materials Science and Engineering: C 121, 111718, 2021.

108. MEHRALI, F., ZIYADI, H., HEKMATI, M., FARIDI-MAJIDI, R. & QOMI, M. “Kefiran/poly(vinyl alcohol)/poly(vinyl pyrrolidone) composite nanofibers: fabrication, characterization and consideration of effective parameters in electrospinning”. SN Appl Sci 2, 895, 2020.

109. QIN, N. ET AL. “RNA-Seq-based transcriptome analysis of methicillin-resistant Staphylococcus aureus biofilm inhibition by ursolic acid and resveratrol”. Scientific Reports 2014 4:1 4, 1–9, 2014.

110. LI, H. ET AL. “Edible chitosan-based Pickering emulsion coatings: Preparation, characteristics, and application in strawberry preservation”. Int J Biol Macromol 264, 130672, 2024.

111. TOBY, B. H. & VON DREELE, R. B. “GSAS-II: the genesis of a modern open-source all purpose crystallography software package”. urn:issn:0021-8898 46, 544–549, 2013.

112. LÓPEZ, R. & GÓMEZ, R. “Band-gap energy estimation from diffuse reflectance measurements on sol-gel and commercial TiO 2: A comparative study”. J Solgel Sci Technol 61, 1–7, 2012.

113. WHO global priority pathogens list of antibiotic-resistant bacteria - Combat AMR. https://www.combatamr.org.au/news-events/who-global-priority-pathogens-list-of-antibiotic-resistant-bacteria.

114. CRUZ, C. D., ESTEVE, P. & TAMMELA, P. “Evaluation and validation of Biolog OmniLog® system for antibacterial activity assays”. Lett Appl Microbiol 72, 589–595, 2021.

115. MOREIRA, A. J. ET AL. “Photodegradation of Fluoxetine Applying Different Photolytic Reactors: Evaluation of the Process Efficiency and Mechanism”. Article J. Braz. Chem. Soc 30, 1010–1024, 2019.

116. SCHNEIDER, J. T., FIRAK, D. S., RIBEIRO, R. R. & PERALTA-ZAMORA, P. “Use of scavenger agents in heterogeneous photocatalysis: truths, half-truths, and misinterpretations”. Physical Chemistry Chemical Physics 22, 15723–15733, 2020.

117. MOREIRA, A. J. ET AL. “Prozac® photodegradation mediated by Mn-doped TiO2 nanoparticles: Evaluation of by-products and mechanisms proposal”. J Environ Chem Eng 8, 104543, 2020.

118. WOLD, S., ESBENSEN, K. & GELADI, P. “Principal component analysis”. Chemometrics and Intelligent Laboratory Systems 2, 37–52, 1987.

119. R: A Language and Environment for Statistical Computing.

120. ASTM D882. Test Method for Tensile Properties of Thin Plastic Sheeting. Preprint at https://doi.org/10.1520/D0882-18, 2018.

121. BARBOSA, M. L. ET AL. « Evaluation the Potential of Onion/Laponite Composites Films for Sustainable Food Packaging with Enhanced UV Protection and Antioxidant Capacity”. Molecules 2023, Vol. 28, Page 6829 28, 6829, 2023.

122. ASTM E96-80. “Test Methods for Water Vapor Transmission of Materials”. Preprint at https://doi.org/10.1520/E0096-00, 2000.

123. CAZÓN, P., MORALES-SANCHEZ, E., VELAZQUEZ, G. & VÁZQUEZ, M. “Measurement of the Water Vapor Permeability of Chitosan Films: A Laboratory Experiment on Food Packaging Materials”. J Chem Educ 99, 2403–2408, 2022.

124. TURHAN, K. N. & ŞAHBAZ, F. “Water vapor permeability, tensile properties and solubility of methylcellulose-based edible films”. J Food Eng 61, 459–466, 2004.

125. WEXLER, A. “Vapor pressure formulation for water in range 0 to 100 Degrees C. A revision”. 1971.

126. SADI, A. & FERFERA-HARRAR, H. “Cross-linked CMC/Gelatin bio-nanocomposite films with organoclay, red cabbage anthocyanins and pistacia leaves extract as active intelligent food packaging: colorimetric pH indication, antimicrobial/antioxidant properties, and shrimp spoilage tests”. Int J Biol Macromol 242, 124964, 2023.

127. BILLMEYER, F. W. & FAIRMAN, H. S. “CIE Method for Calculating Tristimulus Values”. Color Res Appl 12, 27–36, 1987.

128. EXARHOPOULOS, S., RAPHAELIDES, S. N. & KONTOMINAS, M. G. “Conformational studies and molecular characterization of the polysaccharide kefiran”. Food Hydrocoll 77, 347–356, 2018.

129. MONTOILLE, L. ET AL. “Study of the effect of the addition of plasticizers on the physical properties of biodegradable films based on kefiran for potential application as food packaging”. Food Chem 360, 2021.

130. RADHOUANI, H., GONÇALVES, C., MAIA, F. R., OLIVEIRA, J. M. & REIS, R. L. “Kefiran biopolymer: Evaluation of its physicochemical and biological properties”. https://doi.org/10.1177/0883911518793914 33, 461–478, 2018.

131. ZHANG, Y. ET AL. “Effect of carboxyl and hydroxyl groups on adsorptive polysaccharide fouling: A comparative study based on PVDF and graphene oxide (GO) modified PVDF surfaces”. J Memb Sci 595, 117514, 2020.

132. GHASEMLOU, M., KHODAIYAN, F., JAHANBIN, K., GHARIBZAHEDI, S. M. T. & TAHERI, S. “Structural investigation and response surface optimisation for improvement of kefiran production yield from a low-cost culture medium”. Food Chem 133, 383–389, 2012.

133. WANG, Y. ET AL. “Physical characterization of exopolysaccharide produced by Lactobacillus plantarum KF5 isolated from Tibet Kefir”. Carbohydr Polym 82, 895–903, 2010.

134. LIAO, B. & HUANG, H. “Structural characterization of a novel polysaccharide from Hericium erinaceus and its protective effects against H2O2-induced injury in human gastric epithelium cells”. J Funct Foods 56, 265–275, 2019.

135. DADASHI, S., BODDOHI, S. & SOLEIMANI, N. “Preparation, characterization, and antibacterial effect of doxycycline loaded kefiran nanofibers”. J Drug Deliv Sci Technol 52, 979–985 , 2019.

136. PIERMARÍA, J., BENGOECHEA, C., ABRAHAM, A. G. & GUERRERO, A. “Shear and extensional properties of kefiran”. Carbohydr Polym 152, 97–104, 2016.

137. GALDEANO, M. C. ET AL. “Effects of production process and plasticizers on stability of films and sheets of oat starch”. Materials Science and Engineering: C 29, 492–498, 2009.

138. FLEMMING, H. C. ET AL. “Biofilms: an emergent form of bacterial life”. Nature Reviews Microbiology 2016 14:9 14, 563–575, 2016.

139. HUSSAINI, I. M. ET AL. “Microbial anti-biofilms: types and mechanism of action”. Res Microbiol 175, 104111, 2024.

140. SINGH, S., DATTA, S., NARAYANAN, K. B. & RAJNISH, K. N. “Bacterial exo-polysaccharides in biofilms: role in antimicrobial resistance and treatments”. Journal of Genetic Engineering & Biotechnology 19, 140, 2021.

141. SAMBANTHAMOORTHY, K., FENG, X., PATEL, R., PATEL, S. & PARANAVITANA, C. “Antimicrobial and antibiofilm potential of biosurfactants isolated from lactobacilli against multi-drug-resistant pathogens”. BMC Microbiol 14, 1–9, 2014.

142. SENGUPTA, D., DATTA, S. & BISWAS, D. “Surfactant exopolysaccharide of Ochrobactrum pseudintermedium C1 has antibacterial potential: Its bio-medical applications in vitro”. Microbiol Res 236, 126466, 2020.

143. HAHN, M. “The rising threat of fungicide resistance in plant pathogenic fungi: Botrytis as a case study”. J Chem Biol 7, 133–141, 2014.

144. GONG, Z., ZHANG, S. & LIU, J. “Recent Advances in Chitin Biosynthesis Associated with the Morphology and Secondary Metabolite Synthesis of Filamentous Fungi in Submerged Fermentation”. Journal of Fungi 9, 205, 2023.

145. MUNRO, C. A. “Chitin and Glucan, the Yin and Yang of the Fungal Cell Wall, Implications for Antifungal Drug Discovery and Therapy”. Adv Appl Microbiol 83, 145–172, 2013.

146. CABIB, E., ROBERTS, R. & BOWERS, B. “Synthesis of the yeast cell wall and its regulation”. Annu Rev Biochem 51, 763–793, 1982.

147. KANG, X. ET AL. “Molecular architecture of fungal cell walls revealed by solid-state NMR”. Nature Communications 2018 9:1 9, 1–12,2018.

148. LI, L. ET AL. “Study on antifungal properties of modified chitosan combined with essential oil and its application in preserving fruits”. J Stored Prod Res 109, 102452, 2024.

149. ZHANG, L. ET AL. “Antifungal activity and mechanism of chitosan against Fusarium solani caused ginger soft rot during postharvest storage”. Postharvest Biol Technol 208, 112680, 2024.

150. RATNA, R., APRILIA, S., ARAHMAN, N. & MUNAWAR, A. A. “Effect of edible film gelatin nano-biocomposite packaging and storage

temperature on the store quality of strawberry (Fragaria x ananassa var.duchesne)". Future Foods 8, 100276, 2023.

151. WANG, Y. ET AL. "Silk protein: A novel antifungal and edible coating for strawberry preservation". Food Chem 463, 141179, 2025.

152. VALENZUELA, C. ET AL. "Effect of edible quinoa protein-chitosan based films on refrigerated strawberry (Fragaria × ananassa) quality". Electronic Journal of Biotechnology 18, 406–411, 2015.

153. KHODAEI, D., HAMIDI-ESFAHANI, Z. & RAHMATI, E. "Effect of edible coatings on the shelf-life of fresh strawberries: A comparative study using TOPSIS-Shannon entropy method". NFS Journal 23, 17–23, 2021.

154. DE BRUNO, A., GATTUSO, A., RITORTO, D., PISCOPO, A. & POIANA, M. "Effect of Edible Coating Enriched with Natural Antioxidant Extract and Bergamot Essential Oil on the Shelf Life of Strawberries". Foods 2023, Vol. 12, Page 488 12, 488, 2023.

155. MULEY, A. B. & SINGHAL, R. S. "Extension of postharvest shelf life of strawberries (Fragaria ananassa) using a coating of chitosan-whey protein isolate conjugate". Food Chem 329, 127213, 2020.

156. RABASCO-VÍLCHEZ, L., JIMÉNEZ-JIMÉNEZ, F., POSSAS, A., MORCILLO-MARTÍN, R. & PÉREZ-RODRÍGUEZ, F. "Evaluation of the effect of nanocellulose edible coating on strawberries inoculated with Aspergillus flavus through image analysis". LWT 191, 115697, 2024.

157. MARAEI, R. W. & ELSAWY, K. M. "Chemical quality and nutrient composition of strawberry fruits treated by γ-irradiation". J Radiat Res Appl Sci 10, 80–87, 2017.

158. JOKARI, A., MOHAMMADI JAHROMI, S. A., JOKARI, S. & JAMALI, M. "Effect of Edible Coating on Strawberry Quality Characteristics During Cold Storage". Erwerbs-Obstbau 65, 2259–2269, 2023.

159. BERTOLO, M. R. V. ET AL. "Improvement of the physical-chemical, microbiological, volatiles and sensory quality of strawberries covered with chitosan/gelatin/pomegranate peel extract-based coatings". Food Chem 471, 142755, 2025.

160. BENHABILES, M. S., DROUICHE, N., LOUNICI, H., PAUSS, A. & MAMERI, N. "Effect of shrimp chitosan coatings as affected by chitosan extraction processes on postharvest quality of strawberry". Journal of Food Measurement and Characterization 7, 215–221, 2013.

161. ALIM, K. A., FONOBEROV, V. A. & SHAMSA, M. “Micro-Raman investigation of optical phonons in ZnO nanocrystals”. J. Appl. Phys 97, 124313, 2005.

162. GATOU, M.-A., LAGOPATI, N., VAGENA, I.-A., GAZOULI, M. & PAVLATOU, E. A. “ZnO Nanoparticles from Different Precursors and Their Photocatalytic Potential for Biomedical Use”. Nanomaterials 13, 122, 2022.

163. GAUDON, M., TOULEMONDE, O. & DEMOURGUES, A. “Green Coloration of Co-Doped ZnO Explained from Structural Refinement and Bond Considerations”. Inorg Chem 46, 10996–11002, 2007.

164. ZHANG, X. ET AL. “Effect of polar/non-polar facets on the transformation of nanoscale ZnO in simulated sweat and potential impacts on the antibacterial activity”. Ecotoxicol Environ Saf 246, 114187, 2022.

165. ABDULLAH, F. H., ABU BAKAR, N. H. H. & ABU BAKAR, M. “Current advancements on the fabrication, modification, and industrial application of zinc oxide as photocatalyst in the removal of organic and inorganic contaminants in aquatic systems”. 2021. doi:10.1016/j.jhazmat.2021.127416.

166. ZHANG, X. ET AL. “Effect of aspect ratio and surface defects on the photocatalytic activity of ZnO nanorods”. Sci Rep 4, 4596, 2014.

167. GERBREDERS, V. ET AL. “Hydrothermal synthesis of ZnO nanostructures with controllable morphology change”. CrystEngComm 22, 1346–1358, 2020.

168. MURILLO, G. ET AL. “Role of aluminum and HMTA in the hydrothermal synthesis of two-dimensional n-doped ZnO nanosheets”. Nano Energy 60, 817–826, 2019.

169. LI, Y., LIAO, C. & TJONG, S. C. “Recent Advances in Zinc Oxide Nanostructures with Antimicrobial Activities”. Int J Mol Sci 21, 8836, 2020.

170. CONSONNI, V. & LORD, A. M. “Polarity in ZnO nanowires: A critical issue for piezotronic and piezoelectric devices”. Nano Energy 83, 2021.

171. LIMA, R. C. ET AL. “Toward an Understanding of Intermediate- and Short-Range Defects in ZnO Single Crystals. A Combined Experimental and Theoretical Study”. J Phys Chem A 112, 8970–8978, 2008.

172. MORA-FONZ, D. ET AL. “Why Are Polar Surfaces of ZnO Stable?”. Chemistry of Materials 29, 5306–5320, 2017.

173. Synthesis and characterization of copper zinc oxide nanoparticles obtained via metathesis process *. 2017. doi:10.1088/2043-6254/aa7223.

174. HASSANZADEH-TABRIZI, S. A. “Precise calculation of crystallite size of nanomaterials: A review”. J Alloys Compd 968, 171914, 2023.

175. QI, L. ET AL. “Facile synthesis of ZnO films with anisotropic preferred orientations: An effective strategy for controllable surface and optical property”. 2022. doi:10.1016/j.jallcom.2022.168125.

176. KHAN, M. M. ET AL. “Antibacterial Studies of ZnO and Cu-Doped ZnO Nanoparticles Synthesized Using Aqueous Leaf Extract of Stachytarpheta jamaicensis”. Bionanoscience 10, 1037–1048, 2020.

177. ASUNCION DIMAPILIS, E. S., HSU, C.-S., MARIE MENDOZA, R. O. & LU, M.-C. “Zinc oxide nanoparticles for water disinfection”. 2017. doi:10.1016/j.serj.2017.10.001.

178. PRANJALI, P. ET AL. “Physicochemical and Antibacterial Properties of PEGylated Zinc Oxide Nanoparticles Dispersed in Peritoneal Dialysis Fluid”. ACS Omega 4, 19255–19264, 2019.

179. NEL, A. E. ET AL. “Understanding biophysicochemical interactions at the nano–bio interface”. Nature Materials 2009 8:7 8, 543–557, 2009.

180. RAJAGOPAL, M. & WALKER, S. “Envelope Structures of Gram-Positive Bacteria”. Curr Top Microbiol Immunol 404, 1, 2017.

181. HUTCHINGS, C., YAIR, Z. P., REIFEN, R. & SHEMESH, M. “Antimicrobial effect of zn2+ ions governs the microbial quality of donor human milk”. Foods 10, 2021.

182. RAGHUPATHI, K. R., KOODALI, R. T. & MANNA, A. C. “Size-dependent bacterial growth inhibition and mechanism of antibacterial activity of zinc oxide nanoparticles”. Langmuir 27, 4020–4028, 2011.

183. MENDES, C. R. ET AL. “Antibacterial action and target mechanisms of zinc oxide nanoparticles against bacterial pathogens”. Scientific Reports 2022 12:1 12, 1–10, 2022.

184. HALDER, S. ET AL. “Alteration of Zeta potential and membrane permeability in bacteria: a study with cationic agents”. Springerplus 4, 1–14, 2015.

185. SINGH, A., SINGH, N. B., AFZAL, S., SINGH, T. & HUSSAIN, I. “Zinc oxide nanoparticles: a review of their biological synthesis, antimicrobial activity, uptake, translocation and biotransformation in plants. J Mater Sci 53, 185–201, 2018.

186. BROWN, S., SANTA MARIA, J. P. & WALKER, S. “Wall Teichoic Acids of Gram-Positive Bacteria”. Annu Rev Microbiol 67, 313–336, 2013.

187. BABAYEVSKA, N. ET AL. “ZnO size and shape effect on antibacterial activity and cytotoxicity profile”. Scientific Reports 2022 12:1 12, 1–13, 2022.

188. NAGARAJAN, S. & ARUMUGAM KUPPUSAMY, K. “Extracellular synthesis of zinc oxide nanoparticle using seaweeds of gulf of Mannar, India”. J Nanobiotechnology 11, 39, 2013.

189. ASHIKUZZAMAN AYON, S., JAMAL, M., MUKTADIR BILLAH, M. & NEAZ, S. “Augmentation of magnetic properties and antimicrobial activities of band gap modified Ho 3+ and Sm 3+ doped ZnO nanoparticles: A comparative experimental study”. 2021. doi:10.1016/j.jallcom.2021.163179.

190. LI, Y., ZHANG, W., NIU, J. & CHEN, Y. “Mechanism of Photogenerated Reactive Oxygen Species and Correlation with the Antibacterial Properties of Engineered Metal-Oxide Nanoparticles”. 2012. doi:10.1021/nn300934k.

191. DU, J. & GEBICKI, J. M. “Proteins are major initial cell targets of hydroxyl free radicals”. Int J Biochem Cell Biol 36, 2334–2343, 2004.

192. MAKUŁA, P., PACIA, M. & MACYK, W. “How To Correctly Determine the Band Gap Energy of Modified Semiconductor Photocatalysts Based on UV-Vis Spectra”. Journal of Physical Chemistry Letters 9, 6814–6817, 2018.

193. NAZRI, N. H. ET AL. “Physico-mechanical study of cmc/bfo/popd nanocomposite films reinforced with cellulose nanocrystals (Cncmcc) for effective photocatalytic removal of methyl orange”. Journal of Composites Science 5, 142, 2021.

194. AKHTAR, H. M. S. ET AL. “Carboxymethyl cellulose based films enriched with polysaccharides from mulberry leaves (Morus alba L.) as new biodegradable packaging material”. Int J Biol Macromol 253, 127633, 2023.

195. ANGGARINI, U. ET AL. “A highly water-selective carboxymethylated cellulose nanofiber (CNF-CMC) membrane for the separation of binary (water/N2) and ternary (water/alcohols/N2) systems in vapor-permeation”. J Memb Sci 691, 122229, 2024.

196. MICHELIN, M., MARQUES, A. M., PASTRANA, L. M., TEIXEIRA, J. A. & CERQUEIRA, M. A. “Carboxymethyl cellulose-based films: Effect of organosolv lignin incorporation on physicochemical and antioxidant properties”. J Food Eng 285, 110107, 2020.

197. EZATI, P., RIAHI, Z. & RHIM, J.-W. “CMC-based functional film incorporated with copper-doped TiO2 to prevent banana browning”. Food Hydrocoll 122, 107104, 2022.

198. SU, J.-F., HUANG, Z., YUAN, X.-Y., WANG, X.-Y. & LI, M. “Structure and properties of carboxymethyl cellulose/soy protein isolate blend edible films crosslinked by Maillard reactions”. Carbohydr Polym 79, 145–153, 2010.

199. CAPANEMA, N. S. V. ET AL. “Superabsorbent crosslinked carboxymethyl cellulose-PEG hydrogels for potential wound dressing applications”. Int J Biol Macromol 106, 1218–1234, 2018.

200. CHEN, P., XIE, F., TANG, F. & MCNALLY, T. “Glycerol plasticisation of chitosan/carboxymethyl cellulose composites: Role of interactions in determining structure and properties”. Int J Biol Macromol 163, 683–693, 2020.

201. VERMA, P. ET AL. “Transformation of banana peel into biodegradable film added with starch and carboxymethyl cellulose and its characterization”. Sustain Chem Pharm 37, 101356, 2024.

202. WANG, C. ET AL. “Preparation, characterization, and application of pH-responsive biodegradable intelligent indicator film based on rose anthocyanins”. LWT 200, 116156, 2024.

203. DAS, M. ET AL. “TiO2/graphene oxide-filled carboxymethyl cellulose/chitosan blend films”. Mater Chem Phys 332, 130233, 2025.

204. JANNATYHA, N., SHOJAEE-ALIABADI, S., MOSLEHISHAD, M. & MORADI, E. “Comparing mechanical, barrier and antimicrobial

properties of nanocellulose/CMC and nanochitosan/CMC composite films". Int J Biol Macromol 164, 2323–2328, 2020.

205. BOURBON, A. I. ET AL. "Active Carboxymethylcellulose-Based Edible Films: Influence of Free and Encapsulated Curcumin on Films' Properties". Foods 2021, Vol. 10, Page 1512 10, 1512, 2021.

206. RIAZ, A. ET AL. "Effect of Chinese chives (Allium tuberosum) addition to carboxymethyl cellulose based food packaging films". 2020. doi:10.1016/j.carbpol.2020.115944.

207. YU, K. ET AL. "The improvement of water barrier property in gelatin/carboxymethyl cellulose composite film by electrostatic interaction regulation and its application in strawberry preservation". Food Chem 450, 139352, 2024.

208. MUKHERJEE, S. ET AL. "Effects of fatty acid esters on mechanical, thermal, microbial, and moisture barrier properties of carboxymethyl cellulose-based edible films". Carbohydrate Polymer Technologies and Applications 7, 100505, 2024.

209. HIDAYATI, S., MAULIDIA, U., SATYAJAYA, W. & HADI, S. "Effect of glycerol concentration and carboxy methyl cellulose on biodegradable film characteristics of seaweed waste". 2021. doi:10.1016/j.heliyon.2021.e07799.

210. PRIYADARSHI, R., KIM, S. M. & RHIM, J. W. "Carboxymethyl cellulose-based multifunctional film combined with zinc oxide nanoparticles and grape seed extract for the preservation of high-fat meat products". Sustainable Materials and Technologies 29, e00325, 2021.

211. BASU, P., NARENDRAKUMAR, U., ARUNACHALAM, R., DEVI, S. & MANJUBALA, I. "Characterization and Evaluation of Carboxymethyl Cellulose-Based Films for Healing of Full-Thickness Wounds in Normal and Diabetic Rats". ACS Omega 3, 12622–12632, 2018.

212. VOGLER, E. A. "Structure and reactivity of water at biomaterial surfaces". Adv Colloid Interface Sci 74, 69–117, 1998.

213. PULLA-HUILLCA, P. V., GOMES, A., QUINTA BARBOSA BITTANTE, A. M., LOURENÇO, R. V. & SOBRAL, P. J. DO A. "Wettability of gelatin-based films: The effects of hydrophilic or hydrophobic plasticizers and nanoparticle loads". J Food Eng 297, 110480, 2021.

214. CHEN, P., XIE, F., TANG, F. & MCNALLY, T. “Influence of plasticiser type and nanoclay on the properties of chitosan-based materials”. Eur Polym J 144, 110225, 2021.

215. SHAHABI-GHAHFARROKHI, I., KHODAIYAN, F., MOUSAVI, M. & YOUSEFI, H. “Effect of γ-irradiation on the physical and mechanical properties of kefiran biopolymer film”. Int J Biol Macromol 74, 343–350, 2015.

216. GHASEMLOU, M., KHODAIYAN, F., OROMIEHIE, A. & YARMAND, M. S. “Characterization of edible emulsified films with low affinity to water based on kefiran and oleic acid”. Int J Biol Macromol 49, 378–384, 2011.

217. DONG, Y. ET AL. “Effect of polyol plasticizers on properties and microstructure of soluble soybean polysaccharide edible films”. Food Packag Shelf Life 35, 101023, 2023.

218. HASHEMI GAHRUIE, H. ET AL. “Development and characterization of gelatin and Persian gum composite edible films through complex coacervation”. LWT 153, 112422, 2022.

219. FAUZIAH, A. N. ET AL. “Physical performance of glycerol-plasticized cassava peel starch-carboxymethyl cellulose bioplastic”. Emergent Mater 1–19, 2025. doi:10.1007/S42247-025-01027-6/TABLES/4.

220. KHAN, A., RIAHI, Z., KIM, J. T. & RHIM, J. W. “Effect of carbon dot-doped Ti-MOF on CMC/Agar film and active packaging application on storage quality of fruits”. Food Chem 455, 139911, 2024.

221. CATEL, A. B., CAMILO, F. F. & MOLINA, C. “Enhancing luminescent and mechanical properties of carboxymethylcellulose films: The role of glycerol in lanthanide complex incorporation”. Opt Mater (Amst) 165, 117092, 2025.

222. GHASEMLOU, M., KHODAIYAN, F., OROMIEHIE, A. & YARMAND, M. S. “Development and characterisation of a new biodegradable edible film made from kefiran, an exopolysaccharide obtained from kefir grains”. Food Chem 127, 1496–1502, 2011.

223. RHIM, J. W., PARK, H. M. & HA, C. S. “Bio-nanocomposites for food packaging applications”. Prog Polym Sci 38, 1629–1652, 2013.

224. SHEN, Y. Y., ZHANG, X. D., ZHANG, D. C., ZHANG, L. H. & LIU, C. L. “(101)-oriented ZnO nanoparticles fabricated in Si (100) by Zn ion implantation and thermal oxidation”. Mater Lett 65, 3323–3326, 2011.

225. MORKOÇ, H. & ÖZGÜR, Ü. “General Properties of ZnO”. Zinc Oxide 1–76, 2009. doi:10.1002/9783527623945.CH1.

226. CUSCO, R. ET AL. “Temperature dependence of Raman scattering in ZnO”. Phys Rev B Condens Matter Mater Phys 75, 165202, 2007.

227. TANG, S. ET AL. “Ecofriendly and Biodegradable Soybean Protein Isolate Films Incorporated with ZnO Nanoparticles for Food Packaging”. ACS Appl Bio Mater 2, 2202–2207, 2019.

228. JALEH, B. ET AL. “Preparation of Polycarbonate-ZnO Nanocomposite Films: Surface Investigation after UV Irradiation”. Molecules 2022, Vol. 27, Page 4448 27, 4448, 2022.

229. GUERRERO, P., GARRIDO, T., LECETA, I. & DE LA CABA, K. “Films based on proteins and polysaccharides: Preparation and physical–chemical characterization”. Eur Polym J 49, 3713–3721, 2013.

230. PENG, Y. ET AL. “Facile synthesis of Flower-like ZnO loading Cellulose-Chitosan nanocomposite films by biomimetic approach with enhanced performance”. Appl Surf Sci 614, 156119, 2023.

231. DARBASIZADEH, B. ET AL. “Crosslinked-polyvinyl alcohol-carboxymethyl cellulose/ZnO nanocomposite fibrous mats containing erythromycin (PVA-CMC/ZnO-EM): Fabrication, characterization and in-vitro release and anti-bacterial properties”. Int J Biol Macromol 141, 1137–1146, 2019.

232. SHAHABI-GHAHFARROKHI, I. & BABAEI-GHAZVINI, A. “Using photo-modification to compatibilize nano-ZnO in development of starch-kefiran-ZnO green nanocomposite as food packaging material”. Int J Biol Macromol 124, 922–930, 2019.

233. YU, M. ET AL. “ZnO nanoparticles coated and stearic acid modified superhydrophobic chitosan film for self-cleaning and oil–water separation”. Int J Biol Macromol 231, 123293, 2023.

234. KHRANOVSKYY, V., EKBLAD, T., YAKIMOVA, R. & HULTMAN, L. “Surface morphology effects on the light-controlled wettability of ZnO nanostructures”. Appl Surf Sci 258, 8146–8152, 2012.

235. METHA, C., PAWAR, S. & SUVARNA, V. “Recent advancements in alginate-based films for active food packaging applications”. Sustainable Food Technology 2, 1246–1265, 2024.

236. TRIPATHI, S., KUMAR, L., DESHMUKH, R. K. & GAIKWAD, K. K. “Ultraviolet Blocking Films for Food Packaging Applications.” Food and Bioprocess Technology 2023 17:6 17, 1563–1582, 2023.

237. RINCÓN, E., DE HARO-NIZA, J., MORCILLO-MARTÍN, R., ESPINOSA, E. & RODRÍGUEZ, A. “Boosting functional properties of active-CMC films reinforced with agricultural residues-derived cellulose nanofibers”. RSC Adv 13, 24755–24766, 2023.

APPENDIX A

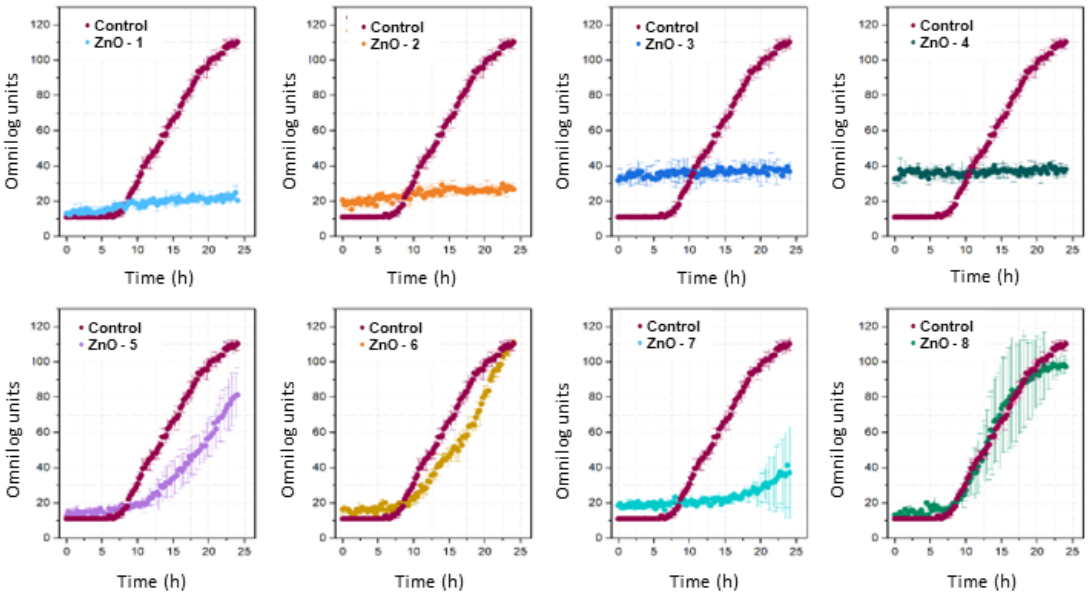

FIGURE 5.1 - Metabolism kinetics of the bacteria S. epidermidis ATCC 35984 in the presence of different samples of ZnO NPs. The purple line refers to the control without the use of ZnO NPs. Reprinted with permission from Marques et al. [80], Copyright 2024, Elsevier.

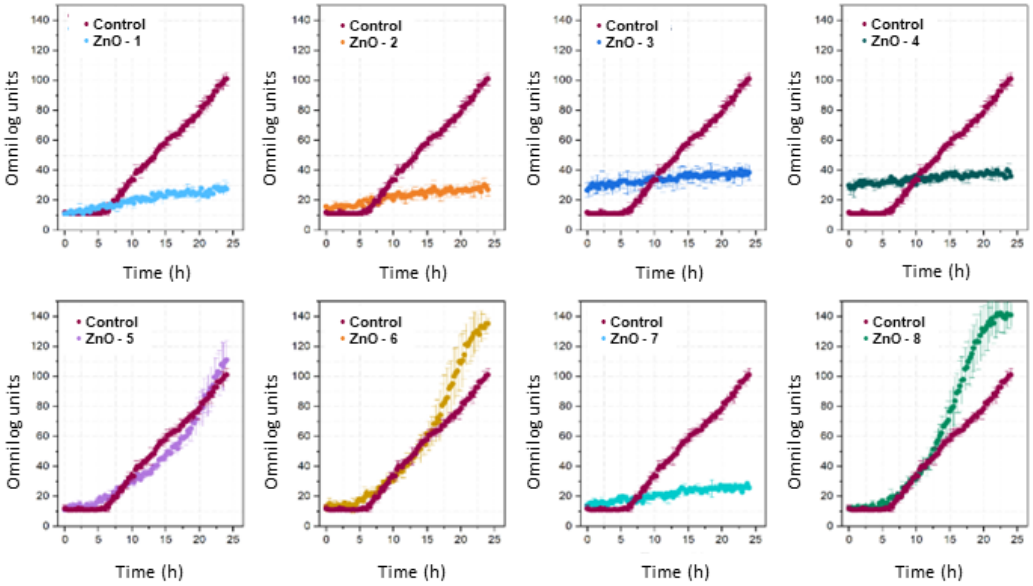

FIGURE 5.2 - Metabolism kinetics of the bacteria S. aureus ATCC 25923 in the presence of different samples of ZnO NPs. The purple line refers to the control

without the use of ZnO NPs. Reprinted with permission from Marques et al. [80], Copyright 2024, Elsevier.

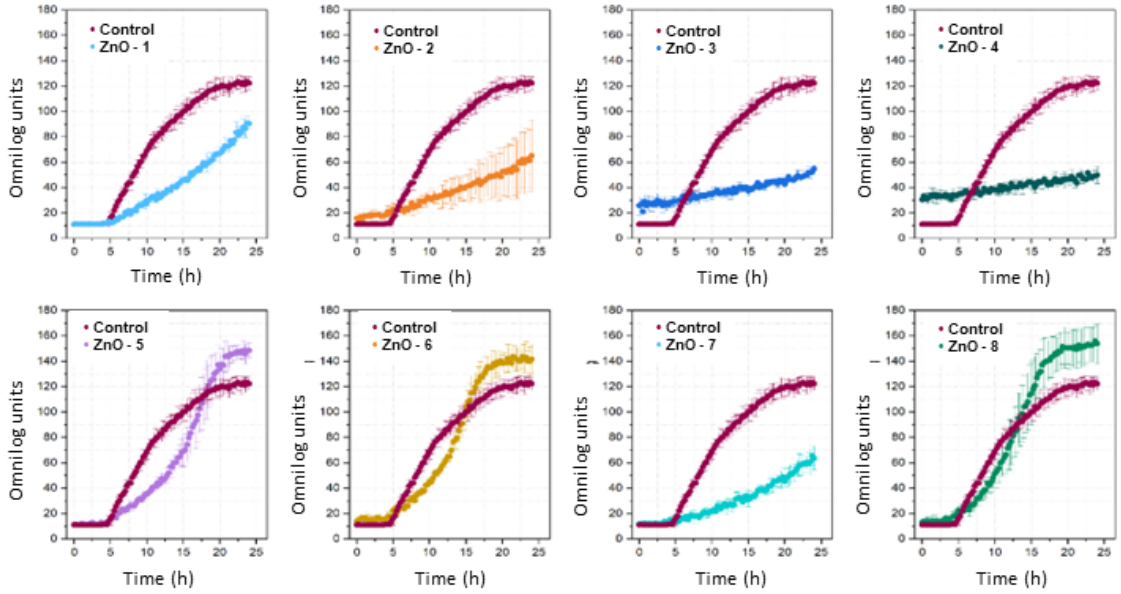

FIGURE 5.3 - Metabolism kinetics of the bacteria S. aureus ATCC 8095 in the presence of different samples of ZnO NPs. The purple line refers to the control without the use of ZnO NPs. Reprinted with permission from Marques et al. [80], Copyright 2024, Elsevier.

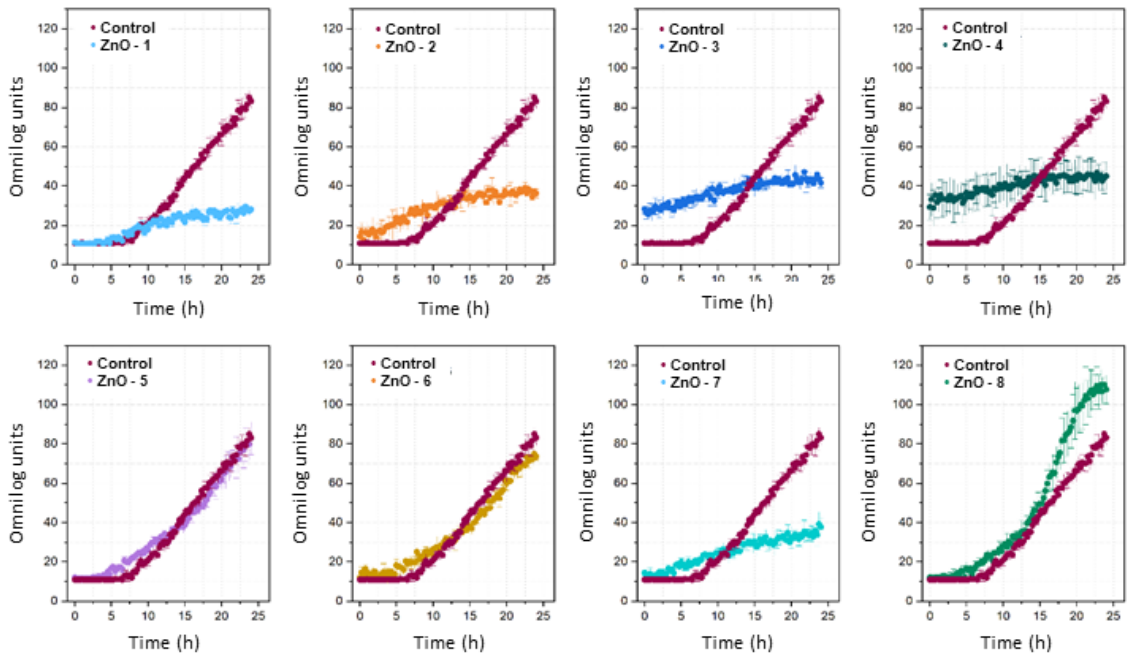

FIGURE 5.4 - Metabolism kinetics of the bacteria E. faecium ATCC 700221 in

the presence of different samples of ZnO NPs. The purple line refers to the control without the use of ZnO NPs. Reprinted with permission from Marques et al.[80], Copyright 2024, Elsevier.

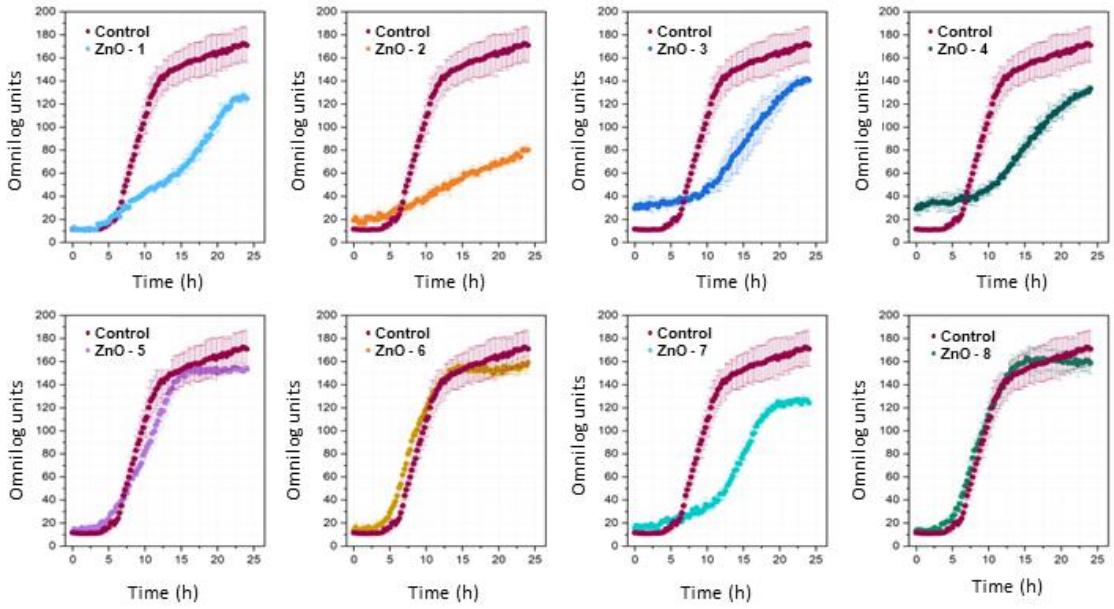

FIGURE 5.5 - Metabolism kinetics of the bacteria K. pneumoniae ATCC 700603 in the presence of different samples of ZnO NPs. The purple line refers to the control without the use of ZnO NPs. Reprinted with permission from Marques et al.[80], Copyright 2024, Elsevier.

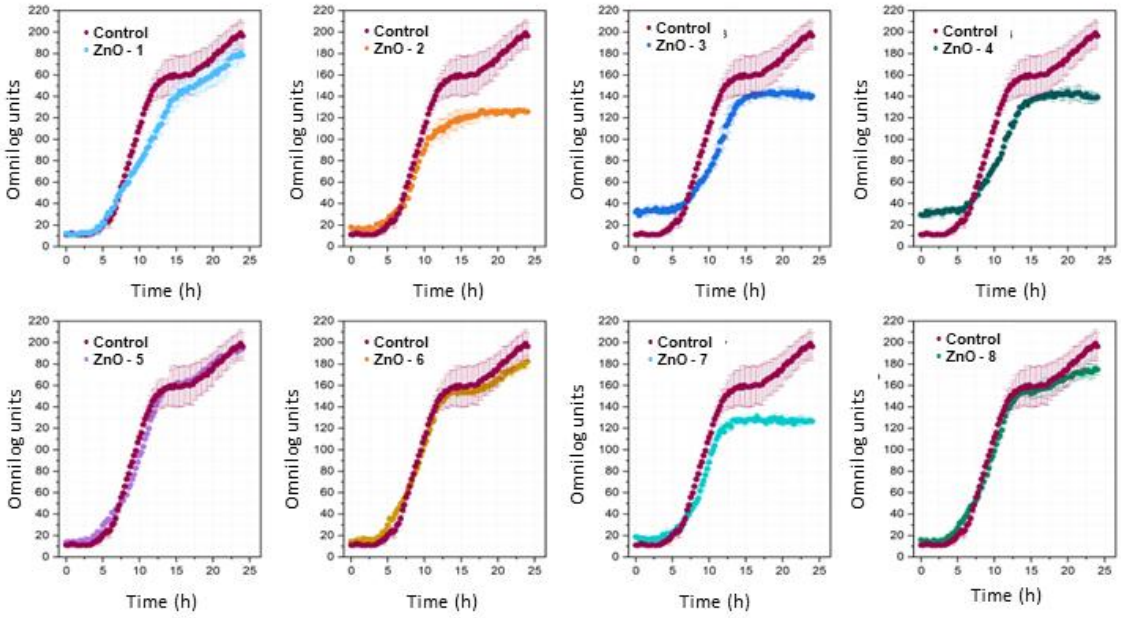

FIGURE 5.6 - Metabolism kinetics of the bacteria E. coli ATCC 25922 in the presence of different samples of ZnO NPs. The purple line refers to the control without the use of ZnO NPs. Reprinted with permission from Marques et al.[80], Copyright 2024, Elsevier.

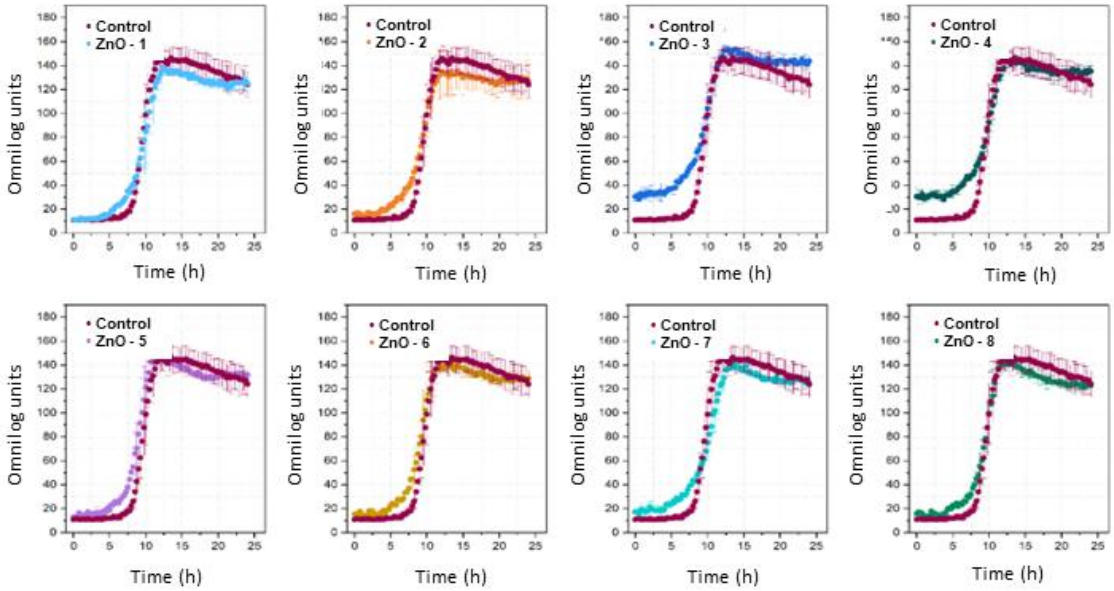

FIGURE 5.7 - Metabolism kinetics of the bacteria A. baumannii ATCC 19606 in the presence of different samples of ZnO NPs. The purple line refers to the control

without the use of ZnO NPs. Reprinted with permission from Marques et al.[80], Copyright 2024, Elsevier.

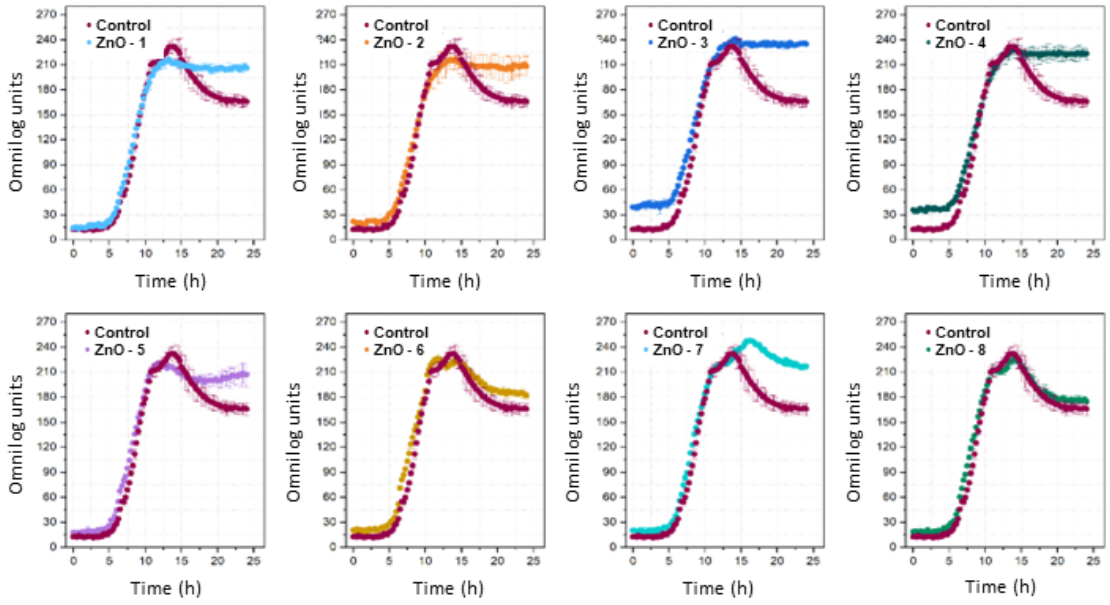

FIGURE 5.8 - Metabolism kinetics of the bacteria P. aeruginosa ATCC 27853 in the presence of different samples of ZnO NPs. The purple line refers to the control without the use of ZnO NPs. Reprinted with permission from Marques et al.[80], Copyright 2024, Elsevier.

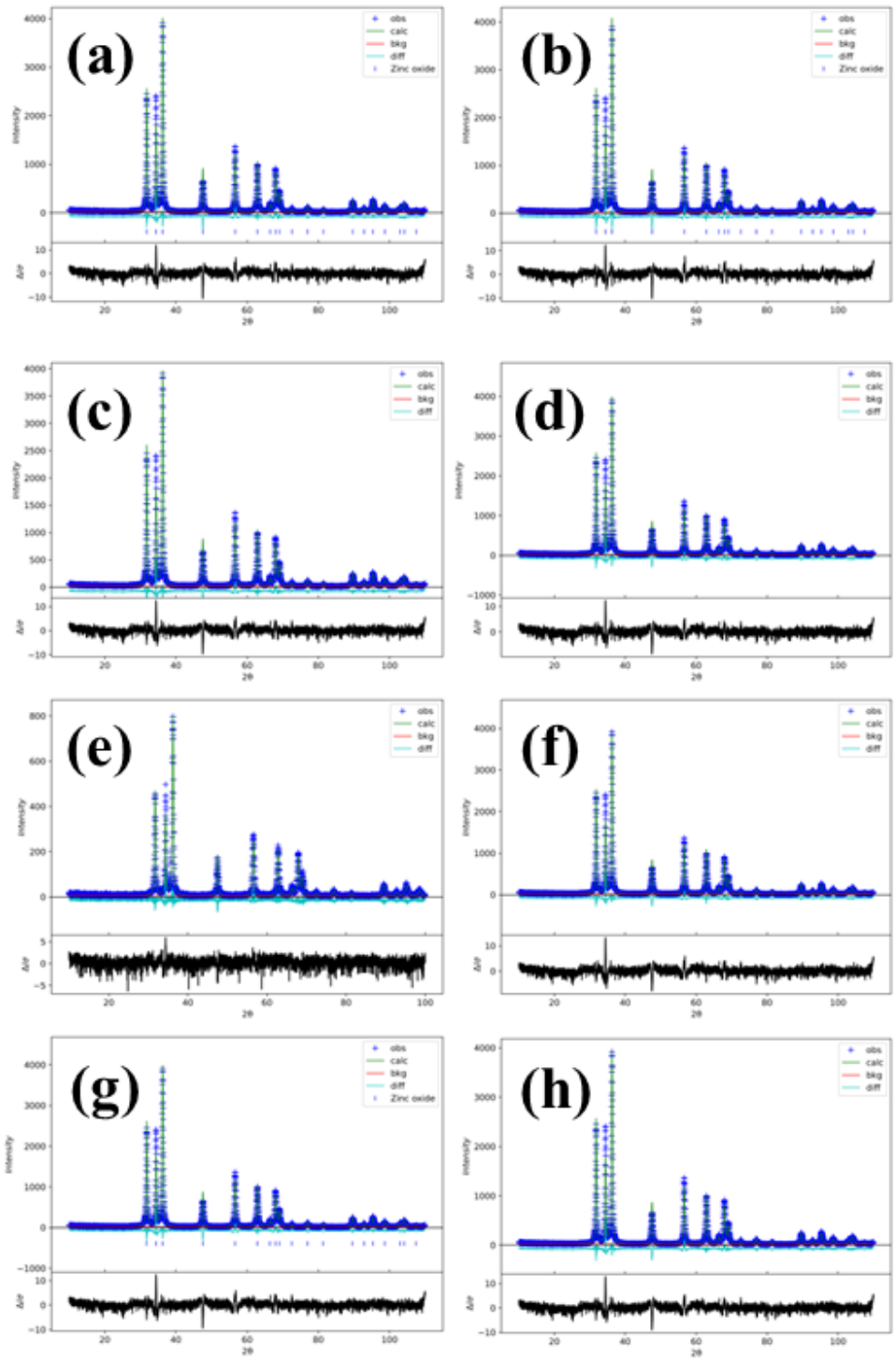

FIGURE 5.9 - Rietveld refinement XRD of ZnO NPs samples using GSAS II software. Reprinted with permission from Marques et al.[80], Copyright 2024, Elsevier.

Publication rights permission

Selective inhibitory activity of multidrug-resistant bacteria by zinc oxide nanoparticles

Author:
Gleison N. Marques,Ailton José Moreira,Eryka Thamyris D. Nóbrega,Sandalene Braga,Marcela N. Argentin,Ilana L.B. da Cunha Camargo,Emilio Azevedo,Ernesto C. Pereira,Maria Inês B. Bernardi,Lucia H. Mascaro

Publication: Journal of Environmental Chemical Engineering

Publisher: Elsevier

Date: February 2024

© 2024 Elsevier Ltd. All rights reserved.

Journal Author Rights

Please note that, as the author of this Elsevier article, you retain the right to include it in a thesis or dissertation, provided it is not published commercially. Permission is not required, but please ensure that you reference the journal as the original source. For more information on this and on your other retained rights, please visit: https://www.elsevier.com/about/our-business/policies/copyright#Author-rights

BACK CLOSE WINDOW

© 2025 Copyright - All Rights Reserved | Copyright Clearance Center, Inc. | Privacy statement | Data Security and Privacy | For California Residents | Terms and Conditions
Comments? We would like to hear from you. E-mail us at customercare@copyright.com

FIGURE 5.10 - Permission to use the article “Selective inhibitory activity of multidrug-resistant bacteria by zinc oxide nanoparticles”.

PUBLICATIONS

Articles related to the thesis

1. **Selective Inhibitory Activity of Multidrug-Resistant Bacteria by Zinc Oxide Nanoparticles**. *Journal of Environmental Chemical Engineering***.** Volume 12, Issue 1, February 2024, 111870

   Marques, Gleison N.; Moreira, Ailton José; Nóbrega, Eryka Thamyris D.; Braga, Sandalene; Argentin, Marcela N.; da Cunha Camargo, Ilana lB.; Azevedo, Emilio; Pereira, Ernesto C.; Bernardi, Maria Inês B.; Mascaro, Lucia H.

2. **Antiviral Leather: A Functional Coating Based on SiO_2-AgNPs to Eliminate Pathogens.** *Journal of Environmental Chemical Engineering*, v. 11 p. 110919, 2023.

   Marques, Gleison N.; Reis, Roberta Y.N.; Ribeiro, Lara K.; Simões, Luiz G.P.; Minozzi, Daniel T.; Andrés, Juan; Assis, Marcelo; Mascaro, Lucia H.; Longo, Elson.

3. **Density Functional Theory Calculations, Antibiofilm Properties, and Edible Coating Application of Kefiran for Strawberry Shelf-Life Extension** *International Journal of Biological Macromolecules*

   Gleison N. Marques, Alex S. Moraes, Marcela N. Argentin, Isadora C. Pedrino, Paulo T. Lacava, Daniela de A. Carrea, Isabela R. O. Pereira, Ernesto C. Pereira, Ilana L.B. da Cunha Camargo, Farayde Matta Fakhouri, Maria Inês B. Bernardi, Lucia Helena Mascaro, José Ignacio Velasco.

Articles For Submission

1. **Enhancement of Production Parameters for CMC Films via Casting to Improve the Properties of Kefiran/CMC Blends.** *International Journal of Biological Macromolecules*

   Gleison N. Marques, Fiama Martins, Maciel L. Barbosa, Maria Inês B. Bernardi, Sandra Andrea Cruz, José Ignácio Velasco, Lúcia Helena Mascaro.

2. **Boosting functional properties of active-CMC/Kefiran/ZnO NPs nanocomposite films for food packaging.** *Food Hydrocolloids*

   Gleison N. Marques, Maciel L. Barbosa, Marcelo Assis, Justin Zoppe, Farayde Matta Fakhouri, Maria Inês B. Bernardi Sandra Andrea Cruz, José Ignácio Velasco, Lúcia Helena Mascaro.

Articles produced in collaboration

1. **Degradation of emerging contaminants using Co/Nb-modified SnO_2 nanoparticles and produced with babassu mesocarp (*Orbgnya Speciosa*).** Journal of Environmental Chemical Engineering.

   Lima, Juliana B. ; **Marques, Gleison N.** ; Ferreira, Davi S. ; Moreira, Ailton. J. ; Assis, Marcelo ; Longo, Elson ; Bernardi, Maria Inês B. ; Rangel, José H.G. ; Azevedo, Emilio ; Mascaro, Lucia H. ; Oliveira, Marcelo M.

2. **Green-assisted synthesis of highly defective nanostructured Fe-doped SnO_2: magnetic and photocatalytic properties evaluation.** Acta Materialia.

   Da Silva Ribeiro, M.H. ; **Marques, G.N.** ; Moreira, A.J. ; Oliveira, M.M. ; Oliveira, R.C. ; Da Silva, R.T. ; Krohling, A.C. ; Macedo, W.A.A. ; Bernardi, M.I.B. ; Mascaro, L.H. ; Rangel, J.H.G. ; De Carvalho, H.B.

3. **Blue pigment based on Ni-doped Zn_2GeO_4: Addressing structure and electronic properties by combining experiment and theory.** Ceramics International.

   Patrocínio, Katiana L.; **Marques, Gleison N.**; Gouveia, Amanda F.; Ribeiro, Lara K.; Pinheiro, Nayara A.; Bernardi, Maria I.B.; Mascaro, Lúcia H.; Andrés, Juan; Longo, Elson; Assis, Marcelo.

4. **Anatase-rutile-brookite: Structural and photocatalytic properties of TiO_2 modified with different boron concentrations. Materials Research Bulletin.** Moreira, Ailton.J. ; De Araújo, Kelvin C. ; **Marques, Gleison N.** ; Nobrega,

Eryka T.D. ; Santos, Hugo L.S. ; Mascaro, Lucia H. ; Onofre, Yina J. ; Galeti, Helder V.A. ; Gobato, Yara Galvão ; Mastelaro, Valmor R. ; Freschi, Gian P.G. ; Godoy, Marcio P.F. ; Pereira, Ernesto C.

5. **Structural, morphological, and optical investigations of Mn-doped $LaAlO_3$ perovskite obtained by microwave-assisted combustion and rapid calcination at low temperature.** Materials Chemistry And Physics.
   Dias, Luís P.S. ; Oliveira, Jefferson S. ; **Marques, Gleison N.** ; Araújo, Tomaz R. ; Melo, Dulce M.A. ; Cabral, Aluísio A. ; Vasconcelos, Jomar S. ; Rangel, José H.G. ; Bernardi, Maria Inês B. ; Figueredo, Gilvan P.

6. **Synthesis of Hematite (α-Fe_2O_3) Nanoparticles Using Syzygium cumini Extract: Photodegradation of Norfloxacin and Enhanced Recyclability.** Materials Chemistry And Physics.
   Ferreira, Davi S. ; **Marques, Gleison N.** ; Ferreira, Adriana.Das.Mercês.P. ; Oliveira, Marcelo M. ; Da Rocha, Cláudia Q. ; Moreira, Ailton J. ; Fernandes, Carlos.H.M. ; Lanza, Marcos.R. . ; Bernardi, Maria.Inês.B. ; Mascaro, Lucia.H. ; Rangel, José.Hilton.G.

7. **Hydrolysis of cassava's (Manihot esculenta Crantz) waste polysaccharides using the natural zeolite Stilbite-Ca as catalyst.** Bioresource Technology Reports.
   Martins, Fiama ; Abreu, Milena Cristina Costa ; Diniz, Paulo Afonso Freitas; **Marques, Gleison Neres** ; Oliveira, Marcelo Moizinho ; De Jesus Silva Mendonça, Cáritas ; De Figueredo, Gilvan Pereira ; Cavalcante, Kiany Sirley Brandão.

8. **Fast and Green Hematite (α-Fe_2O_3) and Akaganeite (β-FeOOH) Synthesis Using a Microwave-Assisted Hydrothermal Process with Single Precursor and No Stabilizing Agent.** MATERIALS RESEARCH. DINIZ,

Paulo Afonso F.; Cavalcante, Kiany Sirley B.; Souza, Josiane Carneiro ; **Marques, Gleison N.** ; Santos, Fernanda Hellen De S. ; Cutrim, Fiama M. ; Henriques, Raelma B. ; Mendonça, Leonardo T. B. ; Nascimento, Ulisses M.

9. **A metal-free catalyst based on g-C_3N_4 functionalized with cyamelurate-like groups: Catalytic properties and mechanism of a new heterogeneous Fenton-like catalyst.** Carbon.
   Oliveira, Wanessa L. ; De Oliveira, Eduarda Ferreira ; Do Carmo Batista, Walker Vinícius Ferreira ; Mourão, Henrique A.J.L. ; Mendes Pires, Manoel José ; Coelho, Rafael Mendes ; Atta Diab, Gabriel Ali ; Teixeira, Ivo Freitas; **Marques, Gleison**; Mastelaro, Valmor Roberto ; Nascimento, Otaciro Rangel ; Valdés, Carlos Eduardo ; Urquieta-Gonzalez, Ernesto A. ; Ferreira, Dalva E.C. ; Pereira, Márcio C. ; De Mesquita, João Paulo.

10. **Effect of synthesis methods of Co-modified TiO2 in its photocatalytic and bactericidal activity.** Research On Chemical Intermediates. Moreira, Ailton J.; Blaskievicz, Sirlon F.; De Assis, Marcelo; **Marques, Gleison N.**; Menezes, Wallas T.; Rabello, Pietra T.; Rabahi, Cesar; Gobato, Yara G.; Freschi, Gian P. G.; Mascaro, Lucia H.; Pereira, Ernesto C.

11. **Hierarchical structure of 3D ZnO experimentally designed to achieve high performance in the sertraline photocatalysis in natural waters.** Chemical Engineering Journal.
   Silva, Thalles E.M. ; Moreira, Ailton J. ; Nobrega, Eryka T.D. ; Alencar, Ridien G. ; Rabello, Pietra T. ; Blaskievicz, Sirlon F. ; **Marques, Gleison N.**; Mascaro, Lucia H. ; Paris, Elaine C. ; Lemos, Sherlan G. ; Pereira, Ernesto C.; Freschi, Gian P.G.

12. **Nickel supported on polymeric graphitic carbon nitride for electrocatalytic in reduction of carbon dioxide.** Journal of CO_2 Utilization. Batista, Walker Vinícius Ferreira Do Carmo ; Coelho, Jessica Fernanda ; De Oliveira, Wanessa Lima ; Filho, Nivaldo Gomes Pereira ; De Oliveira, Eduarda Ferreira ; Dos Santos Da Cruz, Taís ; Da Silva, Hidila Souza Teixeira ; **Marques, Gleison Neres** ; De Mesquita, João P. ; De Souza, Rodrigo F.B. ; Neto, Almir O.

13. **Synthesis, Characterization, and Photocatalytic Investigation ofCuFe2O4for the Degradation of Dyes under Visible Light. Catalysts.** T. P. Oliveira ; S. F. Rodrigues ; **G. N. Marques** ; R. C. V. Costa ; LOPES, C. G. G. ; Aranas, C ; ROJAS, A. ; RANGE, J. G. ; OLIVEIRA, M. M.